

ISSN 0021-3438 (Print)

ISSN 2412-8783 (Online)

IZVESTIYA

**NON-FERROUS
METALLURGY**

Vol. 29, No. 1, 2023

Scientific and Technical Journal

Founded in 1958

6 Issues per year

ИЗВЕСТИЯ ВУЗОВ

**ЦВЕТНАЯ
МЕТАЛЛУРГИЯ**

Том 29, № 1, 2023

Научно-технический журнал

Основан в 1958 г.

Выходит 6 раз в год

IZVESTIYA

ISSN 0021-3438 (Print)
ISSN 2412-8783 (Online)

NON-FERROUS METALLURGY

**Vol. 29, No. 1
2023**

Scientific and Technical Journal Founded in 1958 6 Issues per year <http://cvmet.misis.ru>

Journal is included into the List of the scientific journals recommended by the Highest Attestation Commission of the Ministry of Education and Science of the Russian Federation for publishing the results of doctoral and candidate dissertations
Abstracting/Indexing: Russian Science Citation Index (RSCI), Chemical Abstracts (Online), INIS, OCLC ArticleFirst, Ulrich's Periodicals Directory, VINITI Database (Abstract Journal)

Founder



National University of Science and Technology "MISIS"
Address: 4 Leninskiy Prosp., Moscow 119049, Russia
<http://www.misis.ru>

Editor-in-Chief

Evgeny A. Levashov

Prof., Dr. Sci. (Eng.), Acad. of the RANS, NUST MISIS, Moscow, Russia

Deputy Editor

Vladislava A. Ignatkina

Prof., Dr. Sci., NUST MISIS, Moscow, Russia

Editorial Board

Abhilash – Dr., Ph.D., CSIR – National Metallurgical Laboratory, Jamshedpur, India
E.V. Ageev – Prof., Dr. Sci. (Eng.), SouthWest State University, Kursk, Russia
M.V. Ananyev – Prof., Dr. Sci. (Chem.), Federal State Research and Development Institute of Rare Metal Industry (JSC "Giredmet"), Moscow, Russia
N.A. Belov – Prof., Dr. Sci. (Eng.), NUST MISIS, Moscow, Russia
E.V. Bogatyreva – Prof., Dr. Sci. (Eng.), NUST MISIS, Moscow, Russia
V.B. Deev – Prof., Dr. Sci. (Eng.), NUST MISIS, Moscow, Russia
V.M. Denisov – Prof., Dr. Sci. (Chem.), Siberian Federal University, Krasnoyarsk, Russia
D.V. Drobot – Prof., Dr. Sci. (Chem.), Russian Technological University (MITHT), Moscow, Russia
F.V. Grechnikov – Prof., Dr. Sci. (Eng.), Acad. of RAS, Samara National Research University n.a. S.P. Korolev (Samara University), Samara, Russia
D.V. Gunderov – Dr. Sci. (Phys.-Math.), Institute of Molecule and Crystal Physics Ufa Research Center of the RAS, Ufa, Russia
B. B. Khina – Dr. Sci. (Phys.-Math.), The Physical-Technical Institute of NAS of Belarus, Minsk, Belarus
D.V. Louzguine – Prof., Dr. Sci., Tohoku University, Japan
S.V. Mamyachenkov – Prof., Dr. Sci. (Eng.), Ural Federal University, Ekaterinburg, Russia
Z.A. Mansurov – Dr. Sci. (Chem.), Prof., Institute of Combustion Problems, Almaty, Kazakhstan
N.V. Nemchinova – Prof., Dr. Sci. (Eng.), Irkutsk National Research Technical University, Irkutsk, Russia
K.V. Nikitin – Prof., Dr. Sci. (Eng.), Samara State Technical University, Samara, Russia
H.A. Oye – Prof., Dr., Norwegian University of Science and Technology, Trondheim, Norway
P.V. Polyakov – Prof., Dr. Sci. (Chem.), Siberian Federal University, Krasnoyarsk, Russia

E.S. Prusov – Cand. Sci. (Eng.), Vladimir State University, Vladimir, Russia
V.N. Richkov – Prof., Dr. Sci. (Chem.), Ural Federal University, Ekaterinburg, Russia
D. Sadovay – Prof., Dr., Massachusetts Institute of Technology, Boston, USA
G.A. Salishchev – Prof., Dr. Sci. (Eng.), Belgorod National Research University, Belgorod, Russia
D.V. Shtansky – Prof., Dr. Sci. (Phys.-Math.), NUST MISIS, Moscow, Russia
V.M. Sizyakov – Prof., Dr. Sci. (Eng.), Saint-Petersburg Mining University, St. Petersburg, Russia
Stopic Srecko – Dr.-Ing. habil., RWTH Aachen University, Aachen, Germany
B.B. Straumal – Prof., Dr. Sci. (Phys.-Math.), Institute of Solid State Physics of the RAS, Chernogolovka, Moscow region
O.Yu. Tkacheva – Dr. Sci. (Chem.), Institute of High Temperature Electrochemistry of the Ural Branch of the RAS, Ekaterinburg, Russia
M. Verhaege – Prof., Dr., University of Gent, Belgium
G.M. Vol'dman – Prof., Dr. Sci. (Chem.), Russian Technological University (MITHT), Moscow, Russia
G. Xanthopoulou – Dr., National Center for Scientific Research "Demokritos", Agia Paraskevi, Attica, Greece
A.L. Yerokhin – Prof., Dr., University of Manchester, United Kingdom
Onuralp Yücel – Prof., Dr., Istanbul Technical University, Maslak, Istanbul, Turkey
Yu.P. Zaikov – Prof., Dr. Sci. (Chem.), Institute of High Temperature Electrochemistry of the Ural Branch of the RAS, Ekaterinburg, Russia
R.Kh. Zalavutdinov – Cand. Sci. (Phys.-Math.), A.N. Frumkin Institute of Physical Chemistry and Electrochemistry of the RAS, Moscow, Russia
M. Zinigrad – Prof., Dr., Ariel University, Ariel, Israel
A.I. Zouboulis – Prof., Dr., Aristotle University of Thessaloniki, Greece

Editorial Staff

Address: NUST MISIS, build 1, 4 Leninskiy Prosp., Moscow 119049, Russia

Phone: +7 (495) 638-45-35

E-mail: izv.vuz@misis.ru

Certificate of registration No. 015842 (13.03.1997)

Re-registration PI No. ФС77-79229 (25.09.2020)

Subscription: Ural-Press Agency

Leading Editor – A.A. Kudinova

Executive Editor – O.V. Sosnina

Layout Designer – E.A. Legkaya

Signed print 13.02.2023. Format 60×90 1/8.

Offset paper No. 1. Digital printing. Quires 10.5

Order 16756. Free price

Printed in the printing house of the MISIS Publish House

4 Leninskiy Prosp., Moscow, 119049 Russia. Phone/fax: +7 (499) 236-76-17



© NUST MISIS, Moscow, 2023

© Izvestiya. Non-Ferrous Metallurgy, 2023



Articles are available under Creative Commons Attribution Non-Commercial No Derivatives

ИЗВЕСТИЯ ВУЗОВ ЦВЕТНАЯ МЕТАЛЛУРГИЯ

ISSN 0021-3438 (Print)

ISSN 2412-8783 (Online)

Том 29, № 1 2023

Научно-технический журнал Основан в 1958 г. Выходит 6 раз в год <http://cvmet.misis.ru>

Журнал включен в Перечень рецензируемых научных изданий, рекомендованных ВАК Минобрнауки РФ для публикации результатов диссертаций на соискание ученых степеней

Журнал включен в базы данных: Russian Science Citation Index (RSCI), Chemical Abstracts (Online), INIS, OCLC ArticleFirst, Ulrich's Periodicals Directory, РИНЦ, БД/РЖ ВИНТИ

Учредитель



ФГАОУ ВО Национальный исследовательский технологический университет «МИСИС»
Адрес: 119049, г. Москва, Ленинский пр-т, 4
<http://www.misis.ru>

Главный редактор

Евгений Александрович Левашов

д.т.н., академик РАЕН, профессор, НИТУ МИСИС, г. Москва

Заместитель главного редактора

Владислава Анатольевна Игнаткина

д.т.н., профессор, НИТУ МИСИС, г. Москва

Редакционная коллегия

- Е.В. Агеев** – д.т.н., ЮЗГУ, г. Курск
М.В. Апаньев – д.х.н., АО «Гиредмет», г. Москва
Н.А. Белов – д.т.н., проф., НИТУ МИСИС, г. Москва
Е.В. Богатырева – д.т.н., НИТУ МИСИС, г. Москва
Г.М. Вольдман – д.х.н., проф., РТУ (МИТХТ), г. Москва
Ф.В. Гречников – д.х.н., акад. РАН, проф., СНИУ, г. Самара
Д.В. Гундеров – д.ф.-м.н., ИФМК УНЦ РАН, г. Уфа
В.Б. Деев – д.т.н., проф., НИТУ МИСИС, г. Москва
В.М. Денисов – д.х.н., проф., СФУ, г. Красноярск
Д.В. Дробот – д.х.н., проф., РТУ (МИТХТ), г. Москва
Ю.П. Зайков – д.х.н., проф., ИВТЭ УрО РАН, г. Екатеринбург
Р.Х. Залавутдинов – к.ф.-м.н., ИФХЭ РАН, г. Москва
С.В. Мамяченков – д.т.н., проф., УрФУ, г. Екатеринбург
З.А. Мансуров – д.х.н., проф., Институт проблем горения, г. Алматы, Казахстан
Н.В. Немчинова – д.т.н., проф., ИРНИТУ, г. Иркутск
К.В. Никитин – д.т.н., проф., СамГТУ, г. Самара
П.В. Поляков – д.х.н., проф., СФУ, г. Красноярск
Е.С. Прусов – к.т.н., доцент, ВлГУ, г. Владимир
В.Н. Рычков – д.х.н., проф., УрФУ, г. Екатеринбург
Г.А. Салищев – д.т.н., проф., НИУ «БелГУ», г. Белгород
В.М. Сизяков – д.т.н., проф., СПГУ, г. Санкт-Петербург
Б.Б. Страумал – д.ф.-м.н., проф., ИФТТ РАН, г. Черноголовка
О.Ю. Ткачева – д.х.н., ИВТЭ УрО РАН, г. Екатеринбург
Б.Б. Хина – д.ф.-м.н., доц., ФТИ НАН Беларуси, г. Минск, Беларусь
Д.В. Штанский – д.ф.-м.н., проф., НИТУ МИСИС, г. Москва
Abhilash – Dr., Ph.D., CSIR – National Metallurgical Laboratory, Jamshedpur, India
D.V. Louzguine – Prof., Dr., Tohoku University, Japan
H.A. Oye – Prof., Dr., Norwegian University of Science and Technology, Trondheim, Norway
D. Sadoway – Prof., Dr., Massachusetts Institute of Technology, Boston, USA
Stopic Srecko – Dr.-Ing. habil., RWTH Aachen University, Aachen, Germany
M. Verhaege – Prof., Dr., University of Gent, Belgium
G. Xanthopoulou – Dr., National Center for Scientific Research «Demokritos», Agia Paraskevi, Attica, Greece
A.L. Yerokhin – Prof., Dr., University of Manchester, United Kingdom
Yücel Onuralp – Prof., Dr., Istanbul Technical University, Maslak, Istanbul, Turkey
M. Zinigrad – Prof., Dr., Ariel University, Ariel, Israel
A.I. Zouboulis – Prof., Dr., Aristotle University of Thessaloniki, Greece

Редакция журнала

Адрес: 119049, г. Москва, Ленинский пр-т, 4, стр. 1.
НИТУ МИСИС

Тел.: +7 (495) 638-45-35

E-mail: izv.vuz@misis.ru

Свидетельство о регистрации № 015842 от 13.03.1997 г.
Перерегистрация ПИ № ФС77-79229 от 25.09.2020 г.

Подписка: Агентство «Урал-пресс»

Ведущий редактор – А.А. Кудинова

Выпускающий редактор – О.В. Соснина

Дизайн и верстка – Е.А. Легкая

Подписано в печать 13.02.2023. Формат 60×90 1/8.
Бум. офсетная № 1. Печать цифровая. Усл. печ. л. 10,5
Заказ 16756. Цена свободная

Отпечатано в типографии Издательского Дома МИСИС
119049, г. Москва, Ленинский пр-т, 4. Тел./факс: +7 (499) 236-76-17



© НИТУ МИСИС, Москва, 2023

© «Известия вузов. Цветная металлургия», 2023



Статьи доступны под лицензией Creative Commons Attribution Non-Commercial No Derivatives

Mineral Processing of Nonferrous Metals

- 5 Lavrinenko A.A., Lucinian O.G., Kuznetsova I.N., Olennikov V.G.
Obtaining copper concentrate during iron ore processing

Metallurgy of Nonferrous Metals

- 16 Novikov D.O., Galkova L.I., Maltsev G.I.
The disposal of sulfide-arsenic cake
- 26 Bulatov K.V., Zhukov V.P., Bratygin E.V., Tomilov N.A., Menshchikov V.A.
Investigation of Pobeda furnace bubbling zone physics using cold modeling method
Part 3. The hydro-gas dynamics of combined blowing of liquid by gas using bottom and lateral lances

Foundry

- 39 Bazhenov V.E., Baranov I.I., Lyskovich A.A., Koltugin A.V., Sannikov A.V., Kyaramyan K.A., Belov V.D., Pavlinich S.P.
Investigation of castability, mechanical, corrosion properties and flammability of the ML-OPB and EWZ43 magnesium alloys

Physical Metallurgy and Heat Treatment

- 56 Zorin I.A., Aryshensky E.V., Drits A.M., Kononov S.V., Komarov V.S.
Effect of hafnium on cast microstructure in alloy 1570
- 66 Volodin V.N., Tuleushev Yu.Zh., Kaliyeva A.K., Zhakanbayev E.A., Mamyrbayev A.K.
V–Cd nanoparticle-formed alloys: fabrication, phase composition and structure
- 75 Razumovsky M.I., Rodin A.O., Bokstein B.S.
Interdiffusion in refractory metal systems with a BCC lattice: titanium–tantalum and titanium–multicomponent (high-entropy) alloy

Chronicle

- 84 In memory of Vladimir Alexandrovich Lebedev

Обогащение руд цветных металлов

- 5 Лавриненко А.А., Лусинян О.Г., Кузнецова И.Н., Оленников В.Г.
Получение медного концентрата при обогащении железных руд

Металлургия цветных металлов

- 16 Новиков Д.О., Галкова Л.И., Мальцев Г.И.
Утилизация сульфидно-мышьяковистого кека
- 26 Булатов К.В., Жуков В.П., Братыгин Е.В., Томилов Н.А., Меньшиков В.А.
Исследование физических явлений в барботажной зоне плавильного агрегата «Победа» методом холодного моделирования.
Сообщение 3. Гидрогазодинамика комбинированной продувки жидкости газом с помощью донной и боковой фурм

Литейное производство

- 39 Баженов В.Е., Баранов И.И., Лыскович А.А., Колтыгин А.В., Санников А.В., Кярамян К.А., Белов В.Д., Павлинич С.П.
Исследование литейных, механических, коррозионных свойств и пожароопасности магниевых сплавов МЛ-ОПБ и EWZ43

Металловедение и термическая обработка

- 56 Зорин И.А., Арышенский Е.В., Дриц А.М., Коновалов С.В., Комаров В.С.
Влияние гафния на литую микроструктуру в сплаве 1570
- 66 Володин В.Н., Тулеушев Ю.Ж., Калиева А.К., Жаканбаев Е.А., Мамырбаев А.К.
Сформированные наночастицами сплавы V–Cd: получение, фазовый состав и структура
- 75 Разумовский М.И., Родин А.О., Бокштейн Б.С.
Взаимная диффузия в системах на основе тугоплавких металлов с ОЦК-решеткой: титан–тантал и титан – многокомпонентный (высокоэнтропийный) сплав

Хроника

- 84 Памяти Владимира Александровича Лебедева

UDC 622.765

<https://doi.org/10.17073/0021-3438-2023-1-5-15>

Research article

Научная статья



Obtaining copper concentrate during iron ore processing

A.A. Lavrinenko¹, O.G. Lucinian¹, I.N. Kuznetsova¹, V.G. Olennikov²

¹ Institute of Complex Development of Mineral Resources n.a. Acad. N.V. Melnikov of the Russian Academy of Sciences

4 Kryukovsky impasse, Moscow, 111020, Russia

² LLC NPF “Mashgeo”

105 Skuratov str., Tula, 300026, Russia

✉ Anatolii A. Lavrinenko (lavrin_a@mail.ru)

Abstract: The data on the complex processing of iron ore from one of the deposits of the Republic of Kazakhstan, which involves several operations of wet magnetic separation with re-grinding of raw products and their subsequent refining to produce a conditioned iron concentrate with 65–66 % iron containing 79–80 % Fe and 2.2–2.5 % Si, are presented. It was found that during the magnetic enrichment of the ore under study, the copper minerals concentrate in the magnetic separation tailings and the copper content in them increases from 0.093 to 0.2 %. A scheme and reagent system have been developed for the recovery of conditioned copper concentrate from magnetically enriched tailings. To obtain copper concentrate, magnetic separation tailings are subjected to regrinding in a lime medium to a fineness of 75 % of the –0.071 mm grade. After two operations of the main copper flotation with the use of water glass, butyl xanthate and frother MIBK, waste tailings are obtained. The froth product of the first basal flotation is cleaned twice. The result is a copper concentrate containing 15.2 % copper, 26.5 % iron, 17.5 % sulfur, 3.47 % silicon, 1.4 % aluminum and 8.5 % zinc, which corresponds to the KM-7 grade according to GOST R 52998-2008. Waste tailings contain: copper 0.08 %, iron 20.1 %, sulfur 0.25 %, silicon 16.2 %, aluminum 6.4 % and zinc 0.045 %. The influence of xanthates with different length and structure of hydrocarbon radical as well as hostaflots and amyl aeroflots on the process of copper flotation is studied. The high efficiency of butyl xanthate in the flotation of copper minerals has been confirmed.

Keywords: wet magnetic separation, iron ore, butyl xanthate, aeroflot, Hostaflots, copper concentrate

For citation: Lavrinenko A.A., Lucinian O.G., Kuznetsova I.N., Olennikov V.G. Obtaining copper concentrate during iron ore processing. *Izvestiya. Non-Ferrous Metallurgy*. 2023; 29 (1): 5–15. (In Russ.). <https://doi.org/10.17073/0021-3438-2023-1-5-15>

Получение медного концентрата при обогащении железных руд

А.А. Лавриненко¹, О.Г. Лусинян¹, И.Н. Кузнецова¹, В.Г. Оленников²

¹ Институт проблем комплексного освоения недр им. акад. Н.В. Мельникова РАН

111020, Россия, г. Москва, Крюковский тупик, 4

² ООО НПФ «Машгео»

300026, Россия, г. Тула, ул. Скуратовская, 105

✉ Анатолий Афанасьевич Лавриненко (lavrin_a@mail.ru)

Аннотация: Приведены данные по комплексной переработке железной руды одного из месторождений Республики Казахстан, которая предусматривает несколько операций мокрой магнитной сепарации с доизмельчением полученных черновых

продуктов и последующую их перемычку с получением кондиционного железного концентрата, содержащего 65–66 % железа при извлечении 79–80 % Fe и 2,2–2,5 % Si. Установлено, что при магнитном обогащении исследуемой руды медные минералы концентрируются в хвостах магнитной сепарации и содержание меди в них повышается с 0,093 до 0,2 %. Разработана схема и реагентный режим получения кондиционного медного концентрата из хвостов магнитного обогащения. Для получения медного концентрата хвосты магнитной сепарации подвергаются доизмельчению в известковой среде до крупности 75 % класса –0,071 мм. После двух операций основной медной флотации с применением жидкого стекла, бутилового ксантогената и вспенивателя МИБК получают отвальные хвосты. Пенный продукт первой основной флотации дважды перечищается. В результате получается медный концентрат с содержанием, %: 15,2 Cu, 26,5 Fe, 17,5 S, 3,47 Si, 1,4 Al и 8,5 Zn, который соответствует марке КМ-7 (ГОСТ Р 52998–2008). Отвальные хвосты содержат, %: 0,08 Cu, 20,1 Fe, 0,25 S, 16,2 Si, 6,4 Al и 0,045 Zn. Рассмотрено влияние на процесс медной флотации ксантогенатов с различной длиной и строением углеводородного радикала, а также Хостафлотов и амилового аэрофлота. Подтверждена высокая эффективность бутилового ксантогената при флотации медных минералов.

Ключевые слова: мокрая магнитная сепарация, железная руда, бутиловый ксантогенат, аэрофлот, Хостафлоты, медный концентрат

Для цитирования: Лавриненко А.А., Лусинян О.Г., Кузнецова И.Н., Оленников В.Г. Получение медного концентрата при обогащении железных руд. *Известия вузов. Цветная металлургия*. 2023; 29 (1): 5–15. <https://doi.org/10.17073/0021-3438-2023-1-5-15>

Introduction

The industry's increasing demand for nonferrous metals has made it increasingly important to involve poor ores and enrichment tailings in comprehensive processing of minerals. The practice of iron ore enrichment shows that the tailings of iron ore enrichment plants often contain significant amounts of nonferrous metal minerals. The content of these constituents is usually less than in the ores of the same name, and the usefulness of their extraction is not always apparent.

The processing of raw materials with an unbalanced content of valuable components is usually carried out according to combined schemes involving enrichment and metallurgical methods [1–3]. The preparation of mineral raw materials for enrichment plays an important role [4–6], and often requires finer grinding in comparison with the initial ore raw materials for breaking down the aggregates [7].

Development of rational enrichment schemes and effective choice of reagent regime in flotation of prepared (previously grinded) raw materials (enrichment tailings) makes it possible to include products with unbalanced content of valuable components in processing [8–12].

The objective of this work was to develop a technology to recover not only iron ore concentrate but also copper concentrate from current magnetic enrichment tailings.

Objects and research methods

Studies were conducted on an ore sample with a content of 44.6 % iron and 0.093 % copper. The composition of the main elements of the ore is given below, %:

Ag	1.36 g/t	K	0.25
Al	1.96	Na	0.31
Ca	1.51	Zn	0.087
Cu	0.093	S	3.46
Fe	44.60	Si	7.2

It can be seen that of the precious metals silver is present in the sample — about 1.4 g/t.

Using X-ray phase analysis on X-ray diffractometer X'Pert PRO MPD (PANalytical, Netherlands) the following mineral composition of the ore sample, wt.% was established:

Magnetite	56.19
Hematite.....	3.3
Chalcopyrite.....	0.62
Pyrite	6.19
Chlorite	0.95
Mica	0.14
Feldspar.....	4.9
Asbestos	0.71
Sphalerite	1.9
Amphibole.....	8.06
Pyroxene	4.74
Quartz	6.42
Carbonate.....	1.1
Epidote	2.77
Others: gypsum, talc, apatite, polymineral aggregates	2.01
Total	100

Optical and mineralogical analysis showed that the main ore mineral is magnetite, which is noted both in the form of grains and aggregates with rock-forming

minerals (Fig. 1). Secondary minerals are hematite, pyrite, feldspar, quartz, pyroxene, amphibole, and epidote. The ore also contains sphalerite, carbonate, chlorite,

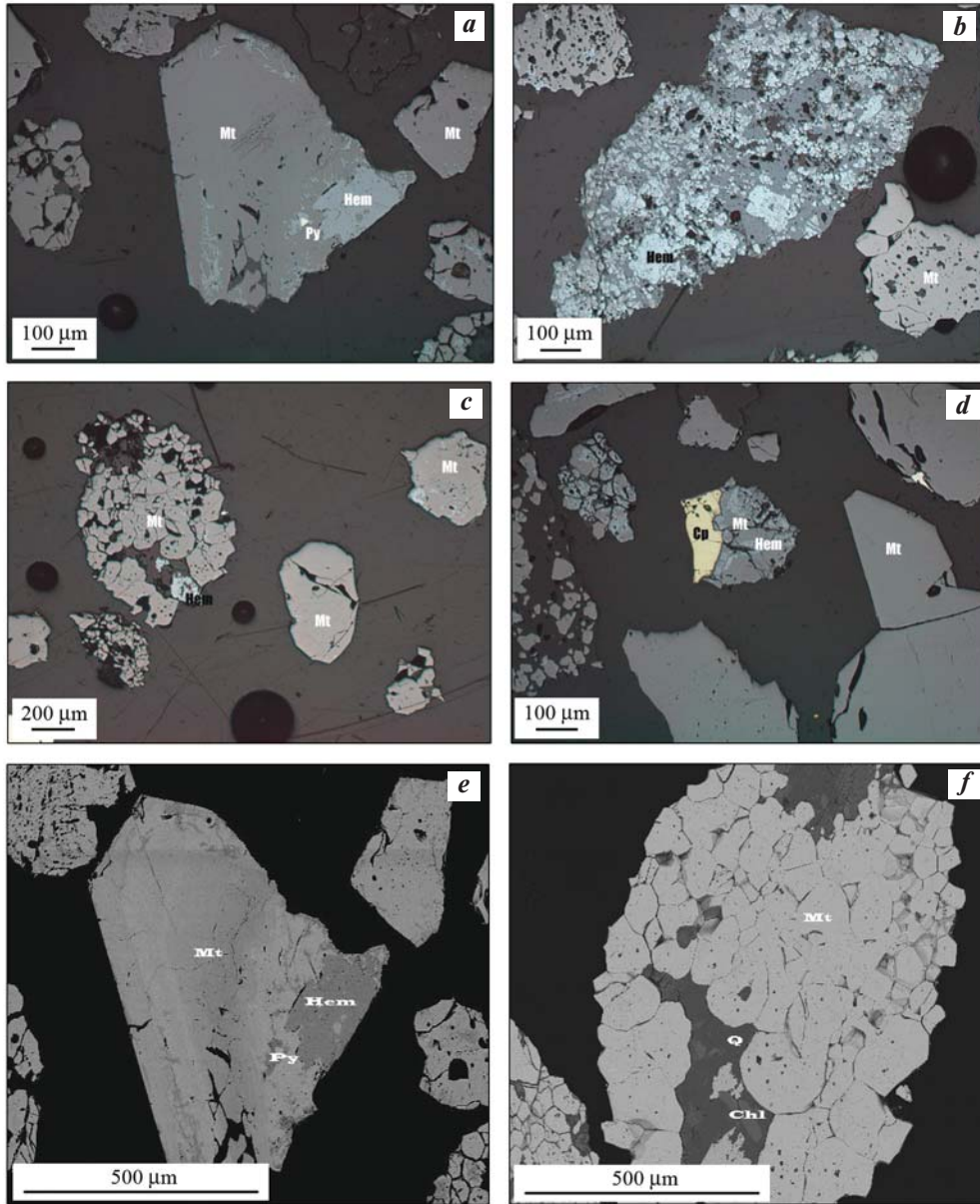


Fig. 1. Optical and mineralogical analysis results.

a – magnetite grains fragments, some grains are subject to hematization, reflected light, nicoli are parallel; *b* – magnetite, hematized to various degrees, and hematite grains fragments, reflected light, nicoli are parallel; *c* – magnetite and hematite grains fragments, reflected light, nicoli are parallel; *d* – magnetite and chalcopyrite aggregation, reflected light, nicoli are parallel; *e* – magnetite with hematite and pyrite aggregation, back-scattered electrons image; *f* – magnetite with quartz and clinochlorite aggregation, back-scattered electrons image

Рис. 1. Результаты оптико-минералогического анализа

a – фрагменты зерен магнетита, некоторые зерна подвержены гематитизации, отраженный свет, николи параллельны; *b* – фрагменты зерен магнетита, в различной степени подверженные гематитизации, и гематита, отраженный свет, николи параллельны; *c* – фрагменты зерен магнетита и гематита, отраженный свет, николи параллельны; *d* – сросток магнетита и халькопирита, отраженный свет, николи параллельны; *e* – сросток магнетита с гематитом и пиритом, изображение в обратно-рассеянных электронах; *f* – сросток магнетита с кварцем и клинохлором, изображение в обратно-рассеянных электронах

and asbestos. The rest of the minerals are represented in a landmark quantity.

The study of the composition of the sample material has shown that the basic processing of the ore is associated with the technology of extraction of ferrous minerals. Further it is useful to extract copper from the magnetically enriched tailings, which requires solving some schematic problems.

In the laboratory technological study, the ore was grinded in a jaw grinder SChKD 150×200, then the grinder KID-100 was used. Ore grinding was carried out in a roller ball mill with a volume of 1 L. The PBSZ-22 magnetic separator with two drums with variable rotational speed and constant magnetic induction of 0.15 and 0.25 T was used for dry magnetic separation at different magnetic field strengths.

To simulate a continuous process of wet magnetic separation, we used a system consisting of a wet magnetic separator MMS-0.1 PM and a pump. The magnetic induction of the drum separator is 0.15 T. The rotation speed of the magnetic system and the pump power are regulated. The flotation tests were performed in the FM2M laboratory flotation machine with a chamber volume of 150–500 cm³. Various xanthates (butyl, isobutyl, amyl, isoamyl), Hostaflots, amyl aeroflot, lime, liquid glass, MIBK were used. Hostaflots contained major components such as LIB E, sodium salt of Dithiophosphoric acid O,O-diisobutyl; Hostafлот 3403, Sodium O,O-diisobutyl dithiophosphate; Hostafлот X-23, O-ethyl-N-isopropyl thionocarbamate; Hostafлот X 231, O-N-isopropyl thiocarbamate.

Operational determination of useful constituent content was performed using Olympus X-5000 X-ray fluorescence analyzer (USA) and balance determination was performed using ARL Advantx X-ray fluorescence spectrometer (ThermoFisher Scientific, Switzerland).

Technological study

The main technological studies on the ore with the aim of developing an optimal scheme and technology of its enrichment were carried out in two directions: dry and wet magnetic separation and copper flotation from magnetically enriched tailings.

The scheme of laboratory tests for obtaining iron concentrate included: grinding of the initial ore to a size of –2+0 mm, two operations (base and control) of dry magnetic separation, the concentrates of which were combined. The coarseness of the combined concentrate was 8 % of the –0.071 mm grade. The grinding of the

concentrate to a content of 63 % of the –0.071 mm grade and its dry magnetic separation make it possible to increase the quality of the iron concentrate from 52.8 % to 57.3 %, while the iron yield in the concentrate remains constantly high at 82–83 %.

Further investigations to improve the quality of the concentrate were carried out involving the wet magnetic enrichment process. As a result, an optimal technological scheme for the recovery of iron ore concentrate with wet magnetic separation of grinded combined concentrate was developed (Fig. 2).

Preparation of the studied ore with grinding of the combined dry concentrate to the content of 63 % of the –0.071 mm grade and subsequent wet magnetic separation according to the proposed scheme allows to obtain an iron ore concentrate containing in %: 65.4 Fe, 0.01 Cu, 0.42 S, 2.7 Si, 0.95 Al. Zinc was not detected in the iron concentrate.

For the elaboration of the final scheme of ore processing with the definition of enrichment regimes and parameters, studies have been carried out that allow defining the possibility and expediency of flotation processing of the tailings obtained after wet magnetic separation. Magnetic separation tailings have the following composition, %: 0.2 Cu, 0.14 Zn, 3.5 S, 21.0 Fe, 8.9 Al, 13.4 Si. Analysis has shown that the copper content in the magnetic separation effluents increas-

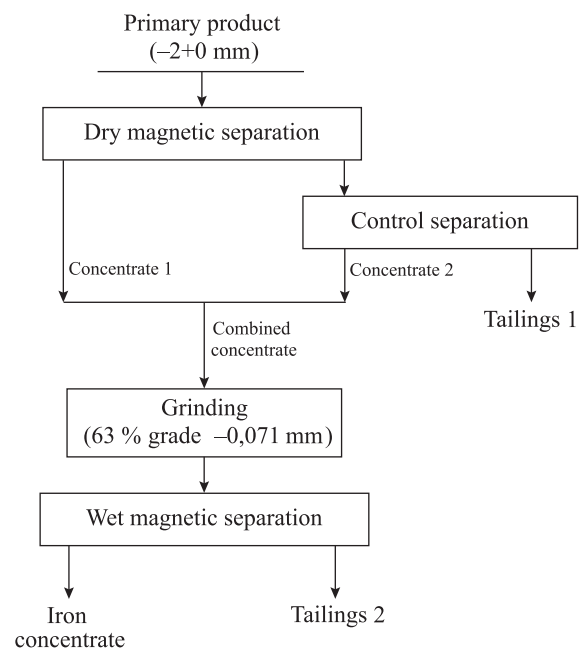


Fig. 2. Scheme of obtaining iron ore concentrate with wet magnetic separation

Рис. 2. Схема получения железорудного концентрата с мокрой магнитной сепарацией

es by more than 2 times and may be of economic interest.

The flotation experiments to determine the flotation and reagent regimes basic scheme were carried out according to a scheme that included the following operations: re-grinding of the combined magnetic separation tailings (dry and wet); the first base copper flotation with addition of lime carbonate, liquid glass, collector and foaming agent. In the second base flotation, 40 % of the reagents were fed from their consumption in the first main flotation.

Previously, tailings flotation with magnetic separation without re-grinding (50 % grade -0.071 mm) was carried out using butyl xanthate as collector at a consumption rate of 40 g/t in the first and 16 g/t in the second basic operation and foaming agent MIBK at consumption rates of 40 and 16 g/t, respectively, with a copper recovery rate in the common concentrate of 77 %. Grinding to a particle size of 75 % grade -0.071 mm grade increased the copper recovery rate to 83.3 %. The further increase of the fineness degree up to 95 % grade -0.071 mm did not lead to significant changes in the technological parameters of flotation. Therefore, in further flotation studies, the grinding mode was adopted up to a size of 75 % grade -0.071 mm.

The effect of the collector consumption rate on the flotation results for a total process time of 6 min is shown in Fig. 3. From the data presented, when the butyl xanthate consumption rate is increased up to 40 g/t, the copper extraction into concentrate reaches 88.3 % with a concentrate recovery of about 31 %. A further increase in the collector consumption rate does not have a significant impact on the flotation performance. The low copper content in a concentrate is connected with a high pyrite yield caused by its flotation activity.

Lime carbonate $\text{Ca}(\text{OH})_2$ was used for pyrite depression. The possibility of its delivery to different points of the technological process was studied. Introduction of the reagent in the flotation pulp did not lead to satisfactory results of flotation. The results of the study of the effect of lime in the grinding process on the results of flotation are shown in Fig. 4. Xanthates consumption rate during flotation was 40 g/t. MIBK was used as a foaming agent and its consumption rate was 40 g/t. From the data shown in Fig. 4, it can be seen that the addition of lime carbonate during grinding can increase the quality of the concentrate. The optimum consumption rate for lime carbonate was 9 kg/t ore — in this case, the copper content in the concentrate was 0.93 % and the extraction was 85 %. The increase in

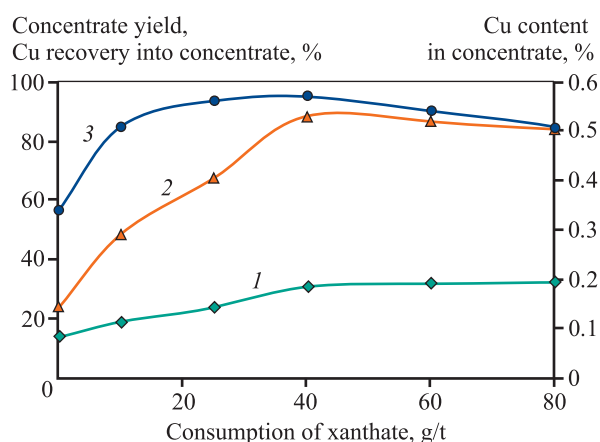


Fig. 3. Butyl xanthate consumption rate influence on concentrate yield (1), copper recovery (2) and its concentrate content (3) ($\tau_{\text{fl}} = 6$ min)

Рис. 3. Влияние расхода бутилового ксантогената на выход концентрата (1), извлечение меди в концентрат (2) и ее содержание в нем (3) ($\tau_{\text{фл}} = 6$ мин)

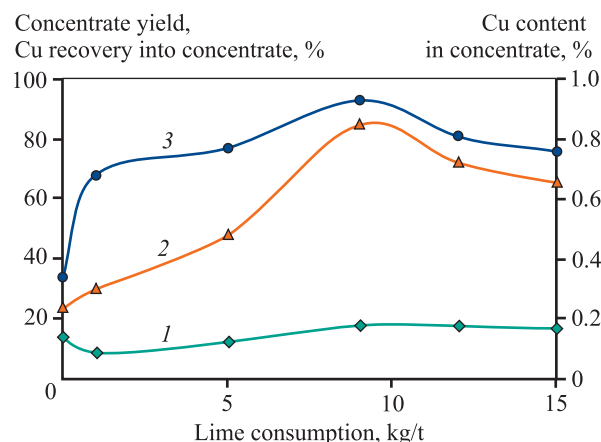


Fig. 4. $\text{Ca}(\text{OH})_2$ at grinding consumption rate influence on yield concentrate (1), copper recovery rate (2) and its content in concentrate (3) at flotation with butyl xanthate

Рис. 4. Влияние расхода $\text{Ca}(\text{OH})_2$ при измельчении на выход концентрата (1), извлечение меди в концентрат (2) и ее содержание в нем (3) при флотации бутиловым ксантогенатом

lime carbonate consumption leads to a decrease in copper extraction and its content in the concentrate. Thus, it can be seen that the alkaline environment created by the carbonate of lime further promotes the separation of the copper from the iron oxide [13].

The study of the influence of liquid glass on the depression of rock minerals was carried out with the consumption rates for xanthate — 40 g/t, lime — 800 g/t and MIBK — 40 g/t. The increase of liquid glass con-

sumption rate to 800 g/t results in a 2 % decrease of a concentrate recovery rate (from 17.1 to 15.3 %), also a 2 % decrease of copper recovery rate (from 71.8 to 69.6 %), but its content in a concentrate remains almost the same. At the same time, aluminum extraction decreases by 5 %, silicon extraction — by 6–7 %.

Fig. 5 shows the kinetics of copper sulfide flotation. It can be seen that after the 1st minute of flotation, the copper content in the concentrate is 3.5 % and the recovery rate is 73 %. During the first 3 minutes of flotation, 83 % of the copper is extracted, but the copper content in the combined concentrate decreases significantly. Thus, the time of the first basal flotation — 1 min, the second basal flotation — 2 min was accepted.

The results of the tests carried out with the application of xanthates with different length of hydrocarbon radical and structure in flotation for 1 min are shown in Fig. 6. The comparison of butyl and amyl xanthate shows that amyl has a stronger collecting power, which can be explained by the large size of the hydrocarbon radical. But in this case the quality of the concentrate decreases. The authors [14] used quantum chemical calculations to show that amyl xanthate binds more strongly to a mineral surface containing copper ions compared to other xanthates.

When comparing butyl and isobutyl as well as amyl and isoamyl xanthates, it was found that the isomerization of the hydrocarbon radical leads to a deterioration of the collection properties. This is consistent with the data from the paper [15] that the authors applied to pyrite: “Radical isomerization of hydrocarbons reduces the flotation activity of pyrite due to

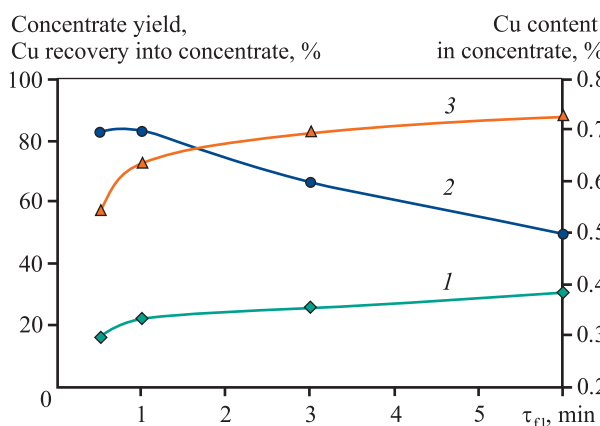


Fig. 5. Flotation with butyl xanthate kinetics

1 – concentrate yield, 2 – Cu content in concentrate, 3 – copper recovery in concentrate

Рис. 5. Кинетика флотации бутиловым ксантогенатом

1 – выход концентрата, 2 – содержание Cu в концентрате, 3 – извлечение меди в концентрат

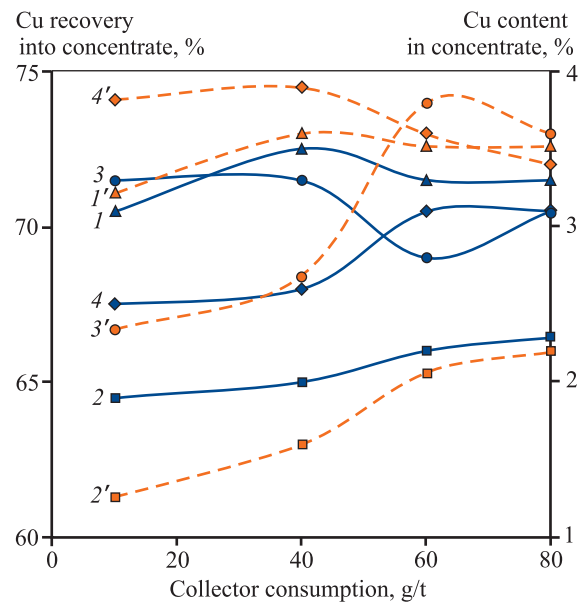


Fig. 6. Various xanthates and their consumption rate influence on copper extraction and its content in the concentrate

1, 1' – butyl xanthate; 2, 2' – isobutyl xanthate; 3, 3' – isoamyl xanthate; 4, 4' – amyl xanthate

Solid curves – content, dashed curves – extraction

Рис. 6. Влияние различных ксантогенатов и их расхода на извлечение меди в концентрат и ее содержание в нем

1, 1' – бутиловый ксантогенат; 2, 2' – изобутиловый; 3, 3' – изоамиловый; 4, 4' – амиловый

Сплошные кривые – содержание, штриховые – извлечение

the lower susceptibility of the collector to oxidation”. Comparing straight and branched chain compounds, the authors [16] concluded that branched chain xanthates higher homologues are less effective. Fig. 6 data shows that the most effective collector is butyl xanthate at a consumption rate of 40 g/t. When using it, the highest copper content in the concentrate is achieved.

Thiophosphates, thiophosphinates, thiocarbamates etc. are widely used to increase the flotation efficiency. These reagents are used for various sulfides in combination with xanthates and independently [17–23]. Our flotation studies with different collectors (Fig. 7) have shown that amyl aeroflot and Hostaflots have weaker collection properties compared to xanthates. Of the Hostaflots used, Hostafлот X-231 showed the strongest collection characteristics — at a consumption rate of 40 g/t copper, the extraction rate in concentrate was 54 % with an increase in grade in concentrate up to 3.6 %. Stronger collecting properties in comparison with Hostafлот were revealed in amyl aeroflot. The maximum copper content of 3.3 % at

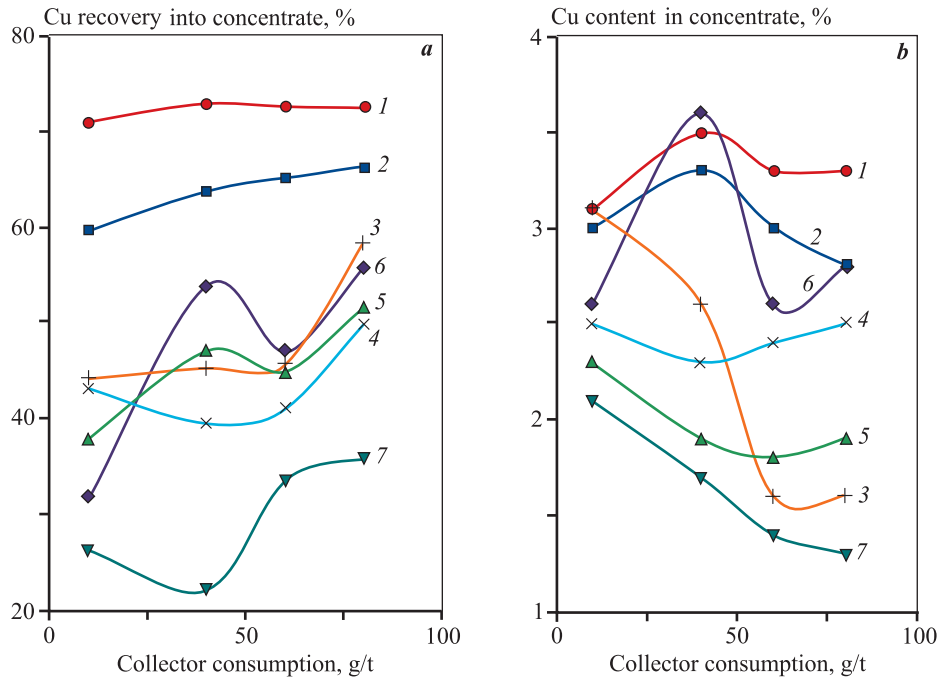


Fig. 7. Various collectors and their consumption rate influence on copper recovery (a) and its content (b) in a concentrate
 1 – butyl xanthate, 2 – Aeroflot, 3–7 – Hostafлот: 3 – 3403, 4 – LIB, 5 – X-023, 6 – X-231, 7 – 10093

Рис. 7. Влияние различных собирателей и их расхода на извлечение меди в концентрат (a) и ее содержание в нем (b)

1 – бутиловый ксантогенат, 2 – Аэрофлот, 3–7 – Хостафлот: 3 – 3403, 4 – LIB, 5 – X-023, 6 – X-231, 7 – 10093

extraction rate of 63.8 % was reached at the aeroflot consumption rate of 40 g/t. By increasing the aeroflot consumption rate, the extraction can be increased, but the quality of the concentrate decreases. At a similar consumption rate (40 g/t) of butyl xanthate, the copper extraction in the concentrate was 73 % at a content of 3.5 %.

In order to improve the efficiency of copper flotation, studies were carried out using a combination of xanthates with amyl aeroflot, as these collectors demonstrated the strongest collecting properties (see Fig. 7). Using one aeroflot reduced the copper recovery by 9 % and its content by 0.2 % (Fig. 8). A comparison of the results of flotation with one xanthogenate, one aeroflot and their combination shows that flotation with only one xanthogenate is preferable. Therefore, the further ore studying was carried out with use of butyl xanthate as collector at its consumption rate of 40 g/t.

Based on the flotation results after determining the optimum reagent consumption, flotation studies were carried out to improve the quality of the copper concentrate using post-purification procedures according to the scheme shown in Fig. 9. At that, the following reagent regime parameters were chosen:

– the first basal flotation: liquid glass – 800 g/t, butyl xanthate and MIBK – 40 g/t each, pH before flotation – 11.7, CaO_{free} – 0.47 g/L, flotation time – 1 min;

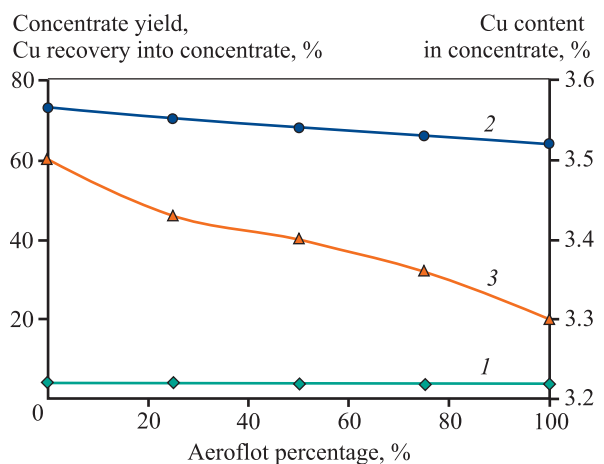


Fig. 8. Amyl aeroflot in a mixture with xanthate influence on concentrate yield (I), copper extraction (2) and its content in concentrate (3)

Рис. 8. Влияние амилового аэрофлота в смеси с ксантогенатом на выход концентрата (I), извлечение меди в концентрат (2) и ее содержание в нем (3)

Balance indicators of investigated ore enrichment

Балансовые показатели обогащения исследуемой руды

Product name	Output, %	Content, %		Extraction, %	
		Fe	Cu	Fe	Cu
Iron concentrate	54.60	65.4	0.01	80.0	5.9
Copper concentrate	0.33	26.5	15.2	0.2	54.0
Final tailings	45.07	20.0	0.08	19.8	40.1
Primary ore	100.00	44.7	0.093	100.0	100.0

— the second basal flotation: reagent consumption rate — 40 % of the consumption during the first basal flotation, pH before flotation — 11.5, CaO_{free} — 0.35 g/L, flotation time — 2 min;

— the recleaning flotation (1st and 2nd): lime carbonate — 330 g/t, CaO_{free} — 0.14 g/L, flotation time — 15 s.

The size of the magnetic separation tailings after regrinding with lime carbonate (9 kg/t) was 75 % grade — 0.071 mm. The basal and control flotations resulted in final tailings. The froth product of the basal flota-

tion was processed twice. The first recleaning tailings and the control flotation froth product were returned to the basal copper flotation and the chamber product of the second recleaning was fed to the first recleaning. The froth product of the second recleaning was copper concentrate with copper content of 15.2 % (KM-7 grade according to GOST R 52998-2008, group A32).

Thus, the scheme (Fig. 9) and the reagent regime of the flotation cycle for obtaining copper concentrate and tailings were developed according to the results of flotation of magnetic separation tailings of iron-containing ore. Copper concentrate contains %: 15.2 Cu, 26.5 Fe, 17.5 S, 3.47 Si, 1.4 Al and 8.5 Zn, which corresponds to KM-7 grade (GOST R 52998-2008, group A32). The final tailings have the following content of main components %: 0.08 Cu, 20.1 Fe, 0.25 S, 16.2 Si, 6.4 Al and 0.045 Zn.

Balance indicators of investigated ore enrichment are shown in the table.

Conclusion

1. The use of wet magnetic separation in deep grinding of iron ore allows obtaining iron ore concentrates with iron content of 65–66 % with its extraction of 79–80 %. Thus, the Si content does not exceed 2.2–2.5 %.

2. During magnetic enrichment of the ore under study, copper minerals concentrate in the tailings and the copper content in them increases from 0.093 to 0.2 %.

3. The application of the flotation method for the enrichment of magnetically separated tailings with their pre-grinding and the use of butyl xanthate makes it possible to obtain a conditioned copper concentrate of the quality KM-7 with a copper content of 15.2 %. The high efficiency of butyl xanthate in flotation of copper minerals is confirmed.

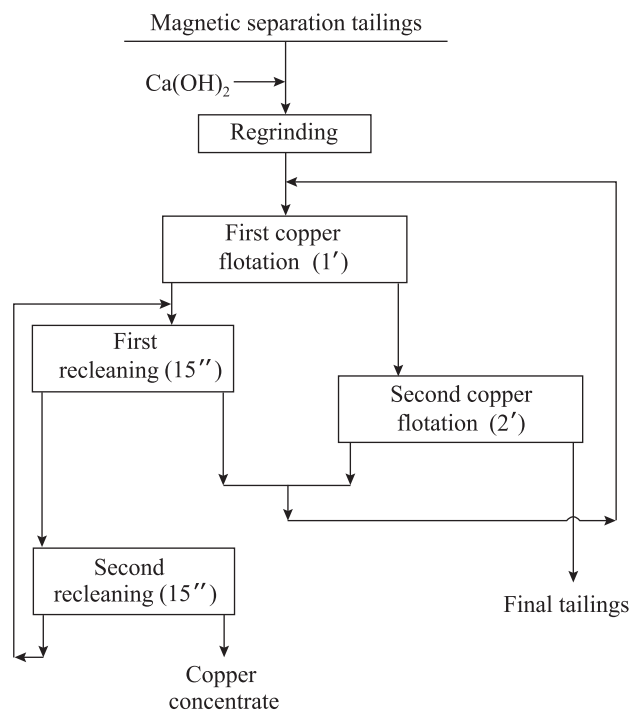


Fig. 9. Scheme of obtaining copper concentrate from magnetic separation tailings of iron ore

Рис. 9. Схема получения медного концентрата из хвостов магнитной сепарации железной руды

References

1. Karimova L.M. Combined method for processing off-balance copper sulfide ore. *Vestnik MGTU im. Nosova*. 2014; (2): 11–15. (In Russ.).
Каримова Л.М. Комбинированный метод переработки забалансовой медной сульфидной руды. *Вестник МГТУ им. Носова*. 2014; (2): 11–15.
2. Gorlova O.E., Yun A.B., Sinyanskaya O.M., Medyanik N.L. Combined processing of dumped complex copper ores of the Taskora deposit: process development and field trials. *Tsvetnye Metally*. 2018; (12): 14–20. (In Russ.).
Горлова О.Е., Юн А.Б., Сиянская О.М., Медяник Н.Л. Разработка и опытно-промышленные испытания комбинированной технологии переработки отвала труднообогатимых смешанных медных руд месторождения Таскора. *Цветные металлы*. 2018; (12): 14–20.
3. Jonović R., Avramović L., Stevanović Z., Jonović M. Technological investigations of sulphide oxidation from flotation tailings in order to increase the degree of copper leaching. *Mining and Metallurgy Engineering Bor*. 2014; (3): 153–160. <https://doi.org/10.5937/mmeb1403153j>
4. Bochkarev G.R., Pushkareva G.I., Rostovtsev V.I. Intensification of ore preparation and sorption extraction of metals from technogenic raw materials. *Fiziko-tekhnicheskie problemy razrabotki poleznykh iskopayemykh*. 2007; (3): 129–139. (In Russ.).
Бочкарев Г.Р., Пушкарева Г.И., Ростовцев В.И. Интенсификация процессов рудоподготовки и сорбционного извлечения металлов из техногенного сырья. *Физико-технические проблемы разработки полезных ископаемых*. 2007; (3): 129–139.
5. Chanturiya V.A., Bunin I.Zh. Non-traditional high-energy methods of disintegration and opening of finely dispersed mineral complexes. *Fiziko-tekhnicheskie problemy razrabotki poleznykh iskopayemykh*. 2007; (3): 107–128. (In Russ.).
Чантурия В.А., Бунин И.Ж. Нетрадиционные высокоэнергетические методы дезинтеграции и вскрытия тонкодисперсных минеральных комплексов. *Физико-технические проблемы разработки полезных ископаемых*. 2007; (3): 107–128.
6. Korostovenko V.V., Strekalova T.A., Korostovenko L.P., Kaplichenko N.M. Electrophysical methods in combined schemes of the main enrichment of sulfide ores. *Uspekhi sovremennogo estestvoznaniya*. 2018; (6): 84–89. (In Russ.).
Коростовенко В.В., Стрекалова Т.А., Коростовенко Л.П., Капличенко Н.М. Электрофизические методы в комбинированных схемах основного обогащения сульфидных руд. *Успехи современного естествознания*. 2018; (6): 84–89.
7. Gao M., Holmes R., Pease J. The latest developments in fine and ultrafine grinding technologies (Plenary). In: *XXIII International Mineral Processing Congress* (Istanbul, Turkey, 3–8 Sept. 2006). 2006; 1: 30–37.
8. Lavrinenko A.A., Sarkisova L.M., Shrader E.A., Chikhladze V.V., Shimkunas Ya.M. Investigation of the possibility of flotation extraction of sulfides from tailings of copper-nickel ores enrichment. *Gornyi informatsionno-analiticheskii byulleten'*. 2013; (2): 98–102. (In Russ.).
Лавриненко А.А., Саркисова Л.М., Шрадер Э.А., Чихладзе В.В., Шимкунас Я.М. Исследование возможности флотационного извлечения сульфидов из хвостов обогащения медно-никелевых руд. *Горный информационно-аналитический бюллетень*. 2013; (2): 98–102.
9. Yun A.B. Replenishment of the raw material base of the Zhezkazgan region through the use of new methods of extraction and processing of off-balance and low-grade ores. In: *Proceedings of National Center for the complex processing of mineral raw materials of the Republic of Kazakhstan*. Almaty, 2013. P. 335–348 (In Russ.).
Юн А.Б. Восполнение сырьевой базы Жезказганского региона за счет применения новых методов добычи и переработки забалансовых и бедных руд. В сб.: *Труды Национального центра по комплексной переработке минерального сырья Республики Казахстан*. Алматы, 2013. С. 335–348.
10. Kondratiev S.A. Reagents-collectors in the elementary act of flotation. Novosibirsk: Publ. of the Siberian Branch of the RAS, 2012. 241 p. (In Russ.).
Кондратьев С.А. Реагенты-собиратели в элементарном акте флотации. Новосибирск: Изд-во СО РАН, 2012. 241 с.
11. Lashkhiya V.Yu., Rudnev B.P. The method of enrichment of poor and off-balance silver-bearing sulfide ores and enrichment tailings: Pat. 2555280 (RF). 2015. (In Russ.).
Лашхия В.Ю., Руднев Б.П. Способ обогащения бедных и забалансовых серебряносодержащих сульфидных руд и хвостов обогащения: Пат. 2555280 (РФ). 2015. <https://patenton.ru/patent/RU2555280C1.pdf>
12. Bhaskar Raju G., Khangaonkar P.R. Electro-flotation of chalcopyrite fines. *International Journal of Mineral Processing*. 1982; 9 (2): 133–143.
13. Rao S.R., Finch J.A. Base metal oxide flotation using long chain xanthates. *International Journal of Mineral Processing*. 2003; 69 (1–4): 251–258. [https://doi.org/10.1016/S0301-7516\(02\)00130-8](https://doi.org/10.1016/S0301-7516(02)00130-8)
14. Bag B., Das B., Mishra B.K. Geometrical optimization of xanthate collectors with copper ions and their response to flotation. *Minerals Engineering*. 2011; 24 (8): 760–765. <https://doi.org/10.1016/j.mineng.2011.01.006>

15. Ignatkina V.A., Bocharov V.A., Dyachkov F.G. Study of the collecting properties of diisobutyl dithiophosphate during the flotation of sulfide minerals from pyrite ores. *Fiziko-tekhnicheskie problemy razrabotki poleznykh iskopaemykh*. 2013; (5): 138–146. (In Russ.).
Игнаткина В.А., Бочаров В.А., Дьячков Ф.Г. Исследование собирательных свойств диизобутилового дитиофосфината при флотации сульфидных минералов из колчеданных руд. *Физико-технические проблемы разработки полезных ископаемых*. 2013; (5): 138–146.
16. Ackerman P.K., Harris G.H., Klimpel R.R., Aplan F.F. Evaluation of flotation collectors for copper sulfides and pyrite. III. Effect of xanthate chain length and branching. *International Journal of Mineral Processing*. 1987; 21 (1–2): 141–156.
[https://doi.org/10.1016/0301-7516\(87\)90011-1](https://doi.org/10.1016/0301-7516(87)90011-1)
17. Hangone G., Bradshaw D., Ekmekci Z. Flotation of a copper sulphide ore from Okiep using thiol collectors and their mixtures. *Journal of the Southern African Institute of Mining and Metallurgy*. 2005; 105: 199–206.
18. Jianhua Chen, Zhenghe Xu, Ye Chen. Electronic structure and surfaces of sulfide minerals. In: *Density functional theory and applications*. 2020. P. 181–236.
<https://doi.org/10.1016/B978-0-12-817974-1.00005-3>
19. Noirant G., Benzaazoua M., Kongolo M., Bussière B., Frenette K. Alternatives to xanthate collectors for the desulphurization of ores and tailings: Pyrite surface chemistry. *Colloids and Surfaces A*. 2019; 577: 333–346.
<https://doi.org/10.1016/j.colsurfa.2019.05.086>
20. Mehdi Bazmandeh, Abbas Sam. Improvement of copper sulfide flotation using a new collector in an optimized addition scheme. *Physicochemical Problems of Mineral Processing*. 2021; 57 (6): 71–79.
<https://doi.org/10.37190/ppmp/142503>
21. Tijsseling L.T., Dehaine Q., Rollinson G.K., Glass H.J. Flotation of mixed oxide sulphide copper-cobalt minerals using xanthate, dithiophosphate, thiocarbamate and blended collectors. *Minerals Engineering*. 2019; 138: 246–256.
<https://doi.org/10.1016/j.mineng.2019.04.022>
22. Walter Amos Ngobeni, Gregory Hangone. The effect of using sodium di-methyl-dithiocarbamate as a co-collector with xanthates in the froth flotation of pentlandite containing ore from Nkomati mine in South Africa. *Minerals Engineering*. 2013; 54: 94–99.
<https://doi.org/10.1016/j.mineng.2013.04.027>
23. Corin K.C., Bezuidenhout J.C., O'Connor C.T. The role of dithiophosphate as a co-collector in the flotation of a platinum group mineral ore. *Minerals Engineering*. 2012; 36–38: 100–104.
<https://doi.org/10.1016/j.mineng.2012.02.019>

Information about the authors

Anatolii A. Lavrinenko — Dr. Sci. (Eng.), Chief Researcher, Head of the Laboratory of Complex Processing of Mineral Raw Materials of Non-Traditional of Institute of Complex Development of Mineral Resources n.a. acad. N.V. Melnikov of the Russian Academy of Sciences (IPKON RAS).
<https://orcid.org/0000-0002-7955-5273>
E-mail: lavrin_a@mail.ru

Oganes G. Lucinian — Cand. Sci. (Eng.), Leading Engineer of Laboratory of Complex Processing of Mineral Raw Materials of Non-Traditional, IPKON RAS.
<https://orcid.org/0000-0002-5655-1747>
E-mail: lusinyan.oganes@yandex.ru

Irina N. Kuznetsova — Cand. Sci. (Eng.), Senior Researcher of Laboratory of Complex Processing of Mineral Raw Materials of Non-Traditional, IPKON RAS.
<https://orcid.org/0000-0002-5980-8472>
E-mail: iren-kuznetsova@mail.ru

Vladimir G. Olennikov — Director of LLC NPF “Mashgeo”.
<https://orcid.org/0000-0003-1548-520X>
E-mail: ovg2007@mail.ru

Информация об авторах

Анатолий Афанасьевич Лавриненко — д.т.н., главный научный сотрудник, заведующий лабораторией комплексной переработки нетрадиционного минерального сырья, Институт проблем комплексного освоения недр им. акад. Н.В. Мельникова РАН (ИПКОН РАН).
<https://orcid.org/0000-0002-7955-5273>
E-mail: lavrin_a@mail.ru

Оганес Георгиевич Лусинян — к.т.н., ведущий инженер лаборатории комплексной переработки нетрадиционного минерального сырья, ИПКОН РАН.
<https://orcid.org/0000-0002-5655-1747>
E-mail: lusinyan.oganes@yandex.ru

Ирина Николаевна Кузнецова — к.т.н., старший научный сотрудник лаборатории комплексной переработки нетрадиционного минерального сырья, ИПКОН РАН.
<https://orcid.org/0000-0002-5980-8472>
E-mail: iren-kuznetsova@mail.ru

Владимир Григорьевич Оленников — директор ООО НПФ «Машгео».
<https://orcid.org/0000-0003-1548-520X>
E-mail: ovg2007@mail.ru

Contribution of the authors

A.A. Lavrinenko — formation of the main concept, goal and objectives of the study, writing the text, formulation of the conclusions.

O.G. Lucinian — conducting the calculations, testing the samples, preparing the text of the article.

I.N. Kuznetsova — conducting the experiments, processing of the research results, writing the text.

V.G. Olennikov — analysis of the research results, correction of the text and conclusions.

Вклад авторов

А.А. Лавриненко — формирование основной концепции, постановка цели и задачи исследования, подготовка текста, формулировка выводов.

О.Г. Лусинян — проведение расчетов, испытаний образцов, подготовка текста статьи.

И.Н. Кузнецова — проведение экспериментов, обработка результатов исследований, написание текста.

В.Г. Оленников — анализ результатов исследований, корректировка текста и выводов.

The article was submitted 23.03.2022, revised 29.04.2022, accepted for publication 11.05.2022

Статья поступила в редакцию 18.05.2022, доработана 29.07.2022, принята к публикации 02.08.2022

UDC 669.778 : 504.064

<https://doi.org/10.17073/0021-3438-2023-1-16-25>

Research article

Научная статья



The disposal of sulfide-arsenic cake

D.O. Novikov, L.I. Galkova, G.I. Maltsev**Institute of Metallurgy of Ural Branch of the Russian Academy of Sciences**

101 Amundsen str., Ekaterinburg, 620016, Russia

✉ Dmitrii O. Novikov (dm93nvk@gmail.com)

Abstract: When processing sulfide copper-zinc concentrates at copper smelters, sulfide-arsenic cakes are formed, which are subject to disposal. To solve the global environmental problem of arsenic in the metallurgical and mining industries, it must be reliably concentrated and fixed in technological flows with subsequent waste disposal. The fusion of arsenic cake with elemental sulfur leads to the formation of vitreous sulfides, which are less toxic in comparison with dispersed powdered cake, homogeneous and compact in shape. The fusion product is represented by non-stoichiometric arsenic sulfide, similar in composition to As_2S_5 . The high chemical stability of glassy arsenic sulfides is confirmed by the results of leaching by TCLP method. The fusion products have 100 times lower solubility compared to the initial cake. Achieving the solubility of arsenic in the alloy below the threshold concentration (5 mg/dm^3) makes it possible to recommend the disposal of arsenic cake by fusing it with elemental sulfur. The fusion products belong to non-hazardous waste and are suitable for long-term storage. The composition and structure of cake fusions with iron powder have been studied. New compounds of variable composition were identified in the fused samples: arsenides and sulfides of iron, arsenic sulfides and arsenopyrites. Studies have shown that the products of fusion with iron have a solubility 10–15 times lower than the arsenic compounds in the initial cake but above the threshold concentration as per TCLP method. Therefore, fusion with iron cannot be recommended for practical use for the disposal of arsenic cakes.

Key words: arsenic, sulfur, iron, arsenides, sulfides, oxides, structure, composition, sintering, leaching, cake, chemical analysis, concentration

Acknowledgments: The work was performed under the Comprehensive Program of Fundamental Research of UrB RAS (project No. AAAA-A18-118012590113-6) using the equipment of Collective Use Center “Ural-M” under IMET of the UrB RAS.

For citation: Novikov D.O., Galkova L.I., Maltsev G.I. The disposal of sulfide-arsenic cake. *Izvestiya. Non-Ferrous Metallurgy*. 2023; 29 (1): 16–25. (In Russ.). <https://doi.org/10.17073/0021-3438-2023-1-16-25>

Утилизация сульфидно-мышьяковистого кека

Д.О. Новиков, Л.И. Галкова, Г.И. Мальцев**Институт металлургии УрО РАН**

620016, Россия, г. Екатеринбург, ул. Амундсена, 101

✉ Дмитрий Олегович Новиков (dm93nvk@gmail.com)

Аннотация: При переработке сульфидных медно-цинковых концентратов на медеплавильных заводах образуются сульфидно-мышьяковистые кеки, подлежащие утилизации. Для решения глобальной экологической проблемы мышьяка в металлургической и горнодобывающей отраслях промышленности он должен быть надежно сконцентрирован и иммобилизован в технологических потоках с последующим удалением отходов. Сплавление мышьяковистого кека с элементарной серой приводит к образованию стекловидных сульфидов, которые менее токсичны в сравнении с дисперсным порошкообразным кеком, однородны и обладают компактной формой. Продукт сплавления представлен нестехиометрическим сульфидом мышьяка, близким по составу к As_2S_5 . Высокая химическая устойчивость стеклообразных сульфидов мышьяка подтверждается результатами выщелачивания по методике TCLP. Продукты сплавления имеют в 100 раз меньшую растворимость по сравнению с исходным кеком. Достижение растворимости мышьяка в сплаве ниже пороговой концентрации (5 мг/дм^3) позволяет

рекомендовать утилизацию мышьяковистого кека способом сплавления его с элементарной серой. Продукты сплавления относятся к неопасным отходам и пригодны для длительного хранения. Изучены состав и структура сплавов кека с железным порошком. В сплавленных образцах выявлены новые соединения переменного состава: арсениды и сульфиды железа, сульфиды мышьяка и арсенопириты. Исследования показали, что продукты сплавления с железом обладают растворимостью в 10–15 раз меньшей, чем соединения мышьяка в исходном кеке, но выше пороговой концентрации по методике TCLP. Поэтому сплавление с железом не может быть рекомендовано к практическому использованию для утилизации мышьяковистых кеков.

Ключевые слова: мышьяк, сера, железо, арсениды, сульфиды, оксиды, структура, состав, спекание, выщелачивание, кек, химический анализ, концентрация

Благодарности: Работа выполнена по государственному заданию ИМЕТ УрО РАН (№ государственной регистрации темы: 122020100404-2) с использованием оборудования Центра коллективного пользования «Урал-М».

Для цитирования: Новиков Д.О., Галкова Л.И., Мальцев Г.И. Утилизация сульфидно-мышьяковистого кека. *Известия вузов. Цветная металлургия*. 2023; 29 (1): 16–25. <https://doi.org/10.17073/0021-3438-2023-1-16-25>

Introduction

When processing sulfide copper-zinc concentrates at copper smelters, sulfide-arsenic cakes, being subject to disposal, are formed. To solve the global environmental problem of arsenic in the metallurgical and mining industries, it must be reliably concentrated and fixed in technological flows with subsequent waste disposal. A combination of cost-effective and selective physicochemical treatment methods such as ion exchange, leaching, precipitation, filtration and adsorption, along with biological methods, can constitute a safe alternative for the removal of arsenic from liquid and solid products to be purified. [1]. Arsenic immobilization stage can be performed by hydrometallurgical and pyrometallurgical methods. The initial stage of arsenic fixation is the oxidation of As(III) both to remove arsenic and to stabilize its final residues. Commonly, As(V) is precipitated using hydrometallurgical processes consisting of neutralization with lime, precipitation of sulfides, coprecipitation of arsenic with iron ions, including scorodite $\text{FeAsO}_4 \cdot 2\text{H}_2\text{O}$. In pyrometallurgical methods, arsenic and sulfur are captured using a fixing agent such as calcium and iron salts to obtain a stable residue. [2].

The separation of arsenic from solid-phase is possible through pressure oxidation leaching process ($2.5 \text{ mol/dm}^3 \text{ NaOH}$, $p(\text{O}_2) = 0.5 \text{ MPa}$, $t = 120 \text{ }^\circ\text{C}$, $L : S = 4$, $\tau = 3 \text{ h}$) and AsO_4^{3-} arsenate reduction to AsO_2^- arsenite with sulfur dioxide by $\sim 93 \%$ ($\text{pH} = 4$, $t = 30 \text{ }^\circ\text{C}$, $Q(\text{SO}_2) = 60 \text{ cm}^3/\text{min}$, $\tau = 2.5 \text{ h}$) [3]. The leaching of As_2O_3 by 89% with $100 \text{ g/dm}^3 \text{ Na}_2\text{S}$ solution is possible at $L : S = 6$, $t = 80 \text{ }^\circ\text{C}$ along with its precipitation from $\text{Fe}_2(\text{SO}_4)_3$, when 99.93% of arsenic is removed in the form of amorphous ferric arsenate at $\text{pH} = 4.8$, Fe^{3+}/As molar ratio = 5 and

$\text{H}_2\text{O}_2/\text{As} = 4$ [4]. Studies performed at the interface of precipitate and water suggest that the removal of As from the surface and deep layers is associated with the adsorption of As(V) by Fe oxides and the formation of a precipitate, and/or adsorption by Fe sulfides, respectively [5]. Arsenic adsorbed on hydrated ferric oxide (HFO) can redissolve as a result of the bioreactivated reductive dissolution of HFO at almost neutral pH with the corresponding oxidation of organic matter [6]. Calcium arsenates are also unstable and subject to transformation. When neutralizing CaO with different Ca/As ratios at $\text{pH} = 7\text{--}12$ in the presence of atmospheric CO_2 , the various types of crystalline calcium arsenate, which determine the stability of $\text{Ca}_3(\text{AsO}_4)_2$, are formed. When pH values increase from 8 to 10–12, the solubility of arsenic increases [7].

When sulfating hematite-rich calcines (56–62 % Fe_2O_3) with sulfuric acid, ferric sulfate solution ($13.4 \text{ g/dm}^3 \text{ Fe}$ and $2.3 \text{ g/dm}^3 \text{ As}$) was obtained and used for the precipitation of arsenic by $\sim 99.8 \%$ from waste waters (from $1,583.4$ to 5.3 mg/dm^3 of As). Arsenic carriers were ferric (aluminum) or calcium arsenate/arsenites (up to 72.8 % of As), as well as ferric oxyhydroxides [8]. Amorphous rather than crystalline arsenic trisulfide (As_2S_3) was unstable under alkaline and oxidizing conditions. The release of arsenic in the form of arsenite, which is subsequently oxidized to arsenate, and sulfur in the form of thiosulfate with a transition to sulfate by oxidation and disproportionation, increases upon the increase of pH, dissolved oxygen concentration and temperature [9].

Arsenic leaching from Zn–Pb mine tailings increased to a greater extent under acidic rather than alkaline ones, growing with an increase in the $L : S$ ra-

tio and duration of contact of the tailings with water, reaching a maximum for the samples with particle sizes of 500–600 and 150–250 μm [10]. Acid leaching combined with pressure oxidation was used to release 98.2 % of arsenic from lead plant fumes (100 g/dm^3 H_2SO_4 , $p(\text{O}_2) = 2.5 \text{ MPa}$, $t = 170 \text{ }^\circ\text{C}$, $L : S = 10$, $\tau = 2.5 \text{ h}$, $\omega = 500 \text{ r}/\text{min}$) [11]. Injection of calcium-based adsorbent into flue gases can ensure high arsenic removal efficiency. Further development of advanced adsorbents that are inexpensive, separable and suitable for recycling as well as resistant to high-temperature sintering and deactivation caused by the competitive adsorption of acid gases, having a large specific surface area, is to be the main focus of the future research [12].

Arsenate (2 mg/dm^3) is sorbed by ~85 % from aqueous solutions on 0.3 g/dm^3 CuFe_2O_4 within 90 min at $\text{pH} = 7$ [13]. Hydroxyl-Eggshell (ES-OH), being inexpensive chemical compound, removes arsenic from aqueous solutions in less than 15 min with a description of the process by a pseudo-second order model and a maximum As adsorption in 529 mg/dm^3 according to the Langmuir isotherm. The mechanism of As removal by means of ES-OH is caused by the precipitation of vladimirite $\text{Ca}_5(\text{HAsO}_4)_2(\text{AsO}_4)_2 \cdot 5\text{H}_2\text{O}$, which is followed by weak electrostatic interactions between precipitate and arsenate ions [14].

The pyrometallurgical roasting method is used for the treatment of dust with the addition of sulfuric acid and bitumen, for the reduction of As(V) and the oxidation of arsenic sulfides (consumption $\text{H}_2\text{SO}_4 = 0.2 \div 0.3 \text{ g}/\text{g}$, 5 % of carbon, $t = 300 \div 400 \text{ }^\circ\text{C}$, $\tau = 2 \div 3 \text{ h}$). About 98 % As was fumed, As content in the residue decreased to 0.57 %. The arsenic was eventually extracted as As_2O_3 with high purity of ~99.1 % [15].

The physical and chemical weathering of arsenic-rich industrial wastes can mobilize and disperse contaminated sediments in residential areas surrounding the industrial areas, putting humans at risk of chronic arsenic exposure. Arsenic content in mercury mine deposits (fraction $\leq 250 \mu\text{m}$) is 114–678 mg/kg [16]. The highest bioavailability of As (19–32 %) was established for the fraction of fine particles ($< 53 \mu\text{m}$), represented mainly by crystalline (30–73 %) and amorphous (9–59 %) Fe/Al oxyhydroxides [17]. The metabolic activity of microorganisms was the main reason for the transformation and mobilization of arsenic in the composition of wastes in landfills. Arsenate is reduced to arsenite and additionally methylated to mono- (MMA) and dimethylarsine (DMA) that decreases the total content of arsenic during the waste disposal process, but facilitates its release into the liquid phase in the form of arsenite, MMA and DMA [18].

The deposits in the pond for the discharge of metallurgical production wastes were studied. The content of water-soluble arsenic compounds, HCl and NaOH, was determined. It was established that the oxidation of As(III) and the processes of sorption and precipitation of As(V) proceed upon dissolution. The content of water-soluble As does not exceed 7.4 % of the total As in precipitates, As(III) is below 7.4 % of the extracted As content. The bulk of arsenic compounds (~78 % As) is dissolved in 2 M HCl, As(V) is ~94 % of the extracted arsenic [19].

Two different additives, namely a combination of calcite and ferric sulfate (CC + Fe(III)) and a by-product obtained from the processing of aluminum salt slags (BP– AlO_x), were used to stabilize As. Upon leaching, a decrease in the concentration of dissolved As by 95–98 and 52–79 % respectively was noted, which is acceptable for mine waste storage in controlled landfills. [20]. In order to stabilize arsenic-calcium residue (ACR) formed during the treatment of wastewater containing As during a year, it is treated with $\text{FeSO}_4\text{—H}_2\text{SO}_4$. Leaching results in the decrease of As concentration from 162 to 1.2 mg/dm^3 . The dissolution of As is stabilized by the formation of stable complexes Fe–O–As ($\text{FeAsO}_4 \cdot x\text{Fe}(\text{OH})_3$) [21]. The surface of nanosilica (~18 nm) was modified with a silane coupling agent containing a mercapto group and iron (II) salt to obtain an organic-inorganic hybrid containing –S–Fe–S (RNS-SFE) functional group. At a dosage of 3.0 wt.% RNS-SFE, it can immobilize bioavailable Pb, Cd and As by 97.1 %, 85.0 % and 80.1 %, respectively. Elements form insoluble compounds of mercaptometals (–S–Pb–S– and –S–Cd–S–) and less soluble ferric arsenate ($\text{Fe}_3(\text{AsO}_4)_2$, FeAsO_4), precipitating on the surface of nanosilica particles. Immobilized products Pb, Cd and As exhibit good resistance to acid leaching [22].

Notwithstanding previously performed studies, there remains a need for the development of new, relatively inexpensive and efficient ways to immobilize arsenic contained in intermediate products and industrial waste. The purpose of this paper is to justify a method for the thermal treatment of sulfide-arsenic cakes with elemental sulphur and iron so as to reduce the solubility of arsenic in long-term storage and disposal conditions.

Methods and materials

The chemical composition of initial materials and reaction products was determined by atomic emission spectroscopy by means of Spectroflame Modula S

spectrometer (Spectro Analytical Instruments GmbH, Germany). *X*-ray spectral microanalysis (XSMA) of the samples was performed on EVO 40 XVP scanning electron microscope (Carl Zeiss, Germany) and INCA Energy 350 X-max 80 energy-dispersive *X*-ray spectrometer (Oxford Instruments, UK). *X*-ray phase analysis (XPA) of the formed products was performed on Dron 2.0 diffractometer (“Burevestnik” Research and Production Enterprise, St. Petersburg) with UVD-2000 high-temperature attachment ($\text{CuK}\alpha$ radiation, graphite monochromator, Bragg–Brentano focusing), angle interval of $2\theta = 15.0\div 80.0^\circ$, film step of 0.02° , exposure time of 2 s). ICDD PDF-4 database was used to interpret radiographs [23].

Waste toxicity was characterized using Toxicity Characteristic Leaching Procedure (TCLP) [24, 25] developed by the US Environmental Protection Agency (EPA). The aforementioned method is based on the leaching of a solid sample under conditions simulating its presence in dumps. Leaching was performed on an agitator platform in sodium acetate buffer solution ($\text{pH} = 4.93$) with the ratio of S : L = 1 : 20, the agitation speed of 30 r/min and temperature of 25°C for 18 h. After filtration in the solution, the concentration of arsenic was determined and compared with the table presented by EPA, containing maximum concentrations of the toxic substance. The current TCLP threshold concentration of arsenic is 5 mg/dm^3 .

The object of the study was sulfide-arsenic cake of sulfuric acid production of the following composition, %: 55.3 As; 33.6 S; 2.58 Pb; 0.58 Zn; 0.18 Sb; 0.18 Se; 0.16 Cd; 0.097 Cu; 0.064 Fe; 0.034 Si; 0.21 Na available from “SUMZ”, OJSC (Revda city, the Sverdlovsk Region) [26]. The experiments were performed by fusing a mixture of sulfide-arsenic cake with the addition of elemental sulfur and iron. Pyrrhotite mineral (a piece), fused iron (a piece) and reduced iron powder were used as an iron-containing material. Charge fusion equipment: resistance furnace with graphite carbon heater (Tamman furnace), SNOL tube furnace and muffle furnace. Fuse mode: temperature $370\text{--}500^\circ\text{C}$, time $0.25\text{--}2.0\text{ h}$. To maintain inert atmosphere in the furnace, argon or nitrogen was supplied onto the charge surface at a flow rate of $\sim 2\text{ dm}^3/\text{h}$. The consumption of elemental sulfur was $5\text{--}50\%$, and the consumption of iron (powder) was $50\text{--}200\%$ of the cake weight. The mixture was thoroughly mixed and placed in a porcelain crucible with a lid, which was placed into the preheated furnace. After heating the charge to a predetermined temperature and keeping it for a controlled period of time, the furnace was turned off, cooled, and the crucible was taken out. The products were

weighed, ground to a particle size of less than 1 mm, analyzed by *X*-ray phase analysis, electron microscopy and *X*-ray spectral microanalysis, and the solubility of As in water and buffer solution was determined using TCLP method.

Results and discussion

The results of our studies of the microstructure and phase composition of the sulfide-arsenic cake were previously described in detail [26]. According to XRF results, the cake is represented by *X*-ray amorphous dispersed arsenic sulfide (As_2S_3), lead sulfate (PbSO_4) and arsenic oxide (As_2O_3) reflections were detected. The microanalysis of cake particles showed their heterogeneity both in structure and composition. According to XSMA data, individual sulfates and sulfides of lead and zinc were found in the cake. The phases characterizing aggregates of complex composition containing iron and lead sulfides, arsenic, zinc, copper, silicon oxide, etc. were detected at the points of local probing. A significant part of the aggregates contains non-stoichiometric arsenic sulfides of As_2S_x type, where $x = 3.1\div 3.8$, with small inclusions of arsenic and copper oxides.

Testing the cake for solubility exhibits that the content of acid-soluble arsenic forms is 19166 mg/kg , and the content of water-soluble arsenic forms is 132 mg/kg . The cake leaching in water/buffer solution (under TCLP method) indicated that the liquid phase contains (mg/dm^3) 170/334 As; 1200/1240 S; 150/180 Zn; 3.1/0.4 Pb. The data obtained are many times higher than threshold concentrations of arsenic.

For the purpose of preselecting the cake processing mode, the thermodynamic modeling (TDM) of phase transformations upon cake heating was performed. The calculations were made per 100 kg of the weight of the working medium containing (%) 90 As_2S_3 , 8.7 PbSO_4 and 1.3 CuS , with a composition approximating that of the arsenic cake base. The TDM results indicate a significant effect of temperature on the phase composition. The transformation of the initial compounds occurs, the metal occurrence form changes. In particular, most As_2S_3 is transformed into other sulfides and arsenic oxide. When the temperature of $370\text{--}380^\circ\text{C}$ is reached, the most significant of the formed phases are as follows: AsS, PbS, CuS, As_2S_3 , As_2S_2 . Sulfur is distributed among metal compounds, copper and arsenic are found in the lower sulfides of the same denomination. In the temperature range of $25\text{--}500^\circ\text{C}$, a sequential transformation of As_2S_3 into AsS, As_2S_2 , As_2O_3 , As, As_4S_4 occurs. The increase in

the amount of As_2O_3 can be explained by the following interaction:

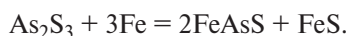
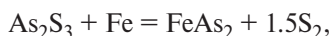
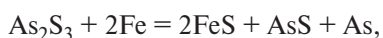
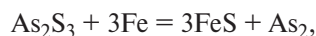
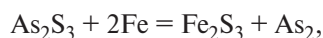


The phase formation when heating the working medium in a mixture with elemental sulfur was evaluated with the addition of sulfur in the amounts of 5, 50 and 200 %. Upon the heat treatment of the charge, some part of sulfur transforms into the gas phase, and the other part reacts with arsenic sulfide at a temperature of 120–150 °C:



A decrease in the amount of As_2S_3 , the appearance and growth of the proportion of other sulfides, AsS , As_2S_2 are observed during the charge heating. An increase in the amount of added elemental sulfur from 5 to 50 % almost does not change the pattern, and when it is added in the amount of up to 200 %, the transition of sulfur into the gas phase increases and the amount of newly formed arsenic sulfides decreases. The results of thermodynamic prediction revealed that the optimal addition of elemental sulfur is 5–10 % minimum, which allows to quantitatively bind arsenic into a poorly soluble non-toxic compound.

Heat treatment of the system consisting of a charge with iron revealed that iron reacts with arsenic sulfide resulting in the formation of secondary sulfides. Some of the possible interactions are as follows:



The number of Fe_2S_3 , FeS_2 , FeAs compounds decreases at the predicted cake processing temperatures of 400–450 °C. FeAs_2 , FeS , and AsS compounds quantitatively increase by the indicated temperatures, non-stoichiometric sulfide $\text{Fe}_{0.877}\text{S}$ and arsenopyrite FeAsS are formed as well. According to TDM results, the optimal addition of iron (~14 wt.%) results in the transition of arsenic-containing cake phases into such mineral forms as arsenides and arsenopyrites that correspond to the criteria of chemical inertness. Technological experiments on the heat treatment of a mixture of cake with additives revealed that the cake transforms into a compact glassy state after being fused with sulfur at a temperature of 420 °C (Fig. 1).

According to the performed calculations, it can be assumed that with an increase in the amount of added sulfur upon fusion, the form of arsenic changes from initial As_2S_3 to As_2S_5 and As_2S_7 , which is consistent with the results of thermodynamic analysis and XSMA. At the points of local probing (Fig. 2, Table 1), the phases of non-stoichiometric arsenic sulfide $\text{As}_2\text{S}_{4,6}$ and lead sulfate, including its non-stoichiometric composition, were detected.

Testing of fusions for toxicity by TCLP method (Table 2) revealed that a small addition of sulfur (5 %) reduces the solubility of arsenic by an order of magnitude, and an increase in sulfur to 20 % reduces the solubility of arsenic below the threshold concentration (3.7–3.3 mg/dm³), which allows to perform the disposal of fusions without special measures.

Preliminary experiments ensured the establishment of a temperature of 400–440 °C for the fusion of sulfide-arsenic cake with iron allowing to prevent losses with fumes. The heat treatment with iron presented in different variants was performed at a temperature of 400 °C for 2 h. The iron/cake ratio was 0.6/1.0, but a layer of iron was added to the surface of the reaction mix-

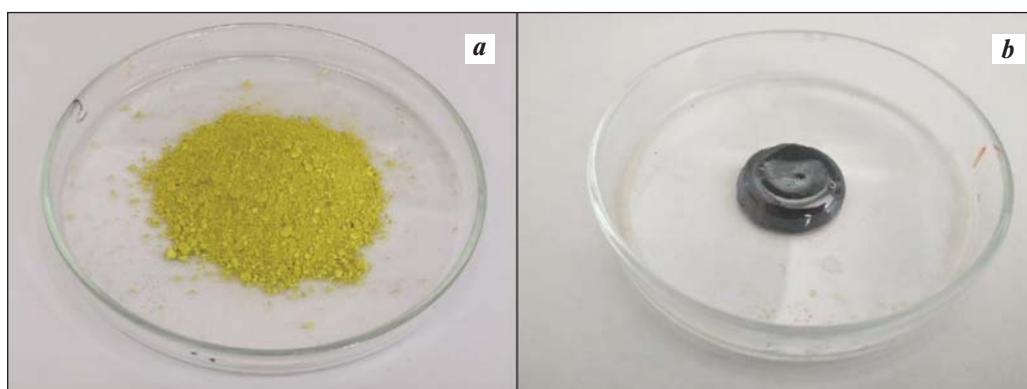


Fig. 1. The view of the cake before (a) and after (b) the fusion with sulfur

Рис. 1. Вид кека до (a) и после (b) сплавления с серой

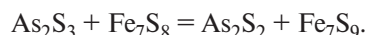
Table 1. The composition of the phases of the sample after fusion of the cake with 20 % S (as per Fig. 2)

Таблица 1. Состав фаз образца после сплавления кека с 20 % S (по рис. 2)

Point No.	Composition, wt. %					Phase composition
	As	S	O	Pb	Zn	
1	50.87	49.13	–	–	–	As ₂ S _{4,6}
2	48.98	50.52	–	–	0.5	As ₂ S _{4,6}
3	–	11.98	20.79	67.23	–	PbSO ₄
4	–	12.84	14.97	71.55	0.64	PbS _{1,2} O _{2,7}
5	50.55	49.45	–	–	–	As ₂ S _{4,6}
6	22.19	28.48	–	49.33	–	PbAs _{1,2} S _{3,8}

ture (300 % of the mixture) in the experiment with iron powder.

Upon the heat treatment of cake mixed with iron sulfide Fe₇S₈ (pyrrhotite), the phases of non-stoichiometric sulfide Fe₇S_x, where x = 8.7; 9.0; 9.5, were identified at the interface with the latter (Table 3). The saturation of initial Fe₇S₈ with sulfur can be observed. The following interaction might occur:



The chemical composition of the phases at the points of probing was determined by XSMAs of the cake surface after heat treatment with molten iron (Table 4)

Such compounds of variable composition as sulfides of lead, iron and arsenic, oxysulfides of iron and sulfur, arsenopyrites FeAsSz, etc. were found in the fusion products.

Experiments for the fusion of cake with iron powder were performed with its consumption from 50 to 200 % of the cake mass (Tables 5, 6). The obtained

fusions were subjected to a toxicity test. With iron consumption of ~60÷80 %, the solubility of arsenic in the buffer solution decreases by an order of magnitude compared to the initial cake, but its concentration in the solution remains high and significantly exceeds the threshold.

Table 2. The results of leaching of samples after fusion with sulfur

Таблица 2. Результаты выщелачивания образцов после сплавления с серой

Sulfur addition, %	Concentration in solution, mg/dm ³	
	As	S
0	70.0	117.0
5	7.2	51.2
20	3.7	52.9
40	3.6	54.7
50	3.3	52.1

Table 3. The composition of fusion phases at the interface with iron sulfide

Таблица 3. Состав фаз сплава на границе с сульфидом железа

Phase	S, %	Fe, %	Phase composition
1	41.6	58.4	Fe ₇ S _{8,7}
2	42.19	57.81	Fe ₇ S ₉
3	43.53	56.47	Fe ₇ S _{9,5}

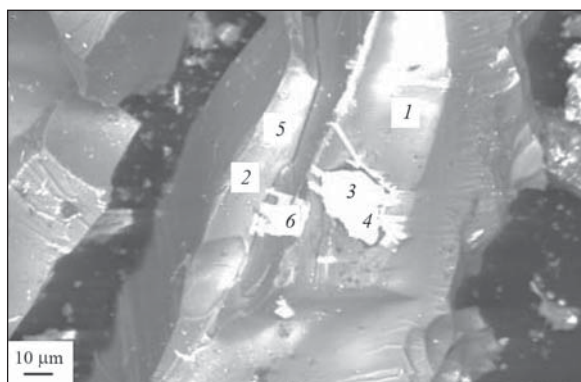


Fig. 2. The microstructure of cake fusion

Рис. 2. Микроструктура сплава кека

Table 4. The chemical composition (%) of the phases of cake fusion with iron

Таблица 4. Химический состав (%) фаз сплава кека с железом

Phase	S	Cu	Fe	As	Pb	O	Phase composition
1	22.63	–	–	19.45	43.3	8.51	PbAsS ₃ O ₃
2	23.47	–	7.37	9.86	53.85	–	FeAsS PbS
3	29.77	–	70.23	–	–	–	FeS
4	22.88	1.58	9.81	14.42	23.79	16	As ₂ S ₄ O ₃ PbFeO ₃
5	24.96	4.2	4.78	14.31	–	27.9	AsS ₄ O ₆

Table 5. The results of cake fusion with iron powder

Таблица 5. Результаты по сплавлению кека с порошковым железом

Iron consumption, %	Loss of weight, %	As concentration in solution, mg/dm ³	Fraction after leaching, wt. %	
			As	S
0	4.9	110	–	–
80	8.2	38	47.35	40.5
120	6.6	76	49.66	39.1
170	3.9	90	47.30	38.5
200	9.6	81	51.00	37.1

Such compounds of variable composition as sulfides of lead and iron of Fe_xS_y type, where $x = 1\div 2$, $y = 1\div 3$; arsenic sulfides As_mS_n, where m and n vary from 1 to 4, oxysulfides of iron and sulfur of FeS₂O₄ and FeS₃O₅ type, as well as the ones of arsenic and sulfur As₂S₂O₅; arsenates Fe_pAs_q, where p and q vary with 1–2; arsenopyrites FeAsS_z, where $z = 1\div 4$, were identified in the products of cake fusion with iron powder. An oxygen compound FeAsO₄, being one of the most stable arsenic compounds, was identified as well. It was established that the composition of the fusion products varies over a wide range. The possibility of binding arsenic into poorly soluble compounds (arsenopyrites, FeAsO₃, FeAsO₄, etc.) in autoclaving processes is known. The formation of poorly soluble compounds in the process of cake fusion with iron can facilitate reducing its solubility and transfer the cake from the category of hazardous wastes to the category of non-hazardous ones.

Conclusion

The fusion of arsenic cake with elemental sulfur results in the formation of vitreous sulfides, which are less toxic compared to dispersed powder cake, homogene-

Table 6. Chemical composition (%) at the points of probing of cake fusion with iron powder (according to XSM data)

Таблица 6. Химический состав (%) в точках зондирования сплава кека с порошком железа (по данным РСМА)

Point No.	O	S	Fe	Pb	As
1	6.46	21.35	48.58	12.39	5.86
2	28.56	13.10	5.19	7.61	33.48
3	10.16	20.48	53.95	2.41	11.54
4	11.93	26.06	52.65	–	8.46

ous and compact in shape. The fusion product is in the form of a non-stoichiometric arsenic sulfide, being close in composition to As₂S₅. The high chemical stability of vitreous arsenic sulfides is confirmed by the results of leaching by TCLP method. The fusion products are 100 times less soluble than the initial cake. Obtaining the solubility of arsenic in the fusion below the threshold concentration (5 mg/dm³) makes it possible to recommend the disposal of arsenic cake by transforming ar-

senic into poorly soluble compounds through its fusion with elemental sulfur. The fusion products are classified as non-hazardous wastes and are suitable for long-term storage.

The composition and structure of cake fusions with iron were studied. Such new compounds of variable composition as arsenides and iron sulfides, arsenic sulfides and arsenopyrites, etc. are found in the fused products. Experiments on cake fusion with iron revealed the possibility of transforming arsenic into poorly soluble compounds (arsenides and arsenopyrites), which results in a decrease in the fusion solubility and toxicity. Under the experimental conditions, a decrease in the solubility of the fusion products by 10–15 times with respect to the initial cake with the test concentration of arsenic in the solution above the threshold, was obtained. At the completed stage, iron-containing reagents cannot be recommended for the technology of disposal of arsenic cake by transforming arsenic into poorly soluble compounds.

References

1. Singh P., Borthakur A., Singh R., Bhadouria R., Singh V.K., Devi P. A critical review on the research trends and emerging technologies for arsenic decontamination from water. *Groundwater for Sustainable Development*. 2021; 14: 100607. <https://doi.org/10.1016/j.gsd.2021.100607>
2. Nazari A.M., Radzinski R., Ghahreman A. Review of arsenic metallurgy: Treatment of arsenical minerals and the immobilization of arsenic. *Hydrometallurgy*. 2017; 174: 258–281. <https://doi.org/10.1016/j.hydromet.2016.10.011>
3. Liu W., Huang C., Han J., Qin W. Removal and reuse of arsenic from arsenic-bearing purified residue by alkaline pressure oxidative leaching and reduction of As(V). *Hydrometallurgy*. 2021; 199: 105541. <https://doi.org/10.1016/j.hydromet.2020.105541>
4. Shahnazi A., Firoozi S., Haghshenas Fatmehsari D. Selective leaching of arsenic from copper converter flue dust by Na_2S and its stabilization with $\text{Fe}_2(\text{SO}_4)_3$. *Transactions of Nonferrous Metals Society of China*. 2020; 30 (6): 1674–1686. [https://doi.org/10.1016/S1003-6326\(20\)65329-8](https://doi.org/10.1016/S1003-6326(20)65329-8)
5. Duan L., Song J., Yin M., Yuan H., Li X., Zhang Y., Yin X. Dynamics of arsenic and its interaction with Fe and S at the sediment-water interface of the seasonal hypoxic Changjiang Estuary. *Science of the Total Environment*. 2021; 769: 145269. <https://doi.org/10.1016/j.scitotenv.2021.145269>
6. Raju N.J. Arsenic in the geo-environment: A review of sources, geochemical processes, toxicity and removal technologies. *Environmental Research*. 2022; 203: 111782. <https://doi.org/10.1016/j.envres.2021.111782>
7. Zhang D., Wang S., Wang Y., Gomez M.A., Jia Y. The longterm stability of calcium arsenates: Implications for phase transformation and arsenic mobilization. *Journal of Environmental Sciences*. 2019; 84: 29–41. <https://doi.org/10.1016/j.jes.2019.04.017>
8. Mendes H.L., Caldeira C.L., Ciminelli V.S.T. Arsenic removal from industrial effluent: In-situ ferric sulfate production and arsenic partitioning in the residues. *Minerals Engineering*. 2021; 169: 106945. <https://doi.org/10.1016/j.mineng.2021.106945>
9. Mirazimi M., Mohammadi M., Liu W. Kinetics and mechanisms of arsenic and sulfur release from crystalline orpiment. *Minerals Engineering*. 2021; 170: 107032. <https://doi.org/10.1016/j.mineng.2021.107032>
10. Akhavan A., Golchin A. Estimation of arsenic leaching from Zn–Pb mine tailings under environmental conditions. *Journal of Cleaner Production*. 2021; 295: 126477. <https://doi.org/10.1016/j.jclepro.2021.126477>
11. Li W., Han J., Liu W., Jiao F., Wang H., Qin W. Separation of arsenic from lead smelter ash by acid leaching combined with pressure oxidation. *Separation and Purification Technology*. 2021; 273: 118988. <https://doi.org/10.1016/j.seppur.2021.118988>
12. Wang Y., Yu J., Wang Z., Liu Y., Zhao Y. A review on arsenic removal from coal combustion: Advances, challenges and opportunities. *Chemical Engineering Journal*. 2021; 414: 128785. <https://doi.org/10.1016/j.cej.2021.128785>
13. Huang Y., Li X., Zhang C., Dai M., Zhang Z., Xi Y., Quan B., Lu S., Liu Y. Degrading arsenic acid and adsorbing the released inorganic arsenic simultaneously in aqueous media with CuFe_2O_4 activating peroxymonosulfate system: Factors, performance, and mechanism. *Chemical Engineering Journal*. 2021; 424: 128537. <https://doi.org/10.1016/j.cej.2021.128537>
14. Ribeiro I.C.A., Vasques I.C.F., Teodoro J.C., Guerra M.B.B., Carneiro J.S.S., Melo L.C.A., Guilherme L.R.G. Fast and effective arsenic removal from aqueous solutions by a novel low-cost eggshell byproduct. *Science of the Total Environment*. 2021; 783: 147022. <https://doi.org/10.1016/j.scitotenv.2021.147022>
15. Zhang W., Che J., Xia L., Wen P., Chen J., Ma B., Wang C. Efficient removal and recovery of arsenic from copper smelting flue dust by a roasting method: Process optimization, phase transformation and mechanism investigation. *Journal of Hazardous Materials*. 2021; 412: 125232. <https://doi.org/10.1016/j.jhazmat.2021.125232>
16. O'Connor K.P., Montgomery M., Rosales R.A., White-man K.K., Kim C.S. Wetting/drying cycles increase arsenic bioaccessibility in mine-impacted sediments. *Science*

- of the *Total Environment*. 2021; 774: 145420.
<https://doi.org/10.1016/j.scitotenv.2021.145420>
17. Bari A.S.M.F., Lamb D., Choppala G., Seshadri B., Islam M.R., Sanderson P., Mohammad P., Rahman M. Arsenic bioaccessibility and fractionation in abandoned mine soils from selected sites in New South Wales, Australia and human health risk assessment. *Ecotoxicology and Environmental Safety*. 2021; 223: 112611.
<https://doi.org/10.1016/j.ecoenv.2021.112611>
 18. Hu L., Nie Z., Wang W., Zhang D., Long Y., Fang C. Arsenic transformation behavior mediated by arsenic functional genes in landfills. *Journal of Hazardous Materials*. 2021; 403: 123687.
<https://doi.org/10.1016/j.jhazmat.2020.123687>
 19. Lihareva N. Arsenic solubility, mobility and speciation in the deposits from a copper production waste storage. *Microchemical Journal*. 2005; 81(2): 177–183.
<https://doi.org/10.1016/j.microc.2004.12.006>
 20. Álvarez-Ayuso E., Murciego A. Stabilization methods for the treatment of weathered arsenopyrite mine wastes: Arsenic immobilization under selective leaching conditions. *Journal of Cleaner Production*. 2021; 283: 125265.
<https://doi.org/10.1016/j.jclepro.2020.125265>
 21. Li E., Yang T., Wang Q., Yu Z., Tian S., Wang X. Long-term stability of arsenic calcium residue (ACR) treated with FeSO₄ and H₂SO₄: Function of H⁺ and Fe(II). *Journal of Hazardous Materials*. 2021; 420: 126549.
<https://doi.org/10.1016/j.jhazmat.2021.126549>
 22. Cao P., Qiu K., Zou X., Lian M., Liu P., Niu L., Yu L., Li X., Zhang Z. Mercapto propyltrimethoxysilane- and ferrous sulfate-modified nano-silica for immobilization of lead and cadmium as well as arsenic in heavy metal-contaminated soil. *Environmental Pollution*. 2020; 266(3): 115152.
<https://doi.org/10.1016/j.envpol.2020.115152>
 23. Powder Diffraction File (PDF), produced by the International Centre for Diffraction Data, Newtown Square, PA. URL: <http://www.icdd.com/index.php/pdfsearch> (accessed: 05.07.2019).
 24. Bluteau M.C., Demopoulos G.P. The incongruent dissolution of scorodite—solubility, kinetics and mechanism. *Hydrometallurgy*. 2007; 87 (3–4): 163–177.
 25. Davis S. Regulated metals: the rule of 20. Pollution Prevention Institute, Kansas SBEAP, 2001.
 26. Selivanov E.N., Novikov D.O., Galkova L.I. Structure of arsenic sulfide cake and solubility of its alloys with sulfur. *Metallurgist*. 2021; 65 (1): 228–236.

Information about the authors

Dmitrii O. Novikov – Cand. Sci. (Eng.), Junior Researcher of the Laboratory of Non-Ferrous Metals Pyrometallurgy of the Institute of Metallurgy (IMET) of Ural Branch of the Russian Academy of Sciences (UrB RAS).
<https://orcid.org/0000-0001-9201-4044>
 E-mail: dm93nvk@gmail.com

Lyudmila I. Galkova – Cand. Sci. (Eng.), Senior Researcher of the Laboratory of Non-Ferrous Metals Pyrometallurgy of IMET of the UrB RAS.
<https://orcid.org/0000-0002-0133-9079>
 E-mail: galkowa@mail.ru

Gennadii I. Maltsev – Dr. Sci. (Eng.), Cand. Sci. (Chem.), Senior Researcher of the Laboratory of Non-Ferrous Metals Pyrometallurgy of the IMET of the UrB RAS.
<https://orcid.org/0000-0002-0750-0070>
 E-mail: maltsewg@yandex.ru

Информация об авторах

Дмитрий Олегович Новиков – к.т.н., младший научный сотрудник лаборатории пирометаллургии цветных металлов Института металлургии (ИМЕТ) УрО РАН.
<https://orcid.org/0000-0001-9201-4044>
 E-mail: dm93nvk@gmail.com

Людмила Ивановна Галкова – к.т.н., старший научный сотрудник лаборатории пирометаллургии цветных металлов ИМЕТ УрО РАН.
<https://orcid.org/0000-0002-0133-9079>
 E-mail: galkowa@mail.ru

Геннадий Иванович Мальцев – д.т.н., к.х.н., старший научный сотрудник лаборатории пирометаллургии цветных металлов ИМЕТ УрО РАН.
<https://orcid.org/0000-0002-0750-0070>
 E-mail: maltsewg@yandex.ru

Contribution of the authors

D.O. Novikov – provision of the resources, preparation and management of the experiments, conducting the experiments, formation of the main concept, goal and objectives of the study; writing the text, formulation of the conclusions.

L.I. Galkova – scientific guidance, correction of the text and conclusions, processing of the research results, conducting the calculations.

G.I. Maltsev – analysis of the research results, writing the text.

Вклад авторов

Д.О. Новиков – обеспечение ресурсами, подготовка и проведение экспериментов, формирование основной концепции, постановка цели и задачи исследования, подготовка текста, формулировка выводов.

Л.И. Галкова – научное руководство, корректировка текста, корректировка выводов. обработка результатов исследований, проведение расчетов.

Г.И. Мальцев – анализ результатов исследований, подготовка текста статьи.

The article was submitted 28.02.2022, revised 17.05.2022, accepted for publication 19.05.2022
Статья поступила в редакцию 28.02.2022, доработана 17.05.2022, подписана в печать 19.05.2022



Investigation of Pobeda furnace bubbling zone physics using cold modeling method

Part 3. The hydro-gas dynamics of combined blowing of liquid by gas using bottom and lateral lances

K.V. Bulatov¹, V.P. Zhukov¹, E.V. Bratygin¹, N.A. Tomilov¹, V.A. Menshchikov²

¹ JSC “Ural Research and Design Institute of Mining Processing, Metallurgy, Chemistry, Standartization”

87 Khokhryakova str., Ekaterinburg, 620063, Russia

² Ural Federal University n.a. the First President of Russia B.N. Eltsin

17 Mira str., Ekaterinburg, 620002, Russia

✉ Vladimir P. Zhukov (zhukov.v.p@mail.ru)

Abstract: Hydro-gas regularities of liquid combined blowing by gas were studied using cold modeling method at Archimedes criterion for lateral $Ar_l = 12+120$ and bottom blowing $Ar_b = 5+60$ simulating Pobeda bubbling unit. The blowing was performed simultaneously by bottom lance vertically fixed in centre of reactor and by the lateral lance which was attached at an angle 5° to the horizontal axis. The quantitative estimation of instantaneous and average circulation velocities (V_{av}) of liquid flow elements in different bath areas, depending on the location of blowing zone and Archimedes criterion, was performed. The liquid motion trajectory was determined. A vortex zone was revealed near the liquid surface and the reactor shell, where instantaneous velocity of the liquid flow elements changes from 69.9 to 181.1 mm/s and $V_{av} = 123.8$ mm/s. The circulation flows fade in the bulk of liquid and V_{av} decreases from 123.8 to 47.0 and 54.1 mm/s. It was shown that, in general, circulation velocity depends on the blowing intensity and appears to be higher for the zone of overlapping of lateral and bottom streams. The dynamic blowing conditions, which ensure the direct contact of lateral and bottom jets leading to their interflow and increased spatter formation, were identified. The characteristics of 3 types of surface oscillations for interface phases “pure liquid – gas-liquid layer”, as well as the estimation of the lateral and bottom blowing impact on the type of oscillation were provided. It has been noted that the introduction of the bottom blowing ($Ar_b = 5$) causes the wave-like motion of liquid (the 2nd type) along with the transverse oscillations of the 1st type, and at higher values of $Ar_b = 25$ the angular oscillations of the 3rd type develop. It has been shown that the presence of a lateral jet at the combined blowing decreases angles of bath swinging to $8-12^\circ$ to horizontal axis. For the estimation of oscillation intensity, $\Delta h_l = (h_l)_{max} - (h_l)_{min}$ value, which means the difference between maximum $(h_l)_{max}$ and minimum $(h_l)_{min}$ height of liquid for the full-wave oscillations (τ), was introduced. The height of liquid (h_l) was plotted as a function of τ , Ar_l , Ar_b , Δh_l was determined on the basis of obtained graph values, which varied upon modeling over the range of 7.7–69.5 mm. The relation between the liquid circulation velocity and the oscillation value (Δh_l) was established for different bath zones and dynamic conditions of the blowing. The impact of all oscillations types on potential erosive lining wear of Pobeda bubbling unit and the completeness of adoption of charging material nearby the bath surface was investigated.

Keywords: combined blowing, lateral lance, bottom lance, Archimedes criterion, Pobeda melting unit, liquid circulation, instantaneous circulation velocity, average circulation velocity, blowing zone, coordinate, interphase oscillation

For citation: Bulatov K.V., Zhukov V.P., Bratygin E.V., Tomilov N.A., Menshchikov V.A. Investigation of Pobeda furnace bubbling zone physics using cold modeling method. Part 3. The hydro-gas dynamics of combined blowing of liquid by gas using bottom and lateral lances. *Izvestiya. Non-Ferrous Metallurgy*. 2023; 29 (1): 26–38. (In Russ.). <https://doi.org/10.17073/0021-3438-2023-1-26-38>

Исследование физических явлений в барботажной зоне плавильного агрегата «Победа» методом холодного моделирования

Сообщение 3. Гидрогазодинамика комбинированной продувки жидкости газом с помощью донной и боковой фурм

К.В. Булатов¹, В.П. Жуков¹, Е.В. Братыгин¹, Н.А. Томилов¹, В.А. Меньшиков²

¹ ОАО «Уральский научно-исследовательский и проектный институт горного дела, обогащения, металлургии, химии, стандартизации» (ОАО «Уралмеханобр») 620063, Россия, г. Екатеринбург, ул. Хохрякова, 87

² Уральский федеральный университет им. первого Президента России Б.Н. Ельцина 620002, Россия, г. Екатеринбург, ул. Мира, 17

✉ Владимир Петрович Жуков (zhukov.v.p@mail.ru)

Аннотация: Методом холодного моделирования в интервалах величин критерия Архимеда для бокового ($Ar_б = 12\div 120$) и донного ($Ar_д = 5\div 60$) дутья применительно к условиям работы барботажного плавильного агрегата «Победа» (ПАП) исследованы гидрогазодинамические закономерности комбинированной продувки жидкости газом. Продувку осуществляли одновременно донной фурмой, установленной вертикально по центру реактора, и боковой, расположенной под углом 5° к горизонтальной оси. Проведена количественная оценка мгновенной и средней ($V_{ср}$) скоростей циркуляции элементов потока жидкости на разных участках ванны в зависимости от местонахождения зоны продувки и критериев Архимеда. Определена траектория движения жидкости. Вблизи поверхности жидкости и корпуса реактора обнаружена вихревая зона, где мгновенная скорость движения элемента потока жидкости изменяется от 69,9 до 183,1 мм/с и $V_{ср} = 123,8$ мм/с. В объеме жидкости циркуляционные потоки затухают, и $V_{ср}$ уменьшается от 123,8 до 47,0 и 54,1 мм/с. Показано, что в общем случае скорость циркуляции зависит от интенсивности продувки на фурмах и становится выше для области наложения боковой и донной струй. Определены динамические условия продувки, обеспечивающие непосредственный контакт бокового и донного факелов, приводящий к слиянию потоков и повышенному брызгообразованию. Приведена характеристика 3 видов колебаний поверхности раздела фаз «чистая жидкость – газожидкостный слой» и дана оценка влияния бокового и донного дутья на разновидность возникающих колебаний. Отмечено, что ввод донного дутья ($Ar_д = 5$) приводит, наряду с поперечными колебаниями 1-го типа, к появлению волнообразного движения жидкости (2-й тип), а при более высоких значениях $Ar_д = 25$ – к угловым колебаниям (3-й тип). Показано, что при комбинированной продувке наличие бокового факела уменьшает углы раскачивания ванны к горизонту до $8\text{--}12^\circ$. Для оценки интенсивности колебаний введена величина $\Delta h_ж = (h_ж)_{\max} - (h_ж)_{\min}$, т.е. разность между максимальной $(h_ж)_{\max}$ и минимальной $(h_ж)_{\min}$ высотой жидкости за полный цикл колебаний (τ). Построены зависимости высоты жидкости $(h_ж)$ от τ , $Ar_б$ и $Ar_д$, на основании которых определены величины $\Delta h_ж$, варьируемые при моделировании в интервале 7,7–69,5 мм. Для различных областей ванны и динамических условий продувки установлен взаимосвязь между скоростью циркуляции жидкости и величиной колебаний ($\Delta h_ж$). Рассмотрено влияние всех видов колебаний на возможный эрозивный износ футеровки ПАП и полноту усвоения шихтовых материалов вблизи поверхности ванны.

Ключевые слова: комбинированная продувка, боковая фурма, донная фурма, критерий Архимеда, плавильный агрегат «Победа», циркуляция жидкости, мгновенная скорость циркуляции, средняя скорость циркуляции, область продувки, координаты, колебания границы раздела фаз

Для цитирования: Булатов К.В., Жуков В.П., Братыгин Е.В., Томилов Н.А., Меньшиков В.А. Исследование физических явлений в барботажной зоне плавильного агрегата «Победа» методом холодного моделирования. Сообщение 3. Гидрогазодинамика комбинированной продувки жидкости газом с помощью донной и боковой фурм. *Известия вузов. Цветная металлургия*. 2023; 29 (1): 26–38. (In Russ.). <https://doi.org/10.17073/0021-3438-2023-1-26-38>

Introduction

Previously, the hydrodynamic patterns of separate (lateral and bottom) liquid blowing using a single lance in a gas envelope were studied [1–3]. This paper is aimed at estimating the physics upon the

combined outflow of gas into the liquid through the lateral and bottom nozzles. Due to being split, the combined blowing allows to integrally impact the melt with several jets and to influence the physico-

chemical regularities of metallurgical reactions, respectively.

Currently, the majority of publications are devoted to autogenous processes, addressing the operation of units with a submersible vertical lance, as well as various combinations of bottom or lateral blowing with top blowing in relation to steelmaking technology [4–21]. At the same time, each combination of blowing devices is characterized by optimal geometric and gas-dynamic parameters. In addition, it is known that the melting productivity of copper sulfide concentrate in Pobeda melting unit (PMU) depends on the ratio of bottom and lateral blowing costs [5]. The geometry of the mutual arrangement of the lances and the direction of the streams in the melt have different effects on the intensity of the bath mixing. The mathematical description of hydro-gas-dynamics as applied to bubbling conditions and the solution of a complete system of differential equations for calculating the true velocity of currents in two and three directions are of significant difficulty. Therefore, the melt circulation velocity was determined experimentally using the cold modeling method.

Experimental methods

The experiments were carried out using lateral and bottom lances installed in the reactor of the laboratory plant as used in previous papers [1–3]. The location of

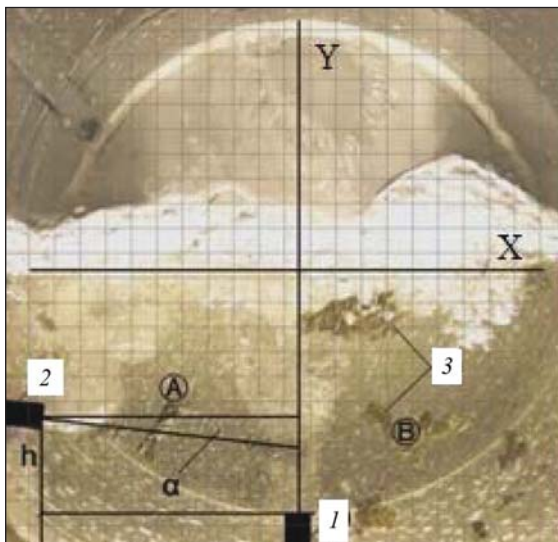


Fig. 1. The position of lance in relation to the axes of the cross-section of the reactor with a conditional coordinate grid

Рис. 1. Положение фурм относительно осей поперечного сечения реактора с условной координатной сеткой

the lances in relation to the axes of the nozzles and the reactor is shown in Fig. 1. The bottom lance 1 was vertically fixed in the center of the reactor, and the lateral lance 2 was attached at an angle of $\alpha = 5^\circ$ to the horizontal axis. The lances were placed in the same plane of the cross section of the plant at a distance of $h = 42$ mm between the centers of the tips of the lateral and bottom lances. During the modeling, the change in the coordinates of the location of individual particles-indicators 3 in current blowing time τ_i was monitored, the streamlines were drawn, and the liquid circulation velocity was calculated.

The object of research was the hydrodynamics between the lateral and bottom streams in the conditional area A and beyond the bottom stream in area B . During the data processing, the film fragments allowing to visualize the sequential movement of a specific indicator within the field of the investigated areas of the bath were used. The total distance (S) of the curved path of the indicator was assumed to be the sum of the absolute values of the lengths of the segments (S_i) by which its center moves at each i th point of n images:

$$S = \sum_{i=1}^n |S_i|. \quad (1)$$

In the Cartesian coordinate system, the distance between points is as follows:

$$S_i = \sqrt{(x_{i+1} - x_i)^2 + (y_{i+1} - y_i)^2}, \quad (2)$$

where i stands for the number of the image in the series; x_i, y_i are the indicator coordinates in the i th image; x_{i+1}, y_{i+1} are the coordinates in the next image within the following time: $\Delta\tau = \tau_{i+1} - \tau_i$.

Instantaneous (V_i) and average (V_{av}) values of indicator movement velocity were calculated by the following equations:

$$V_i = S_i / \Delta\tau, \quad (3)$$

$$V_{av} = S / (n\Delta\tau), \quad (4)$$

where $\Delta\tau$ stands for the time interval between the shots, which is equal to 0.143 s according to the conditions of the experiment.

The example shown in Fig. 2 illustrates the methodology for determining the trajectory and calculating the values of V_i, V_{av} for the movement of the indicator mark in the liquid between the lateral and bottom streams when analyzing 6 fragments of the film record depicted in Fig. 3. In the coordinate system (Fig. 2), the horizontal axis X is directed along the bottom nozzle section, while the vertical axis Y passes through its

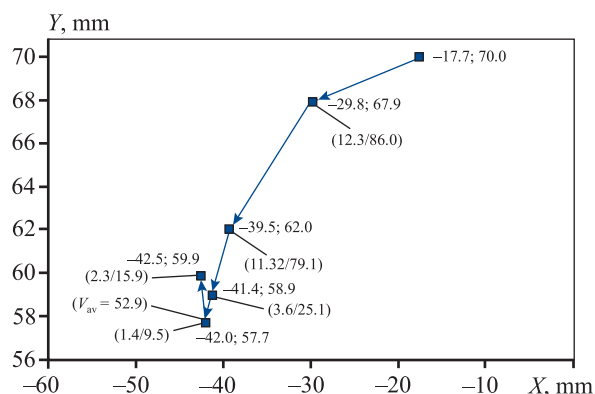


Fig. 2. The current coordinates and the trajectory of the indicator movement in $\Delta\tau = 0.143$ s

In brackets the numerator is the length of the segment (S_i , mm), the denominator is the instantaneous velocity (V_i , mm/s)

Рис. 2. Текущие координаты и траектория перемещения индикатора через $\Delta\tau = 0,143$ с

В скобках числитель – длина отрезка (S_i , мм), знаменатель – мгновенная скорость (V_i , мм/с)

center. A two-dimensional section of the bath with a symmetry plane in the middle of the section is considered, assuming that the mixing conditions in other sections do not affect this velocity field. The current location of the particles was also determined using Paint.net software [1]. When comparing the coordinates in the image measurement system with real coordinates, the position of the axes and the scale of the image were taken into account.

The motion of liquid in the blowing area occurs due to the translational energy of the gas stream, which is determined by the magnitude of its momentum. When using a shell lance, the total momentum of motion (i_t) translated to the liquid by annular (i_{sh}) and circular (i_c) streams is equal to the sum of these values as per the principle of conservation of moment [6]:

$$i_t = i_{sh} + i_c. \tag{5}$$

According to the experimental conditions [1], the cross-sectional areas of the annular (f_{sh}) and circular

(f_c) nozzles are equal, therefore, the equivalent size of the annular nozzle is as follows: $d_e = (4f_{sh}/\pi)^{1/2}$, and $d_e = d_{sh} = d_c$. As the momentum of the stream is generally determined by the following equation:

$$i = \rho_g \omega_g^2 f_n, \tag{6}$$

where ρ_g stands for gas density, kg/m^3 , ω_g stands for the velocity of gas outflow from the nozzle, m/s , and f_n stands for the cross-sectional area of the nozzle, m^2 , and the Archimedes criterion is determined under the following equation:

$$Ar = \frac{\rho_g \omega_g^2}{\rho_l g d_n}, \tag{7}$$

where d_n stands for the nozzle diameter, m , we obtain the following expression, taking into account expression (5):

$$Ar_t = Ar_{sh} + Ar_c, \tag{8}$$

where Ar_t stands for total Archimedes criterion; Ar_{sh} , Ar_c stand for its values of gas outflow from the shell and the central nozzle, respectively.

The additive nature of equations (5), (8) indicates the possibility of modeling of physics in the investigated areas of the bath using only one cylindrical nozzle for blowing with gas supply at a value of Ar_t equivalent to the values of Ar_{sh} , Ar_c .

The liquid was treated by the lateral and bottom streams at a blowing flow rate through a circular nozzle corresponding to $Ar_l = 12+120$ and $Ar_b = 5+60$ Archimedes criteria for the lateral and bottom gas injection. The latter are in the range of Ar_t values of equation (8) and correspond to the dynamic conditions of the previously performed cold molding with separate gas supply to the annulus and the central cavity of the lance [1–3].

Modeling results and discussion

Fig. 4 represents a diagram of motion of the liquid in the laboratory reactor with an inner radius $R = 135$ mm,

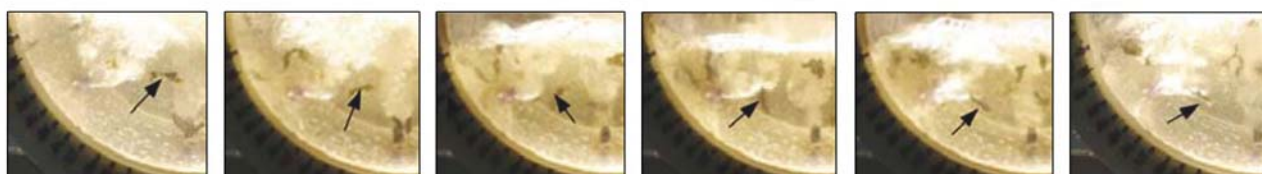


Fig. 3. The film record of the indicator successive movement (marked by the arrow) in the bubbling area (A) with the interval of $\Delta\tau = 0.143$ s

Рис. 3. Кинограмма последовательного движения индикатора (указан стрелкой) в области барботаж (A) с шагом $\Delta\tau = 0,143$ с

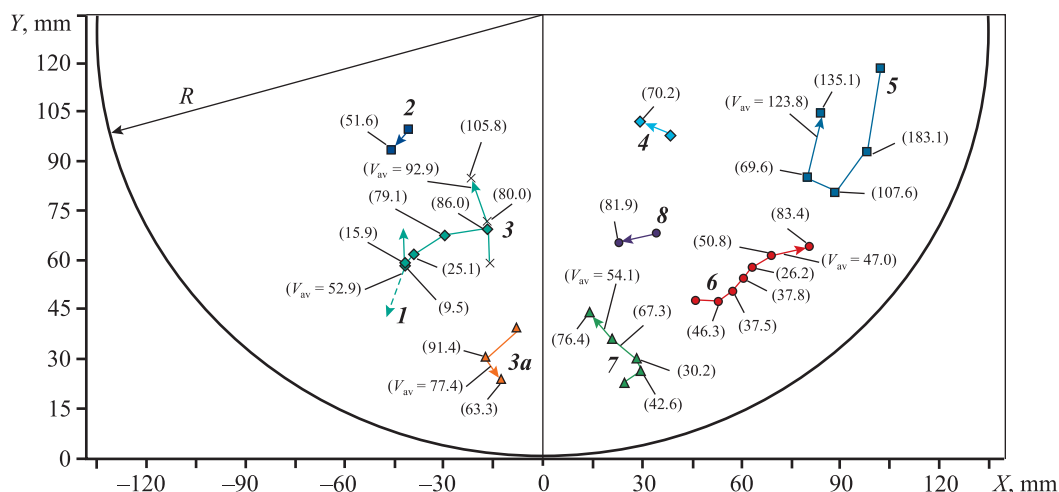


Fig. 4. The scheme of liquid motion and velocity field depending on the blowing conditions and the coordinates of the bubbling area

For combined lateral and bottom blowing – curves *1, 4, 6–8* ($Ar_l = Ar_b = 25$) and *3* ($Ar_l = 25, Ar_b = 5$); *3a* – separate lateral blowing ($Ar_l = 25$); *2, 5* – only bottom blowing ($Ar_b = 25$)

Рис. 4. Схема движения жидкости и поле скоростей в зависимости от условий продувки и координат области барботаж

Для совместного бокового и донного дутья – кривые *1, 4, 6–8* ($Ar_b = Ar_d = 25$) и *3* ($Ar_b = 25, Ar_d = 5$); *3a* – отдельная боковая продувка ($Ar_b = 25$); *2, 5* – только донная продувка ($Ar_d = 25$)

and shows V_i , V_{av} values for each velocity vector at the corresponding coordinate point.

As it follows from the data in Fig. 4, the geometry of the streamlines and the value of the liquid circulation velocity depend on the blowing conditions and the coordinates of the flow points in the bath. A vortex zone 22.0 mm wide and 37.9 mm high, being limited by the extreme values of x (79.9–101.9 mm) and y (80.6–118.5 mm) and remote from the inner surface of the reactor shell at a distance of 27 mm (curve 5) is formed near the liquid surface and the shell. At this point, the instantaneous velocity of the liquid flow element varies from 69.9 to 183.1 mm/s with an average velocity of 123.8 mm/s. The circulation flows fade in the bulk of liquid, resulting in V_{av} decreasing from 123.8 (curve 5) to 47.0 and 54.1 mm/s (curves 6 and 7, respectively). The difference in velocities can be explained by the wave nature of the oscillations of the gas-liquid system on the surface due to the factors of hydrodynamic instability of the bulk of liquid due to the pulsating mode of gas outflow [1, 2]. Approaching the reaction zone to the blowing jet results in increasing V_i values from 70.2 to 81.9 mm/s (curves 4, 8) and, on the contrary, decreasing them from 76.4 to 30.2 as well as from 46.3 to 26.2 mm/s (curves 7 and 6). A further increase in velocity to 42.6 and 83.4 mm/s occurs due to the displacement of the flow towards the surface of the reac-

tor shell, which also constitutes the reason for motion trajectory changes (curves 5–7).

Blowing area *A*, where the lateral and bottom jets produce a combined impact on the liquid, is of particular interest. The comparison of V_i values for comparable coordinates in *A* and *B* areas reveals a higher circulation velocity under the combined impact of the jets on the liquid, for instance, 86.0 mm/s (curve 1) and 81.9 mm/s (curve 8). Curve 1 is shown more precisely in Fig. 2, from which it can be seen that upon approaching the zone of impact of the lateral stream, the direction of the flow changes at the point with (–42.0; 55.7 mm) coordinates (the dashed line indicates a hypothetically possible continuation of the motion trajectory), the instantaneous velocity increases from 9.5 to 15.9 mm/s (see Fig. 4). Note that even at a lower blowing intensity (curve 3), V_i and V_{av} values are 105.8 and 92.9 mm/s, which is significantly higher than similar values in most areas of the considered velocity field. In the liquid circulation zone created only by the lateral jet (curve 3a), value $V_{av} = 77.4$ mm/s appears to be higher than the corresponding value of 54.1 mm/s (curve 7) in the bottom stream area. Upon that, the instantaneous velocity developed by the liquid at the same distance from the reactor shell is 91.4 mm/s at the lateral blowing and it is 30.2 mm/s near the bottom jet. This can be explained by additional swirling of the liquid flow in the near-wall

area due to the introduction of the blowing at an angle of swinging to horizontal axis (Fig. 1).

The scheme of liquid flows at higher values of Archimedes criterion is shown in Fig. 5, from which it follows that the previously revealed regularities of liquid motion are generally retained. Upon that, the circulation velocity in the considered areas of the bath (*A*, *B*) increases, for instance, according to the data shown in Fig. 4, V_{av} value is 52.9 and 92.9 mm/s in area *A*, 47.0 and 54.1 mm/s in area *B*, whereas at high *Ar* values (Fig. 5) V_{av} increases up to 121.3 and 112.0 mm/s, respectively. Upon comparing the trajectories of motion of liquid elements (curves 2 and 3 in Fig. 5), it can be seen that at

comparable coordinates of points (–43.3; 72.3 and 42.2; 78.5) V_i value is higher for the area of the combined impact of the streams (153.4 mm/s) than in the vicinity of the bottom jet (90.9 mm/s).

The intensity of circulation motions in the liquid is related to the energy impact of the streams on the corresponding areas of the liquid and is determined by Archimedes dynamic criterion at the nozzle outlet [12]. Therefore, the circulation velocity increases upon an increase in *Ar* value, which is particularly noticeable in the overlapping area of lateral and bottom streams (area *A*). The geometric dimensions of this zone depend on the range of the lateral jet and the width of the bottom

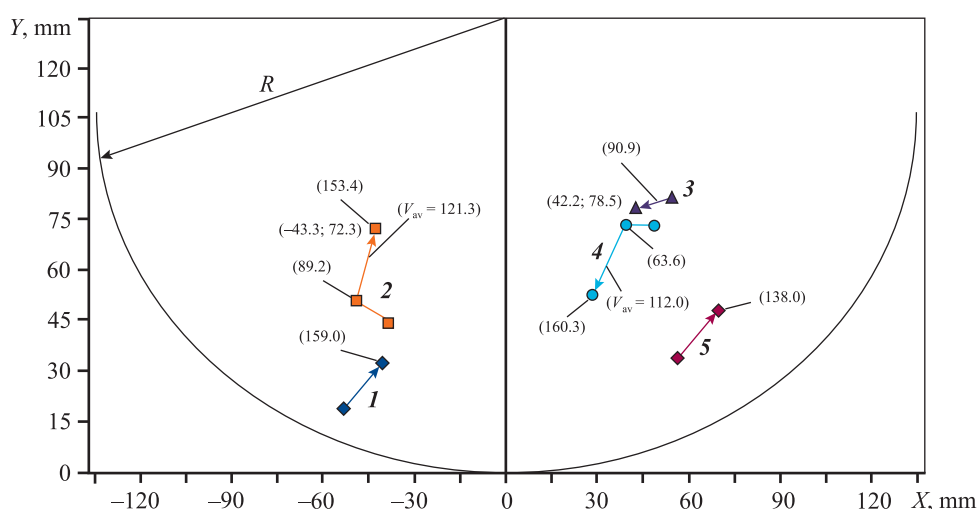


Fig. 5. Streamlines and the field of liquid motion velocities depending on *Ar* criterion

1, 4, 5 – $Ar_l = Ar_b = 60$; 2, 3 – $Ar_l = 120$; $Ar_b = 60$

Рис. 5. Линии тока и поле скоростей движения жидкости в зависимости от критерия *Ar*

1, 4, 5 – $Ar_b = Ar_d = 60$; 2, 3 – $Ar_b = 120$; $Ar_d = 60$

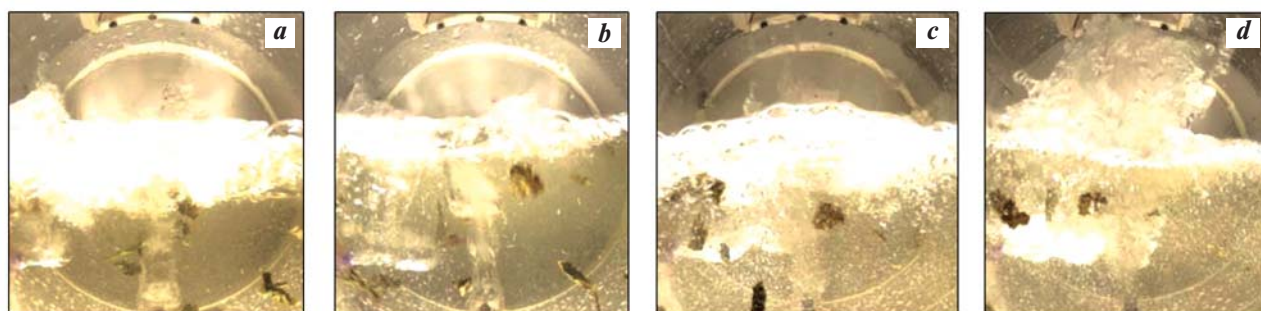


Fig. 6. The film fragments of the reaction zone depending on the size of the jet and Archimedes criterion upon reaching the extreme limits of the lateral stream range

a, b – $Ar_l = Ar_b = 60$; c, d – $Ar_l = 120$; $Ar_b = 60$

a, c – minimum lateral stream range; b, d – the maximum one

Рис. 6. Кинофрагменты реакционной зоны в зависимости от размеров факела и критерия Архимеда при достижении экстремальных границ дальности боковой струи

a, b – $Ar_b = Ar_d = 60$; c, d – $Ar_b = 120$; $Ar_d = 60$

a, c – минимальная дальность боковой струи; b, d – максимальная

jet, which are constantly changing due to the pulsation of the streams.

Fig. 6 shows the fragments of the reaction zone between the lateral and bottom jets at the moment of reaching the minimum (*a*, *c*) and the maximum (*b*, *d*) range of the lateral stream. It can be seen from the image in Fig. 6 (*d*) that with the relative constancy of the geometrical dimensions of the bottom stream due to $Ar_b = \text{const}$, the lateral jet under the conditions of $Ar_l = 120$ is in contact with the bottom stream. Upon less intensive blowing, a liquid area, being free from the interaction of streams, is observed (Fig. 6, *b*) between the lateral and bottom streams. The comparison of film fragments (Fig. 6, *b* and *d*) also exhibits that the direct contact of the blowing jets and the merging of their gas volumes are simultaneously accompanied by increased spatter formation. Furthermore, a high value of the Ar_b criterion and, accordingly, the length of the bottom stream can cause the formation of a “breakdown” of the bath [2], which results in a decrease in the degree of blowing oxygen uptake and an increase in the removal of the melt with spatter. According to the blowing macropattern (Fig. 6, *d*), such a mode is possible at $Ar_b = 60$, $Ar_l = 120$, therefore, it is of interest to estimate the velocity of circulation flows for variable values of Ar_b and Ar_l .

The table presents the data on liquid motion velocities in different parts of the bath, linked to the coordinate system (Fig. 4, 5), depending on the values of Ar_b , Ar_l upon $Ar_b \neq Ar_l$.

As a result of the analysis of the data specified in the table, the closest coordinates of the points were identified and the corresponding values Ar_b , Ar_l , V_i , V_{av} were determined. Data classification was performed using “*k* means” algorithm [22] and “Scikit-learn” standard cluster library [23]. The lines that characterize the trajectory of the movement of a particular indicator are marked with a horizontal line in the table. This allows to estimate the average circulation velocity along the entire length of the streamline *S*. The minimum discrepancy between the coordinates of the points was found in lines 1, 21; 11, 24; 13, 26; 16, 28; 4, 24; 8, 26, where the velocity value is least dependent on the location of the flow and is determined by other factors. The comparison of the table data (lines 11, 24; 13, 26; 16, 28) reveals that an increase in the bottom blowing intensity at $Ar_l = \text{const}$ reduces the liquid circulation velocity. An increase in Ar_l at $Ar_b = \text{const}$ causes an increase in the instantaneous and average velocities (lines 1, 21). The explanation of the specified regularities is as follows: In the general case, the mixing of the bath is performed due to the force impact of circulation

Liquid circulation velocity upon blowing through the lateral and bottom nozzles depending on the location of the flow and Archimedes criteria

Скорость циркуляции жидкости при продувке через боковое и донное сопла в зависимости от местоположения потока и критериев Архимеда

Archimedes criterion		Coordinates, mm		Velocity, mm/s		Line
Ar_b	Ar_l	<i>X</i>	<i>Y</i>	V_i	V_{av}	
1	2	3	4	5	6	7
5	25	-16.5	71.2	80.0	—	1
		-21.8	85.4	105.8	92.9	2
		-29.5	64.4	135.7	—	3
		-25.4	53.8	79.6	—	4
		-25.1	25.8	195.6	137.0	5
		12.4	90.3	58.9	—	6
		15.2	83.9	48.3	—	7
		18.8	64.3	139.1	—	8
		17.4	34.2	210.2	114.1	9
25	60	-37.8	43.5	82.0	—	10
		-30.9	37.0	66.1	—	11
		-22.1	37.0	63.0	70.4	12
		26.2	34.4	101.2	—	13
		38.6	42.1	102.1	—	14
		45.0	46.5	55.1	86.1	15
		101.0	102.8	50.6	—	16
		93.8	80.6	163.0	—	17
		95.5	70.0	76.7	—	18
107.9	78.2	104.2	98.6	19		
5	60	-21.3	61.1	88.1	—	20
		-14.4	54.9	64.8	76.4	21
		-59.9	35.9	4.31	—	22
		-45.5	29.0	111.2	—	23
		-28.7	29.5	117.6	77.7	24
		29.3	59.8	60.3	—	25
		18.8	34.8	189.1	—	26
		29.5	31.7	78.1	109.2	27
		102.4	95.6	143.2	—	28
		88.0	99.6	104.0	—	29
96.3	121.0	160.1	135.8	30		

flows and turbulent pulsations on the liquid [6]. Thus, the observed liquid velocity (V_i , V_{av}) represents the sum of the circulation (V_c) and pulsation (V_p) components of the velocity. Therefore, the different impact of the lateral and bottom blowing can be caused by the occurrence of turbulent pulsations in the gas-liquid two-

phase flow, the appearance of which causes oscillations of the bath.

The visualization results (Fig. 7, 8) attest to the fact that depending on Ar_b , Ar_l and the current blowing time, 3 main types of oscillations of the phase interface, i.e. gas-liquid and liquid layers of the bath, arise. The first one includes the vertical displacement of the horizontal plane of the main bulk of liquid by Δh_1 value (Fig. 7 *a, b*). The oscillations of the 2nd type form a wave-like motion of the liquid near the surface of the bath (Fig. 7, *c*). In this case, Δh_1 is defined as the difference between the average horizontal lines between the levels of the main bulks of pure liquid. The oscillations of the 3rd type (Fig. 8, *a–c*) are characterized

by opposite angles of swinging of the phase interface to the horizontal axis (for instance, 5°, 8°). This type of oscillation causes boundary vertical displacements of the liquid of various sizes Δh_1 on the inner surface of the reactor. All these 3 types of oscillation can be seen on a single film record.

To estimate the impact of each type of blowing on the overall macropattern of oscillations, the state of the liquid bath was considered under similar dynamic conditions of separate blowing for the lateral and bottom streams. Fig. 9 (*c*) shows the fragments of film record of liquid bubbling by single nozzles. As per Fig. 9 (*a*), it can be seen that wave-like oscillations of the 2nd type, being close to the sinus one with amplitude A , is

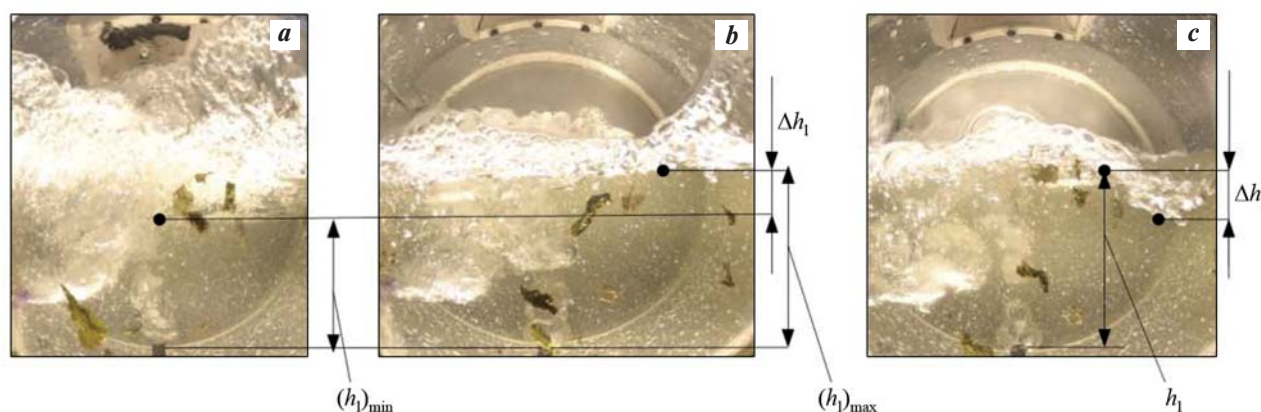


Fig. 7. Film fragments of transverse (*a, b*) and wave-like (*c*) oscillations of the liquid at $Ar_l = 60$, $Ar_b = 5$

Δh_1 – average change in the liquid level

Рис. 7. Кинофрагменты видов поперечного (*a, b*) и волнообразного (*c*) колебаний жидкости при $Ar_б = 60$, $Ar_д = 5$

$\Delta h_ж$ – среднее изменение уровня жидкости

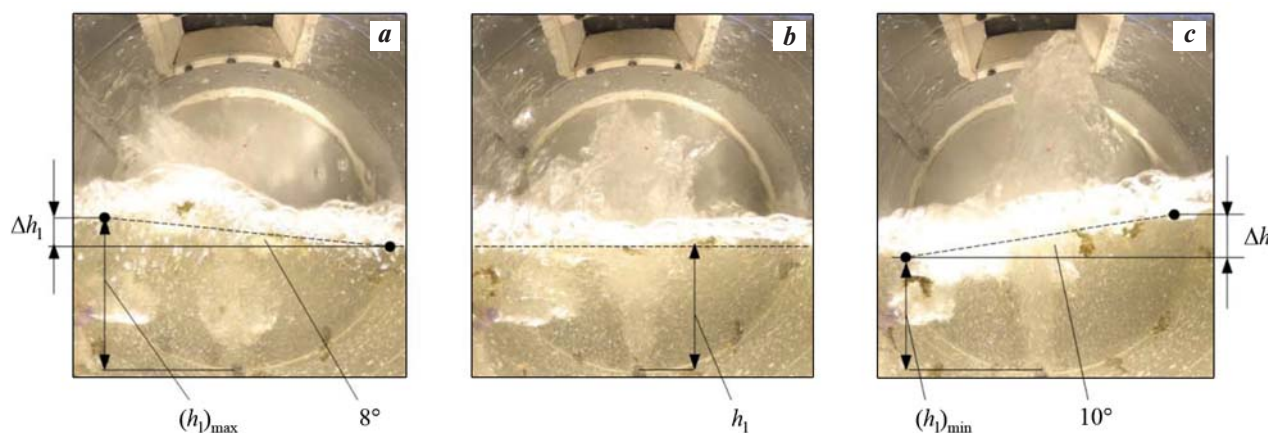


Fig. 8. The film fragments of successive changes in the averaged line of the interface between the gas-liquid and liquid layers of the bath depending on the current blowing time (τ_j) at $Ar_l = 60$, $Ar_b = 25$

τ_j , s: *a* – 0.143; *b* – 0.286; *c* – 0.429

Рис. 8. Кинофрагменты последовательного изменения усредненной линии границы раздела газожидкостного и жидкого слоев ванны в зависимости от текущего времени продувки (τ_j) при $Ar_б = 60$, $Ar_д = 25$

τ_j , с: *a* – 0,143; *b* – 0,286; *c* – 0,429

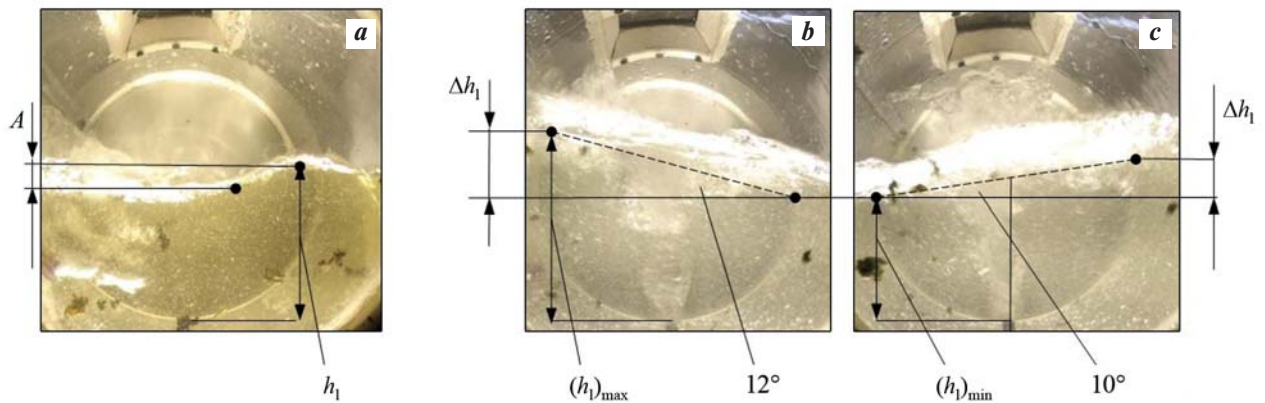


Fig. 9. The types of oscillations depending on the type of separate blowing at different values of Archimedes criterion *a* – the lateral blowing, $Ar_l = 60$; *b, c* – the bottom blowing, $Ar_b = 25$; the dashed line indicates the middle line of the phase boundary

Рис. 9. Разновидности колебаний в зависимости от вида отдельной продувки при различных значениях критерия Архимеда

a – боковая продувка, $Ar_b = 60$; *b, c* – донная, $Ar_d = 25$; штрихом показана средняя линия границы раздела фаз

more clearly revealed when the lateral blowing is used. Stronger bath oscillation with the angles of 12° and 10° under the 3rd type occurs in the case of bottom blowing (Fig. 9, *b, c*). Therefore, upon combined blowing, the partial contribution of each type of blowing impacts the overall intensity and the type of oscillations of the liquid bath in a different way. The moderate introduction of the bottom blowing ($Ar_b = 5$) causes the wave-like motion of the liquid (Fig. 7, *c*) along with the oscillations of the 1st type (see Fig. 7, *a, b*), and at higher values $Ar_b = 25$, it causes angular oscillations (Fig. 8). Upon that, Δh_l value gradually decreases as the bubbling area approaches the geometric center of the reactor. In practice, this circumstance means that the mixing of the bath according to the 3rd type covers the volume of the melt near the center of the PMU to a lesser extent, and is mainly concentrated on the periphery near the lining of the unit. This can cause additional erosive wear of the lining in the area of lances. The wavy oscillations of the 2nd type are characterized by less oscillation amplitude and Δh_l value, therefore, in the near-wall zone they can exhibit a lesser impact on the lining. The mixing of the melt in the surface layer due to any oscillations contributes to the dissolution and adoption of charging material by the liquid bath of the unit. A further increase of the blowing intensity only by a bottom lance increases the liquid swing angles up to 18 – 15° (Fig. 10). The combined blowing reduces the intensity and changes the pattern of angular oscillations of the liquid due to the lateral jet, reducing the angles of swinging from 18 – 15° down to 8 – 10° (Fig. 9, *a, b, c*; Fig. 10; Fig. 8, *a, c*). In industrial conditions, this type of oscillations can cause additional erosion of the PMU lining.

The impact of phase interface oscillations on the liquid circulation velocity at various points of the reaction zone and under various blowing conditions was studied. The value of oscillations was estimated as difference between maximum and minimum height of the liquid: $\Delta h_l = (h_l)_{\max} - (h_l)_{\min}$ for full-wave oscillations (τ_i). The place of control of extreme values of the height of pure liquid (h_l) at the current time τ_i was determined visually, based on the minimum gas injections. In the presence of oscillations of the 1st type, h_l was taken as the value corresponding to the horizontal line of the liquid (Fig. 7, *a, b*; Fig. 8, *b*), in the presence of oscillations of the 2nd type – at the wave amplitude point (Fig. 7, *c*; Fig. 9, *a*), and in the presence of oscillations of the 3rd type – near the reactor wall, at the point of extremum (Fig. 8, *a, c*; Fig. 9, *b, c*).

Fig. 11 presents the results of estimation of h_l values at the boundary with the gas-liquid layer depending on

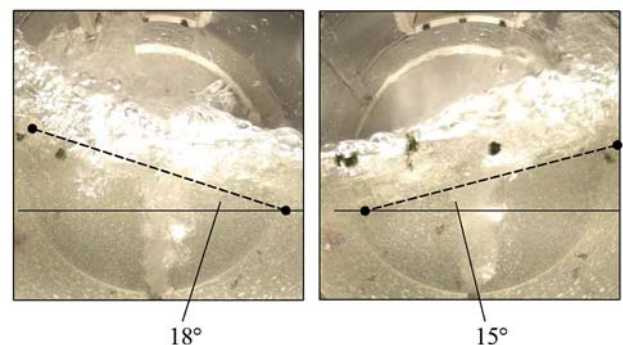


Fig. 10. The film fragments when the liquid is blown by the bottom lance at $Ar_b = 60$

Рис. 10. Фрагменты кинограммы при продувке жидкости донной фурмой при $Ar_d = 60$

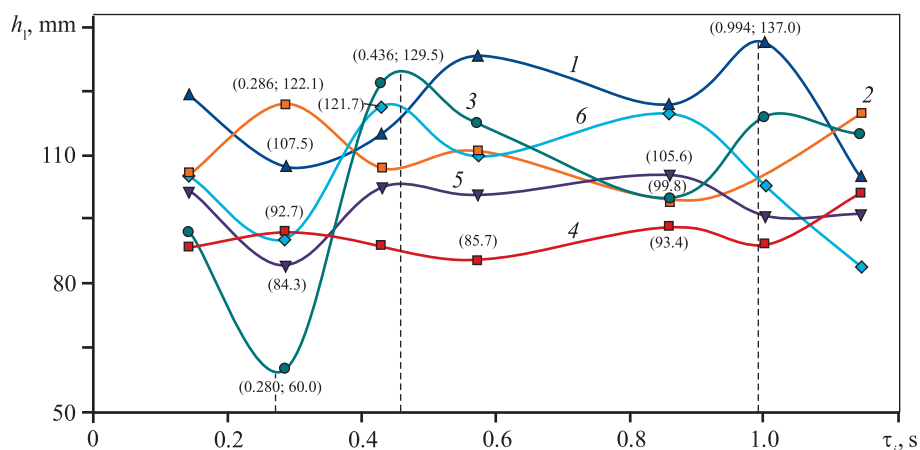


Fig. 11. The height of the liquid layer depending on the current time of the combined blowing and Archimedes criterion
 1 – $Ar_l = 60, Ar_b = 5$; 2 – $Ar_l = Ar_b = 25$; 3 – $Ar_l = 120, Ar_b = 60$; 4 – $Ar_l = 25, Ar_b = 5$; 5 – $Ar_l = 60, Ar_b = 25$; 6 – $Ar_l = Ar_b = 60$

Рис. 11. Высота слоя жидкости в зависимости от текущего времени комбинированной продувки и критерия Архимеда
 1 – $Ar_l = 60, Ar_b = 5$; 2 – $Ar_l = Ar_b = 25$; 3 – $Ar_l = 120, Ar_b = 60$; 4 – $Ar_l = 25, Ar_b = 5$; 5 – $Ar_l = 60, Ar_b = 25$; 6 – $Ar_l = Ar_b = 60$

the Archimedes criteria and the current blowing time τ_i . The coordinates of the extremum points of curves 1, 3 are determined based on the approximation functions. The type of curves in Fig. 11 demonstrates that the surface oscillations are complex in nature with different extreme values of h_l and the values of the time to reach them.

The results of mathematical processing of the data from Fig. 11 (curves 3, 4) attest to the fact that the change in the surface level of the liquid bath (Δh_l) makes up 7.7–69.5 mm and depends on Archimedes criteria of the lateral and bottom blowing. Increasing the overall intensity of the combined blowing at $Ar_l = Ar_b$ results in the increase of Δh_l from 21.3 to 29.0 mm (Fig. 11, curve 2, 6). For these conditions, as previously noted, the value of the average liquid circulation velocity increases. The change of Δh_l from 21.3 to 29.5 mm (Fig. 11, curves 5 and 1) for $Ar_b = 25$ and 5 increases V_i value from 66.1 to 117.6 mm/s (see the table, lines 11 and 24) and V_{av} value from 70.4 to 77.7 mm/s (see the table, lines 12 and 24) in area A. In area B, V_i value also increases from 50.6 to 143.2 mm/s (see the table, lines 16 and 28), and V_{av} increases from 98.6 to 135.8 mm/s (see the table, lines 19 and 30) under these conditions. The change of Ar_l from 25 to 60 ($Ar_b = 5 = \text{const}$) increases Δh_l value from 7.7 to 29.5 mm (Fig. 11, curves 4 and 1). Upon that, V_i for area A increases from 79.6 to 88.1 mm/s (see the table, lines 4 and 20). In the zone of interaction of the bottom stream only (B), V_{av} value also increases from 104.2 to 114.1 mm/s (see the table, lines 19 and 9). Thus, the liquid circulation velocity is interconnected with the pulsating component of the flow motion and increases

with an increase in the amplitude of oscillations at the phase boundary.

Conclusion

Over the range of $Ar_l = 12\div 120, Ar_b = 5\div 60$ values, cold modeling of the hydrodynamics of the bubbling PMU bath was performed with the combined blowing of the liquid by the lateral and bottom lances. A quantitative estimation of the velocity of liquid bath circulation, depending on the Archimedes criteria and the location of the flow, was performed. Three types of oscillations (pulsations) of the phase boundary “pure liquid – gas-liquid layer” were revealed. The analysis of the occurrence of each type of pulsation under various blowing conditions was performed. It is shown that the liquid circulation velocity depends on the intensity of oscillations, defined as the difference (Δh_l) between the maximum and minimum height of the pure liquid for full-wave oscillations. With regard to the stability of the PMU lining, the intensity of mixing of the near-surface layer and the adoption of charging material by the bath, the impact of each type of oscillations on the liquid circulation velocity was considered.

References

1. Bulatov K.V., Zhukov V.P., Bratygin E.V., Tomilov N.A., Menshikov V.A. Investigation of Pobeda furnace bubbling zone physics using cold modeling method. Part 1. Investigation of fluid and gas dynamics of bubbling using a side-blowing gas-protected lance. *Izvestiya. Non-Ferrous Metallurgy*. 2021; 27 (3): 15–23. (In Russ.).

- Булатов К.В., Жуков В.П., Братыгин Е.В., Томилов Н.А., Меньшиков В.А. Исследование физических явлений в барботажной зоне плавильного агрегата «Победа» методом холодного моделирования. Сообщение 1. Исследование гидрогазодинамических закономерностей продувки жидкости газом с помощью боковой фурмы в защитной газовой оболочке. *Известия вузов. Цветная металлургия*. 2021; 27 (3): 15–23.
2. Bulatov K.V., Zhukov V.P., Bratygin E.V., Tomilov N.A., Menshikov V.A. Investigation of Pobeda furnace bubbling zone physics using cold modelling method. Part 2. Hydro-gas dynamics of liquid blowing with gas using bottom gas-protected lance. *Izvestiya. Non-Ferrous Metallurgy*. 2022; 28 (1): 4–14. (In Russ.).
Булатов К.В., Жуков В.П., Братыгин Е.В., Томилов Н.А., Меньшиков В.А. Исследование физических явлений в барботажной зоне плавильного агрегата «Победа» методом холодного моделирования. Сообщение 2. Гидрогазодинамика продувки жидкости газом с помощью донной фурмы в защитной газовой оболочке. *Известия вузов. Цветная металлургия*. 2022; 28 (1): 4–14.
 3. Bulatov K.V., Zhukov V.P., Bratygin E.V., Tomilov N.A., Menshikov V.A. Investigation of Pobeda furnace bubbling zone physics using cold modelling method. Part 2. Hydro-gas dynamics of liquid blowing by gas using bottom gas-protected lance. *Russian Journal of Non-Ferrous Metals*. 2022; 63 (2): 113–120.
 4. Nakanishi K., Fujii T., Szekely J. Possible relationship between energy dissipation and agitation in steel-processing operations. *Ironmaking & Steelmaking*. 1975; 2 (3): 193–197.
 5. Bulatov K.V., Yakornov S.A., Ibragimov A.F., Iskhakov I.I. Industrial tests of sulphide copper concentrate melting in smelter Pobeda on oxygen blow using bottom tuyeres. *Metallurgist*. 2020; (8): 36–40. (In Russ.).
Булатов К.В., Якорнов С.А., Ибрагимов А.Ф., Исхаков И.И. Промышленные испытания плавки сульфидного концентрата в ПАП на кислородном дутье с использованием донных фурм. *Металлург*. 2020; (8): 36–40.
 6. Surin V.A., Nazarov Yu.N. Mass and heat transfer, hydro-gas dynamics of a metallurgical bath. Moscow: Metallurgiya, 1993. (In Russ.).
Сурин В.А., Назаров Ю.Н. Массо- и теплообмен, гидрогазодинамика металлургической ванны. М.: Металлургия, 1993.
 7. Dyudkin D.A., Kisilenko V.V. Modern steel production technology. Moscow: Teplotekhnika, 2007. (In Russ.).
Дюдкин Д.А., Кисиленко В.В. Современная технология производства стали. М.: Теплотехника, 2007.
 8. Fluid Flow, Duan Zhang, Lifeng Thomas, Brian Conejo. Dissolution, and mixing phenomena in argon-stirred steel ladles. *Metallurgical and Materials Transactions B*. 2018; 49: 2722–2743.
 9. Gajjar Prince, Haas T.N., Kwaku Boateng Owusu, Moritz Eickhoff, Pruet Kowitzarangkul, Herbert Pfeifer. Physical study of the impact of injector design on mixing, convection and turbulence in ladle metallurgy. *Engineering Science and Technology*. 2019; 22: 538–547.
 10. Rogotovskii A.N., Shipelnikov A.A., Bobyleva N.A., Rogotovskii A.N. Modeling of the melt movement in the tundish of a continuous casting machine with the presence of flow modifiers. *Lipetsk State Technical University*. 2018; 37 (3): 87–94. (In Russ.).
Роговский А.Н., Шипельников А.А., Бобылева Н.А., Роговский В.Н. Моделирование движения расплава в промежуточном ковше машины непрерывного литья заготовок с различными модификаторами потока. *Вестник Липецкого государственного технологического университета*. 2018; 37 (3): 87–94.
 11. Panteikov S.P. Technology of combined bottom blowing with oxygen and inactive gases in converters. *Ferrous Metallurgy. Bulletin of Scientific, Technical and Economic Information*. 2017; (7): 55–67. (In Russ.).
Пантейков С.П. Технология комбинированной продувки кислородом сверху и неактивными газами через днище в конвертерах. *Черная металлургия. Бюллетень научно-технической и экономической информации*. 2017; (7): 55–67.
 12. Chernatevich A.G., Molchanov L.S., Sigarev E.N., Dudchenko S.A., Vakul'chuk V.V., Yushkevich P.O., Chubin K.I., Pokhvalityi A.A., Chubina E.A. Video recording of physical and chemical processes in the converter cavity during the top blowing of the bath using various designs of oxygen lances. Part 1. Installations and methodology for conducting research. *Ferrous Metallurgy. Bulletin of Scientific, Technical and Economic Information*. 2021; 77 (8): 969–976. (In Russ.).
Чернатевич А.Г., Молчанов Л.С., Сигарев Е.Н., Дудченко С.А., Вакульчук В.В., Юшкевич П.О., Чубин К.И., Похвалитый А.А., Чубина Е.А. Видеофиксация физико-химических процессов в полости конвертера при верхней продувке ванны с использованием различных конструкций кислородных фурм. Сообщение 1. Установки и методика проведения исследований. *Черная металлургия. Бюллетень научно-технической и экономической информации*. 2021; 77 (8): 969–976.
 13. Chernyatevich A.G., Sigarev E.N., Molchanov L.S. A picture of blowing a converter bath using a two-tier oxygen

- lance. *Ferrous Metallurgy. Bulletin of Scientific, Technical and Economic Information*. 2017; (12): 39–45. (In Russ.).
Чернятевич А.Г., Сигарев Е.Н., Молчанов Л.С. Картина продувки конвертерной ванны с использованием двухъярусной кислородной фурмы. *Черная металлургия. Бюллетень научно-технической и экономической информации*. 2017; (12): 39–45.
14. Jiang X., Cui Z., Chen M., Zhao B. Mixing behaviors in the horizontal bath smelting furnaces. *Metallurgical and Materials Transactions B*. 2019; 50 (1): 173–180.
 15. Jiang X., Cui Z., Chen M., Zhao B. Study of plume eye in the copper bottom-blown smelting furnace. *Metallurgical and Materials Transactions B*. 2019; 50: 765–778.
<https://doi.org/10.1007/s11663-019-01516-0>
 16. Shijie Wang, William Davenport. Coppersmelting: world copper smelter data. *Copper*. 2016; 3: 29–31.
 17. Liam J., Joel P.T. The 2019 copper smelting survey. In: *Pyrometallurgy. Smelting operation: Proceedings Copper 2019 – Cobre International Conference* (Montreal, Quebec, Canada). 2019; 4 (1): 10.
 18. Matusевич R.W., Baldock B.R., Robert J.S. Ausmelt technology recycling of computer board and other high value materials. In: *European Metallurgical Conference EMC* (Friedrichshafen, Germany). 2001; 2: 151–163.
 19. Baldock B.R., Short W.E. Australian technology on the world scene. Update on Ausmelt plants and projects. In: *MINREX 2000: International Congress on mineral processing and extractive metallurgy* (Melbourne, Australia). 2000. P. 164–169.
 20. Yusupkhodjaev A.A., Matharimov S.T., Nosirhodjaev S.K. Wirkungen Technologien in der Kupferpyrometallurgien. Deutschland: Lambert Academic Publishing, 2019.
 21. Yusupkhodjaev A.A., Khojiev S.T., Berdyarov D.O. Technology of processing slags of copper production using local secondary technogenic formations. *International Journal of Innovative Technology and Exploring Engineering*. 2019; 9 (1): 5461–5472.
<https://doi.org/10.35940/ijitee.A4851119119.119119>
 22. MacQueen J. Some methods for classification and analysis of multivariate observations. In: *Proceedings 5th Berkeley Symposium on mathematical statistics and probability*. 1967; 281–297.
 23. Mueller A., Guido S. Introduction to machine learning with Python: A guide for data scientists. Sebastopol, USA: Publ. by O'Reilly Media, Inc., 2016.
Мюллер А., Гвидо С. Введение в машинное обучение с помощью Python: Рук-во для специалистов по работе с данными. М.: O'Reilly, 2017.

Information about the authors

Konstantin V. Bulatov – Cand. Sci. (Eng.), General Director of the JSC “Ural Research and Design Institute of Mining Processing, Metallurgy, Chemistry, Standartization” (JSC “Uralmekhanobr”).

<https://orcid.org/0000-0001-8474-598X>

E-mail: Bulatov_KV@umbr.ru

Vladimir P. Zhukov – Dr. Sci. (Eng.), Prof., Leading Researcher of the Laboratory of Sintering and Physical and Mechanical Tests (LSPMT), JSC “Uralmekhanobr”.

<https://orcid.org/0000-0002-3030-0077>

E-mail: zhukov.v.p@mail.ru

Evgenii V. Bratygin – Cand. Sci. (Eng.), Chief of Laboratory LSPMT, JSC “Uralmekhanobr”.

<https://orcid.org/0000-0003-4049-3797>

E-mail: bev@umbr.ru

Nikolay A. Tomilov – Engineer of Laboratory LSPMT, JSC “Uralmekhanobr”.

<https://orcid.org/0000-0002-2869-2892>

E-mail: tomilov.n@yahoo.com

Vikentii A. Menshchikov – Cand. Sci. (Eng.), Engineer of the Department of Non-Ferrous Metallurgy, Ural Federal University n.a. the First President B.N. Eltsin.

<https://orcid.org/0000-0002-5474-8829>

E-mail: kvadron@yandex.ru

Информация об авторах

Константин Валерьевич Булатов – к.т.н., генеральный директор ОАО «Уральский научно-исследовательский и проектный институт горного дела, обогащения, металлургии, химии, стандартизации» (ОАО «Уралмеханобр»).

<https://orcid.org/0000-0001-8474-598X>

E-mail: Bulatov_KV@umbr.ru

Владимир Петрович Жуков – д.т.н., профессор, ведущий научный сотрудник лаборатории окискования и физико-механических испытаний (ОиФМИ), ОАО «Уралмеханобр».

<https://orcid.org/0000-0002-3030-0077>

E-mail: zhukov.v.p@mail.ru

Евгений Владимирович Братыгин – к.т.н., заведующий лабораторией ОиФМИ, ОАО «Уралмеханобр».

<https://orcid.org/0000-0003-4049-3797>

E-mail: bev@umbr.ru

Николай Алексеевич Томилов – инженер лаборатории ОиФМИ, ОАО «Уралмеханобр».

<https://orcid.org/0000-0002-2869-2892>

E-mail: tomilov.n@yahoo.com

Викентий Алексеевич Меньшиков – к.т.н., инженер кафедры металлургии цветных металлов, Уральский федеральный университет им. первого Президента России Б.Н. Ельцина.

<https://orcid.org/0000-0002-5474-8829>

E-mail: kvadron@yandex.ru

Contribution of the authors

K.V. Bulatov – formation of the main concept, setting the goal and objectives of the study, preparation of the text, formulation of conclusions.

V.P. Zhukov – scientific guidance, analysis of research results, correction of the text of the article.

E.V. Bratygin – development of a methodology for processing experimental data, management of the experiment, resources supply.

N.A. Tomilov – processing of experimental data, performing calculations.

V.A. Menshchikov – the experimental technique substantiation, processing of research results.

Вклад авторов

К.В. Булатов – формирование основной концепции, постановка цели и задачи исследования, подготовка текста, формулировка выводов.

В.П. Жуков – научное руководство, анализ результатов исследований, корректировка текста статьи.

Е.В. Братыгин – разработка методологии обработки экспериментальных данных, руководство проведением эксперимента, обеспечение ресурсами.

Н.А. Томилин – обработка экспериментальных данных, выполнение расчетов.

В.А. Меньшиков – обоснование техники эксперимента, обработка результатов исследований.

The article was submitted 05.09.2022, accepted for publication 11.10.2022
Статья поступила в редакцию 05.09.2022, подписана в печать 11.10.2022

UDC 669.721.5

<https://doi.org/10.17073/0021-3438-2023-1-39-55>

Research article

Научная статья



Investigation of castability, mechanical, corrosion properties and flammability of ML-OPB and EWZ43 magnesium alloys

V.E. Bazhenov¹, I.I. Baranov¹, A.A. Lyskovich¹, A.V. Koltygin¹, A.V. Sannikov¹,
K.A. Kyaramyan², V.D. Belov¹, S.P. Pavlinich²

¹ National University of Science and Technology “MISIS”

4 Leninskii pr., Moscow, 119049, Russia,

² Branch of JSC “United Engine Corporation”

Research Institute of Technology and Organization of Engine Production

16, build. 182 Budennogo av., Moscow, 105118, Russia

✉ Vyacheslav E. Bazhenov (V.E.Bagenov@gmail.com)

Abstract: Magnesium alloys are usually considered as structural materials when the weight reduction is important - in aircraft and space industry for example. In recent years, there has been an increase in the use of new generation ignition-proof high-strength magnesium alloys in the design of aircraft parts. The properties of new ignition-proof casting magnesium alloys ML-OPB (Mg–6.7Y–2.6Zn–0.5Zr–0.35Ce–0.35Yb; wt.%) and EWZ43 (Mg–3.8Y–4.4Nd–0.6Zr–0.6Zn; wt.%) were investigated and compared with properties of commercial magnesium alloys. The microstructure of investigated alloys in the as-cast condition comprises of a magnesium solid solution and a significant amount of eutectic. Heat treatment according to the T6 mode results in change in the eutectic phase’s morphology and also to their partial dissolution in the magnesium matrix. Long-term high-temperature holding, simulating operating conditions (500 h at 300 °C), leads to the formation of precipitates along the grain boundaries in both alloys, significantly reducing the mechanical properties. During the oxidation of the samples, it was established that the main components that involved into the oxide film and provides the protective properties of the alloys is Y, Nd and Yb. The investigated alloys have a high strength, which is not lower than that of the ML10 alloy. At the same time, the advantage of the ML-OPB alloy is a high elongation at fracture, while the EWZ43 alloy is characterized by high strength. The corrosion rate of the investigated alloys exceeds the corrosion rate of known commercial ML10 and AZ91 alloys, which implies the need for additional protection against corrosion of investigated alloys. At the same time, the castability of ML-OPB and EWZ43 alloys is no lower than that of most commercial magnesium alloys. An oxide film with high Y content and high protective properties is formed when the alloys interact with the sand mold bonded with furan resin. The ignition temperature of the investigated alloys is 100–150 °C higher than that of the ML10 alloy. The flammability test of alloys in the flame of a gas burner, made on cone samples and typical aircraft castings «bracket», showed that ML-OPB and EWZ43 alloys are almost non-flammable under the conditions of experiment.

Keywords: magnesium alloys, ignition temperature, corrosion resistance, mechanical properties, castability, ignition-proof

Funding: The work was undertaken as part of research project between JSC UEC and NUST MISIS.

For citation: Bazhenov V.E., Baranov I.I., Lyskovich A.A., Koltygin A.V., Sannikov A.V., Kyaramyan K.A., Belov V.D., Pavlinich S.P. Investigation of castability, mechanical, corrosion properties and flammability of the ML-OPB and EWZ43 magnesium alloys. *Izvestiya. Non-Ferrous Metallurgy*. 2023; 29 (1): 39–55. (In Russ.). <https://doi.org/10.17073/0021-3438-2023-1-39-55>

Исследование литейных, механических, коррозионных свойств и пожароопасности магниевых сплавов МЛ-ОПБ и EWZ43

В.Е. Баженов¹, И.И. Баранов¹, А.А. Лыскович¹, А.В. Колтыгин¹, А.В. Санников¹,
К.А. Кярамян², В.Д. Белов¹, С.П. Павлинич²

¹ Национальный исследовательский технологический университет «МИСИС»
119049, Россия, г. Москва, Ленинский пр-т., 4

² Филиал АО «Объединенная двигателестроительная корпорация»
АО Научно-исследовательский институт технологии и организации производства двигателей
(АО «ОДК» «НИИД»)
105118, Россия, г. Москва, пр-т Буденного, 16, корп. 182

✉ Вячеслав Евгеньевич Баженов (V.E.Bagenov@gmail.com)

Аннотация: Магниевые сплавы как конструкционные материалы обычно рассматриваются в тех случаях, когда снижение массы имеет важнейшее значение, например в авиации и космонавтике. В последние годы наблюдается расширение применения пожаробезопасных высокопрочных магниевых сплавов нового поколения в конструкциях авиационных изделий. В работе были изучены свойства новых пожаробезопасных литейных магниевых сплавов МЛ-ОПБ (Mg–6,7Y–2,6Zn–0,5Zr–0,35Ce–0,35Yb) и EWZ43 (Mg–3,8Y–4,4Nd–0,6Zr–0,6Zn) и выполнено их сравнение с промышленными магниевыми сплавами. Микроструктура исследуемых сплавов в литом состоянии представляет собой магниевый твердый раствор и значительное количество эвтектики. Термическая обработка по режиму T6 приводит к изменению морфологии фаз в эвтектике, а также их частичному растворению в магниевой матрице. В результате длительной высокотемпературной выдержки, имитирующей условия эксплуатации (500 ч при 300 °С), происходит формирование выделений по границам зерен в обоих сплавах, которые значительно снижают механические свойства. Было установлено, что при окислении образцов основными компонентами, переходящими в оксидную плену и обеспечивающими защитные свойства сплавов, являются Y, Nd и Yb. Рассматриваемые сплавы обладают высокими прочностными свойствами, которые не ниже, чем у сплава МЛ10. При этом преимуществом сплава МЛ-ОПБ является высокое относительное удлинение, а для сплава EWZ43 характерна высокая прочность. Скорость коррозии этих сплавов выше, чем у известных промышленных сплавов МЛ10 и МЛ5, из чего следует, что исследуемые сплавы требуют дополнительной защиты от коррозии. При этом литейные свойства сплавов МЛ-ОПБ и EWZ43 оказались не ниже, чем у наиболее распространенных магниевых сплавов. При взаимодействии сплавов с формой из холодно-твердеющей смеси формируется оксидная пленка с высоким содержанием Y и хорошими защитными свойствами. Температура возгорания изученных сплавов оказалась на 100–150 °С выше, чем у сплава МЛ10. Испытание сплавов в пламени газовой горелки на конусных образцах и типовых авиационных отливках типа «кронштейн» показало, что сплавы МЛ-ОПБ и EWZ43 практически не горят в условиях эксперимента.

Ключевые слова: магниевые сплавы, температура возгорания, коррозионная стойкость, механические свойства, литейные свойства, пожаробезопасность

Финансирование: Работа выполнена в рамках НИР между АО «ОДК» и НИТУ МИСИС.

Для цитирования: Баженов В.Е., Баранов И.И., Лыскович А.А., Колтыгин А.В., Санников А.В., Кярамян К.А., Белов В.Д., Павлинич С.П. Исследование литейных, механических, коррозионных свойств и пожароопасности магниевых сплавов МЛ-ОПБ и EWZ43. *Известия вузов. Цветная металлургия*. 2023; 29 (1): 39–55. <https://doi.org/10.17073/0021-3438-2023-1-39-55>

Introduction

The creation of ignition-proof casting magnesium alloys represents a very urgent task, especially for the aircraft industry [1]. Currently, it is recognised as economically and technologically advantageous to expand the use of new generation of ignition-proof high-

strength magnesium alloys in the design of aircraft parts [2].

Ignition resistance is directly dependent on the ability of the oxide film on the surface of the magnesium alloys to protect the metal from contact with atmospheric

oxygen over a wide temperature range [3]. The protective properties of an oxide film can be evaluated by the Pilling—Bedworth ratio (P—B ratio), which indicates the ratio of the oxide volume to the metal volume. If it is greater than 1, the film forming on the surface of the alloy is dense and protects it well against further oxidation. For magnesium and its oxide, the value of P—B ratio is 0.81 [4], i.e., a dense film is not formed. However, with the addition of certain alloying elements the density of the oxide film on the surface of the alloys increases significantly. For example, for the yttrium/yttrium oxide pair, the P—B ratio is 1.39 [4], which means that if an oxide layer with a predominant composed of Y_2O_3 is present, it should be dense and protect the alloy well against oxidation and ignition. Yttrium can therefore be used as an alloying element for ignition-proof alloys. Other rare-earth metals (REs) also contribute to the formation of a protective oxide film. For example, the positive effect of yttrium [5] neodymium [6] lanthanum [7], cerium [8] is known. Calcium is another excellent choice as a component to enhance the protective properties of the oxide film. Numerous studies [9–11] indicate a significant increase in the ignition temperature in the alloys after the addition of calcium.

It is worth noting that the joint addition of several elements that increase the density of the oxide film provides the maximum protective effect. For instance, it was shown in works [5, 8] that the dense oxide film is formed on the surface of Mg—Y alloy when the Y content exceeds 10 wt.%. If a small amount of Ce is subsequently added to the Mg—Y alloy, however, a dense protective film can be formed even at 3 wt.% Y.

Known ignition resistant alloys of the Mg—RE—Zn—Zr system with additions of Sc and Cd, developed by VIAM (Moscow) [12]. The alloys exhibit good strength, high ignition temperatures and a density of less than 2 g/cm^3 . However, the addition of Cd poses environmental risks to the melting of this alloy, whereas Sc is a very expensive alloying element and is currently used industrially only as a microalloying element in aluminum alloys [13].

Earlier, the EWZ43 alloy of the Mg—Nd—Y—Zn—Zr system was developed at MISIS [14], which combines good mechanical properties with high castability [15]. Due to the high Y and Nd content, this alloy should exhibit a high resistance to ignition.

Togliatti State University (TSU) in cooperation with Solikamsk Experimental Metallurgical Plant (SOMZ) proposed the ML-OPB alloy, which is close to the $Mg_{97}Y_2Zn_1$ alloy in content of yttrium and zinc and additionally alloyed with small quantities of Ce and

Yb to increase the ignition temperature. $Mg_{97}Y_2Zn_1$ alloy belongs to alloys with the LPSO (long-period stacking-ordered) phase, usually used to obtain products by plastic deformation methods. Moreover, it is well studied [16–18]. At the same time in the as-cast condition the alloys of Mg—Y—Zn—Zr system can exhibit high mechanical properties (tensile yield strength (TYS) of 150–180 MPa), however, only in the presence of W phase ($MgYZn_2$ or $Mg_3Zn_3Y_2$) apart from the LPSO-phase in the alloy structure [19–21]. Thus, in this system the promising casting alloys with excellent castability and high resistance to ignition can be found.

The development of new ignition-proof alloys is quite an urgent task, however, designers need a thorough understanding of their properties in order to be able to offer such alloys. In this regard, the aim of this paper was to investigate the castability, mechanical properties, corrosion properties and flammability of EWZ43 and ML-OPB magnesium alloys and to compare them with the properties of currently used commercial magnesium alloys.

Materials and methods

The ML10 and ML-OPB alloys were supplied by SOMZ LLC (Solikamsk). Magnesium (99.9 wt.% purity), zinc (99.975 wt.%), and Mg—15wt.%Zr (SOMZ LLC), Mg—20wt.%Y and Mg—20wt.%Nd (Metagran LLC, Moscow) master alloys were used to prepare the EWZ43 alloy.

Samples for corrosion tests were obtained by flux-free melting. Melting in the PT 90/13 resistance furnace (LAC, Czech Republic) was carried out in a steel crucible in a protective atmosphere of argon mixture with 2 vol.% sulfur hexafluoride (SF_6). The weight of alloy charge was 2 kg. After the raw materials was melted and the temperature was raised to 740–760 °C, the melt was purged with argon for 3 min through a steel tube. The melt was poured into the molds at the same temperature after a 10-minute holding in the furnace.

All other samples were obtained by flux melting technology, which was conducted in an induction furnace (RELTEK RRE, Ekaterinburg) in a steel crucible. The weight of the alloy charge was 2–4 kg. Melting was carried out under a flux on the basis of carnallite ($KCl \cdot MgCl_2$). Once the raw materials had been melted, the melt temperature was raised to 740 °C and a carnallite flux was added to clean the melt from non-metallic inclusions. The finished melt was held in the furnace for 10 min and then poured into the molds at a temperature of 740 °C. The mold temperature was 25 ± 2 °C.

To study the alloy microstructure, corrosion resistance and flammability, cylindrical ingots 35 mm in diameter and 150 mm in height were cast in a steel mold.

The chemical composition of ML10 and ML-OPB alloys was taken from the alloy data sheets, and for the EWZ43 alloy it was determined by optical emission spectroscopy on the ARGON-5SF spectrometer (Spectrosoft LLC, Troitsk). The composition of the alloys is presented in Table 1.

The microstructure and phase composition of the alloys were studied using a Vega SBH3 scanning electron microscope (SEM) (Tescan, Czech Republic) with an energy dispersive X-ray microanalysis (EDS) attachment (Oxford, UK).

The phase composition of the alloys was calculated using the “Thermo-Calc 2016a” software (Thermo-Calc Software, Sweden) [22] with the TCMG4 thermodynamic database (TCS Mg-based Alloys Database version 4) [23].

All alloys were heat-treated (HT) according to the T6 regime consisting of solution HT ($t = 525\text{ °C}$ for $\tau = 24\text{ h}$ — ML-OPB; $t = 525\text{ °C}$, $\tau = 8\text{ h}$ — EWZ43; $t = 530\text{ °C}$, $\tau = 10\text{ h}$ — ML10) followed by quenching in water and aging ($t = 200\text{ °C}$, $\tau = 100\text{ h}$ — ML-OPB; $t = 250\text{ °C}$, $\tau = 9\text{ h}$ — EWZ43; $t = 200\text{ °C}$, $\tau = 8\text{ h}$ — ML10).

To determine the mechanical properties of the alloys, the rectangular ingots were made by casting in a graphite mold [24]. Six cylindrical specimens with 5 mm gauge diameter were obtained from ingots for the tensile tests by lathing. The tensile test was conducted on the 5569 universal testing machine (Instron, USA) with an advanced video extensometer (Instron, USA).

Besides the mechanical properties in the HT-state, the mechanical properties after a long-time elevated temperature holding of the alloy samples at $t = 300\text{ °C}$ for 500 h were determined. The crucibles with samples were held in a forced-air furnace that provided both mixing of air inside the furnace and supply of new portions of air. The air flow velocity was measured with a 405i thermo-anemometer (Testo, Germany) and

was 0.06–0.2 m/s. The dimensions of the samples are shown in Fig. 1, *a*. Tensile tests were carried out on 3 specimens which had not been held out (in the HT state) and 3 specimens which had been held out at high temperature.

Samples for corrosion testing were cut from ingots using wire cutting. Corrosion tests were performed on cubic samples with dimensions of $12 \times 12 \times 12\text{ mm}$ and a surface area of approx. 9.5 cm^2 . The corrosion rate was determined by the volumetric method based on measuring the amount of hydrogen released during corrosion. The tests were performed in a 3 wt.% NaCl aqueous solution at room temperature for 48 h. The volume of the solution was 500 mL. Prior to immersion in the corrosion environment, the surface of the samples was

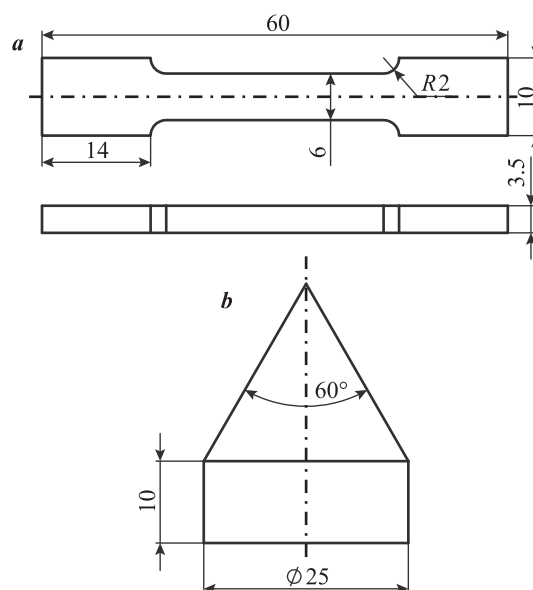


Fig. 1. The tensile test sample after longtime holding at elevated temperature (*a*) and a conical sample for alloy ignition testing in a gas burner flame (*b*)

Рис. 1. Образец для испытаний на растяжение после длительной выдержки при повышенной температуре (*a*) и конусный образец для проведения испытаний на возгорание сплава в факеле газовой горелки (*b*)

Table 1. The composition of investigated alloys, wt.%

Таблица 1. Состав исследуемых сплавов, мас.%

Alloy	Mg	Y	Nd	Zn	Zr	Ce	Yb
ML-OPB	Bal.	6.67	–	2.62	0.46	0.35	0.35
EWZ43	Bal.	3.76	4.39	0.63	0.58	–	–
ML10	Bal.	–	2.36	0.27	0.51	–	–

grounded with P320 grit sandpaper and degreased with ethyl alcohol. The amount of released hydrogen was converted into the mass loss of the sample according to the ratio of 1 mL H₂ = 1 mg Mg [25] and the corrosion rate was calculated in mm/year using the standard method [26].

Electrochemical studies for alloys in a 3 wt.% NaCl aqueous solution were performed using an IPC PRO MF/FRA potentiostat/galvanostat (Volta STC, St. Petersburg) at room temperature (25 ± 2 °C). Measurements were performed in a three-electrode cell in which the alloy sample was the working electrode with an effective area of 1.6 cm². Platinum and saturated silver/silver chloride (Ag/AgCl) electrodes were used as counter and reference electrodes, respectively. Potentiodynamic polarization experiments were performed from the cathode region at –2300 mV to the anode region at +(1300+500) mV at a scan rate of 1 mV/s. The corrosion current density and corrosion potential were determined using Tafel curves. Using the values of corrosion current density, the corrosion rate of the alloys was calculated [27]. Electrochemical measurements were repeated three times for each alloy.

The study of the fluidity of alloys was carried out with a spiral fluidity test. The molds for pouring the spiral test were made of resin bonded sand. For mold production according to “no-bake” process, the FK-5 binder and the OK-3 catalyst were used in the amount of 1.2 and 0.5 % of the sand mass (both produced by “Intema Group”, Pushkino, Russia), respectively. Quartz sand (deposit — Ryazan region) was used. The ignition inhibitor was potassium tetrafluoroborate (KBF₄) added in the amount of 0.5 % of the sand.

The mixture was prepared in a Mieszarki RN12/VL2 mixer (Multiserw-Morek, Poland). First the sand and ignition inhibitor were mixed, then the catalyst and, after it was evenly distributed, the binder were added to the mixture. After introducing each of the components, the mixture was mixed for 2 min.

Before pouring, the casting mold was aligned horizontally with a bubble level to determine fluidity. A wooden stopper was placed in the pouring cup, blocking the sprue. Melt was poured into the cup of the mold at 790–810 °C (50–60 °C above the temperature at which the fluidity was determined). After filling the cup with melt, the temperature changes on the thermocouple located in the cup center were monitored. As soon as the temperature of the thermocouple reached the pouring temperature of 740 °C (after 5–15 s), the stopper was lifted. The spiral fluidity test was repeated 4 times. The temperature was monitored using the BTM-4208SD 12-channel temperature re-

corde (Lutron, Israel). K-type thermocouples were used.

The hot tearing susceptibility test was carried out in the molds made of resin bonded sand. The melt was poured into the molds at 780–800 °C. The maximum ring width (in mm) at which a crack was detected was considered as a measure of hot tearing susceptibility (HTS), assuming that no cracks were detected at subsequent rings of greater width. The width of the poured rings ranged from 5 to 25 mm in increments of 2.5 mm. For each ring width, 2–4 probes were poured. Also the HTS of the alloys was determined by the “Dog-bone” test. The sample as a casting has a massive sprue with side branches of different lengths, but with the same cross-sectional area [29]. The end of each branch ended with a ball-shaped thickening, creating a hindered contraction. The “Dog-bone” probe was poured into a steel mold with a vertical parting line. The HTS of the alloys was assessed by the maximum branch length without cracks. 4 probes were poured for each alloy at a casting temperature of 740 °C.

To determine the influence of the mold material on the surface quality of the castings, two castings of different configurations were made. The first represented bars with thickness 10, 20 and 30 mm, connected by a gating system — its scheme is presented in a work [28]. The second casting was a cylinder 60 mm in diameter and 135 mm length. Two types of resin bonded sand mixtures, with and without ignition inhibitor addition, were used to manufacture the mold for cylinder casting. Potassium tetrafluoroborate (KBF₄) was used as an ignition inhibitor in the amount of 0.5 % of the sand mass. No ignition inhibitor was used to obtain castings with bars of varying thickness. The nature of interaction between the alloy and the mold material and the effect of inhibitors on this interaction were evaluated visually by the surface quality of the castings obtained.

To determine the ignition temperature, rectangular samples of 10×10×5 mm were cut from ingots. Their surfaces were grounded with P400 grit sandpaper. A hole 1.5 mm in diameter and 3–5 mm deep was drilled in each sample, into which the junction of a K-type thermocouple was mounted.

During the tests, alloy samples were placed in a steel crucible. Using an induction furnace, they were heated at a constant rate of 5 °C/s. The ignition temperature of the alloy was determined by a sharp increase in the temperature on the heating curve, and visually by the appearance of flashes on the surface of the melted sample.

Cone-shaped samples were turned from ingots on a lathe for ignition test of the alloy in the gas burner flame (Fig. 1, *b*). The sample was placed on a sheet of asbestos with the tip upwards. The junction of a K-type thermocouple mounted on a tripod was placed 1–2 mm away from the tip of the cone to fix the flame temperature in the area of the cone tip. The flame of the gas burner was directed at the tip of the cone and a countdown began, simultaneously recording the temperature of the flame, which was approx. 1300 °C. In the course of the experiment the time to the appearance of the ignition source was visually recorded.

The molds for producing the “Bracket” casting were made using 3D printing. The molds were made using the Binder jetting technology using an SP 500 3D printer (Additive Technologies LLC, St. Petersburg). We used a furan-based BindEX+ binder (Prom-KhimTech LLC, Ivanteevka, Russia). The castings made of the ML-OPB, EWZ43 and ML10 alloys were casted in the printed molds.

A gas burner was placed in a specially prepared chamber made of refractory bricks, which provided a persistent flame for a long period of time. The casting was placed at a fixed distance from the burner, ensuring its presence in the flame. The temperature of the flame at the casting location was recorded using a K-type thermocouple and was ~1100 °C. The purpose of the test is to record the time until at least one ignition source has appeared.

Results and discussion

Figure 2, *a–c* represents the microstructure of the ML-OPB alloy. In the as-cast state (Fig. 2, *a*) in the structure of the alloy in addition to the primary dendrites of the magnesium solid solution α -Mg there is a significant amount of eutectic phase, which, according to the results of EDS analysis, has the composition, at. %: Mg–3.9Zn–6.2Y–0.42Zr–0.26Ce–0.09Yb. Based on the calculations performed with ThermoCalc, this phase is an LPSO-phase (Mg_{12}ZnY or $\text{Mg}_{21}\text{Zn}_2\text{Y}_2$). The precipitates in the center of the grains are zirconium based solid solution α -Zr. Heat treatment of the ML-OPB alloy leads to a change in the morphology of the LPSO-phase to lamellar as well as the formation of zirconium-rich needle precipitates in the center of the grain (Fig. 2, *b*). The long-time holding at elevated temperature causes the formation of tiny precipitates at grain boundaries. Due to their small size it is impossible to determine the composition of this phase, however, according to the EDS the precipitates of this phase are rich in Y and Zn.

Fig. 2, *d–f* shows the microstructure of the EWZ43 alloy in the as-cast and heat-treated states, as well as after long-time holding at elevated temperature for 500 h. Earlier in paper [15], the phase composition of this alloy was investigated and it was revealed that in the as-cast state in the structure of the alloy in addition to the α -Mg there is the eutectic Mg_3Nd phase, which transforms into the $\text{Mg}_{41}\text{Nd}_5$ phase after the HT. Long-time holding at elevated temperature, as in the case of the ML-OPB alloy, causes the formation of tiny precipitations located on the grain boundaries. The precipitates are enriched in Y and Nd according to the results of the EDS.

Fig. 3, *a* provides the tensile properties of the ML-OPB and EWZ43 alloys in the HT condition. The data for the EWZ43 alloy are taken from work [15] for two aging temperatures (200 and 250 °C). The tensile properties of the ML10 alloy are also given for comparison [30]. The ML-OPB alloy exhibits sufficiently similar tensile yield strength (TYS) and ultimate tensile strength (UTS) values to those obtained for the ML10 alloy, but with a significantly higher elongation at fracture (El). For the EWZ43 alloy, the maximum values of TYS and UTS are observed, but the minimum value of El among the materials is under consideration.

Fig. 3, *b* represents the tensile properties of the ML-OPB and EWZ43 alloys prior to and after long-time holding at elevated temperature. Since the tests in this case were performed on samples of a different configuration with a small cross-sectional area (see Fig. 1, *a*), they cannot be compared with the results of tensile tests obtained on full-size standard samples (Fig. 3, *a*). It can be seen that the ML-OPB and EWZ43 alloys show a significant decrease in TYS and UTS after a long-time holding at elevated temperature. The reduction in El for the ML-OPB alloy is especially significant (~50 %). At the same time, El for the EWZ43 alloy remains practically unchanged. Previously, it was pointed out in microstructure analysis that long-time holding at elevated temperature leads to phase precipitation along the grain boundaries, and it seems that these precipitations, as well as the loss of lattice coherence between the α -Mg and the precipitates released during ageing, cause a decrease in the mechanical properties.

After the long-time holding at elevated temperature, the oxide layer on the surface of the ML-OPB and EWZ43 alloy samples was investigated. Its element content, based on the EDS results, is provided in Table 2. It can be seen that during oxidation of the ML-OPB alloy sample, Y constitutes the main ele-

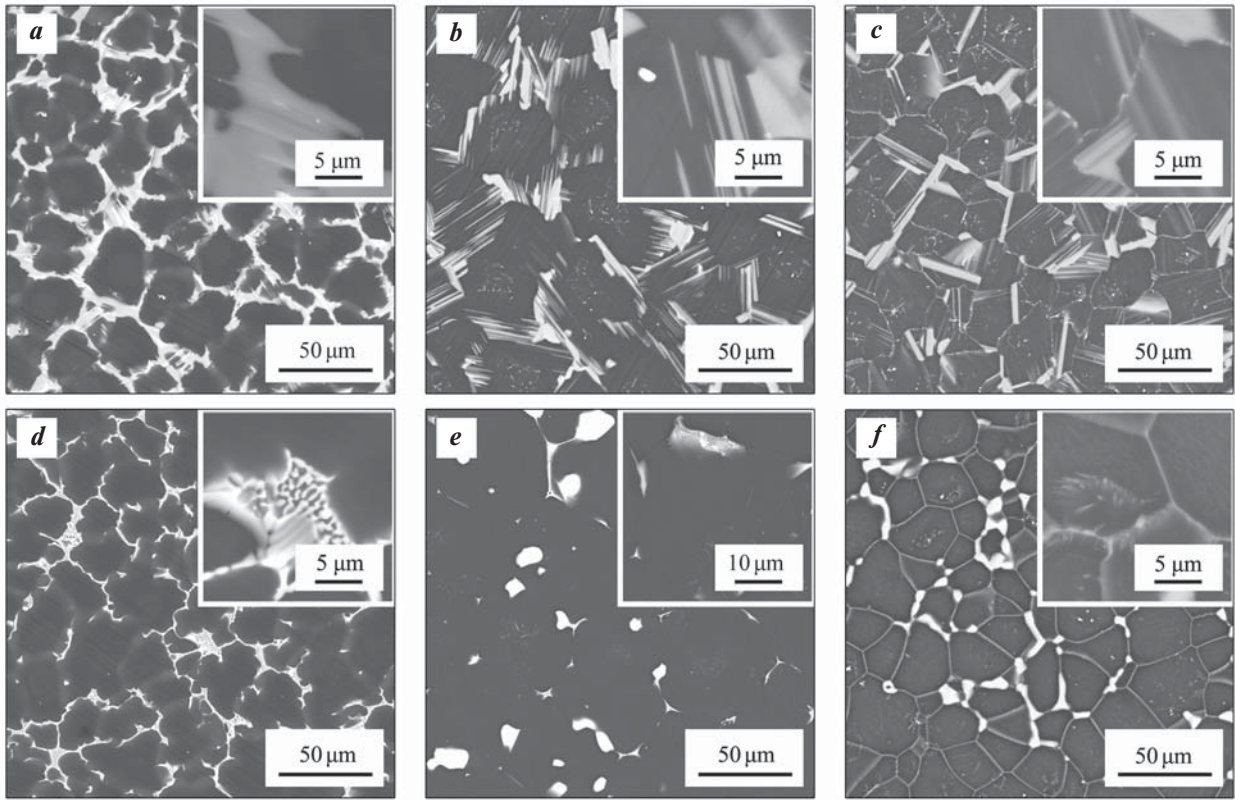


Fig. 2. Microstructure of ML-OPB alloy (*a–c*) and EWZ43 (*d–f*) in as-cast condition (*a, d*), heat-treated condition (*b, e*), and after longtime holding at elevated temperature (*c, f*)

Рис. 2. Микроструктура сплавов МЛ-ОПБ (*a–c*) и EWZ43 (*d–f*) в литом (*a, d*) и термообработанном (*b, e*) состояниях, а также после длительной высокотемпературной выдержки (*c, f*)

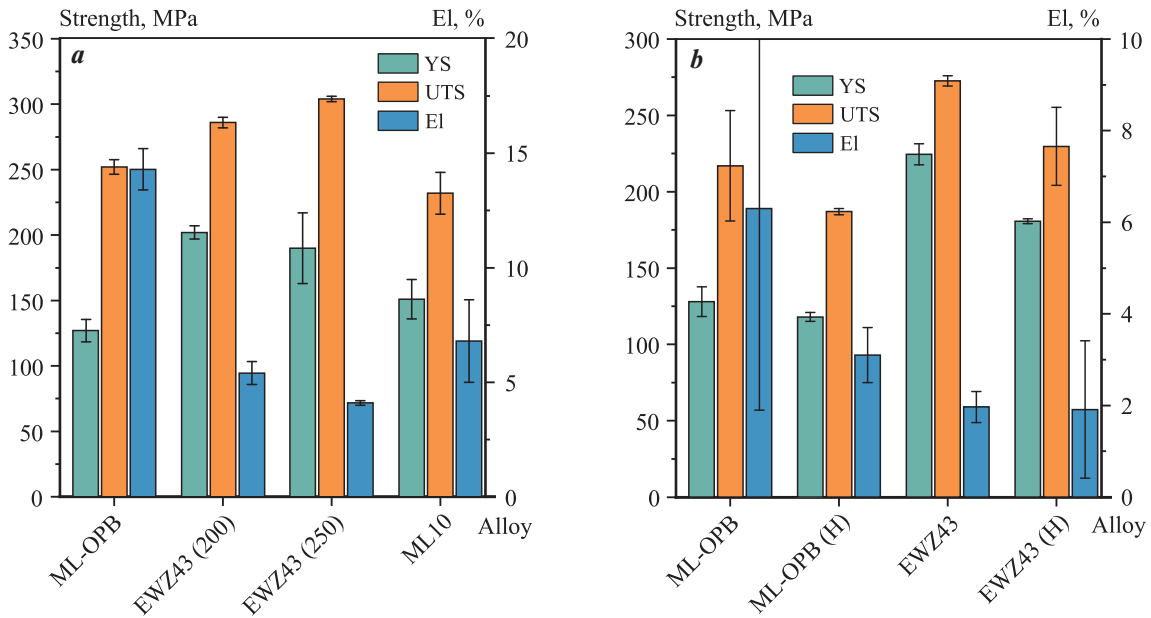


Fig. 3. Tensile properties of ML-OPB, EWZ43, and ML10 alloys after heat treatment (in parentheses the aging temperature of the EWZ43 alloy is indicated) (*a*), as well as the tensile properties of ML-OPB and EWZ43 alloys before and after longtime holding at elevated temperature (indicated by the B) at $t = 300\text{ }^{\circ}\text{C}$ for 500 h (*b*)

Рис. 3. Механические свойства при растяжении сплавов МЛ-ОПБ, EWZ43 и МЛ10 в термообработанном состоянии (в скобках указана температура старения сплава EWZ43) (*a*), а также сплавов МЛ-ОПБ и EWZ43 до и после длительной высокотемпературной выдержки (с буквой В) при $t = 300\text{ }^{\circ}\text{C}$ в течение 500 ч (*b*)

ment comprising the oxide film apart from Mg. There is also a higher Yb content in the oxide film than in the alloy. Regarding the other alloying elements of the ML-OPB alloy (Zn, Zr and Ce), their concentration in the oxide film is much lower than that observed in the alloy.

The predominant elements for the EWZ43 alloy whose content in the oxide layer is higher than that in the alloy are Y and Nd. The rest of the alloying elements are contained in the film either in close or much lower quantities than in the alloy.

Thus, such elements as Y (for both alloys), Nd (for the EWZ43 alloy), and Yb (for the ML-OPB alloy) play a protective role in the oxidation of the ML-OPB and EWZ43 alloys. The thickness of the surface oxide layer after a long-time holding at elevated temperature was from 10 to 30 μm for both alloys, indicating their high heat resistance at $t = 300\text{ }^\circ\text{C}$.

Fig. 4, *a* shows the amount of released hydrogen during corrosion tests of the ML-OPB and EWZ43 alloys in a medium of a 3 wt.% NaCl aqueous solution. It should be noted that during the tests, the intensity of hydrogen release for the ML-OPB alloy increases with time, while for the EWZ43 alloy it is almost constant. This pattern is not common in less-alloyed magnesium alloys. For comparison, the results of similar corrosion tests with the ML10 alloy from work [31] were added in Fig. 4, *a*. It can be seen that the corrosion rate is steadily decreasing due to the protective effect of the layer of corrosion products formed on the alloy surface.

Typical polarization curves for the ML-OPB and EWZ43 alloys obtained in a 3 wt.% NaCl aqueous solution are shown in Fig. 4, *b*. The average values of the corrosion potential, the corrosion current density and the calculated corrosion rate of the alloys under investigation, as determined from the polarization curves, are presented in Table 3. The values of these parameters

for the ML5 alloy obtained under similar conditions are also included in this Table [32]. It can be seen that the corrosion potential of the ML-OPB and EWZ43 alloys is almost the same and it is much more negative than that of the AZ91 alloy. At the same time, the corrosion current density is lower for the ML-OPB alloy compared to the EWZ43 alloy, and it is maximum for the AZ91 alloy.

Based on the results of hydrogen release corrosion tests and electrochemical research, the corrosion rates of the alloys were calculated (see Table 3). It can be seen that the corrosion rate determined from the electrochemical corrosion tests for the ML-OPB and EWZ43 alloys is much lower than that determined in the long-term immersion corrosion tests (by hydrogen release). In general, the corrosion rate for the alloys under investigation, calculated in hydrogen release tests, is 3–4 times higher than for the most common used commercial magnesium alloys (AZ91 and ML10).

Typically, the corrosion rate determined by Tafel fitting of polarization curves is equal to or lower than the corrosion rate determined by long-term immersion test (by hydrogen release), in particular, this pattern can be observed for the AZ91 alloy (Table 3). This is due to the fact that during the corrosion process, the resulting corrosion products cover the surface of the sample and thus prevent its contact with the corrosive environment. A possible reason to explain the increasing corrosion rate of the ML-OPB alloy as the corrosion process occurs is due to the microstructure of the alloy under investigation (see Fig. 2, *b*). Thus, the LPSO phase, which serves as cathode with respect to the α -Mg, is found in a structure in the form of coarse plates. During the corrosion process, the α -Mg dissolves and the surface area of the cathode phase increases [33], which leads to an increase in the corrosion rate.

Fig. 5 represents the values of fluidity obtained by the spiral test, hot tearing susceptibility (HTS) obtained

Table 2. The elements content at the surface of ML-OPB and EWZ43 alloys samples after longtime holding at elevated temperature obtained by Energy-dispersive X-ray spectroscopy

Таблица 2. Содержание элементов в оксидной пленке образцов сплавов МЛ-ОПБ и EWZ43 после длительной высокотемпературной выдержки по результатам РСМА

Alloy	Content, at.% / wt.%								
	Mg	Y	O	C	Nd	Zn	Zr	Ce	Yb
ML-OPB	65.8/59.3	6.4/21.3	21.0/12.5	5.9/2.6	–	0.18/0.43	0.18/0.59	0.10/0.53	0.39/2.47
EWZ43	58.1/53.1	4.9/16.4	28.9/17.4	5.9/2.7	1.7/9.4	0.05/0.13	0.16/0.54	–	–

Table 3. Results of electrochemical corrosion tests and hydrogen evolution corrosion tests for ML-OPB, EWZ43, ML10 and AZ91 alloys

Таблица 3. Результаты электрохимических коррозионных испытаний и коррозионных испытаний по выделению водорода для сплавов МЛ-ОПБ, EWZ43, МЛ10 и МЛ5

Alloy	Electrochemical corrosion tests			Corrosion tests by hydrogen release
	Corrosion potential, V	Corrosion current density, $\mu\text{A}/\text{cm}^2$	Corrosion rate, mm/year	Corrosion rate, mm/year
ML-OPB	-1.53 ± 0.03	74.4 ± 6.9	1.69 ± 0.16	6.93 ± 0.39
EWZ43	-1.56 ± 0.03	94.2 ± 26.5	2.12 ± 0.60	6.27 ± 1.05
ML10 [31]	–	–	–	0.95 ± 0.14
ML5 [32]	-1.42 ± 0.02	115.4 ± 20.8	2.47 ± 0.45	2.10 ± 0.08

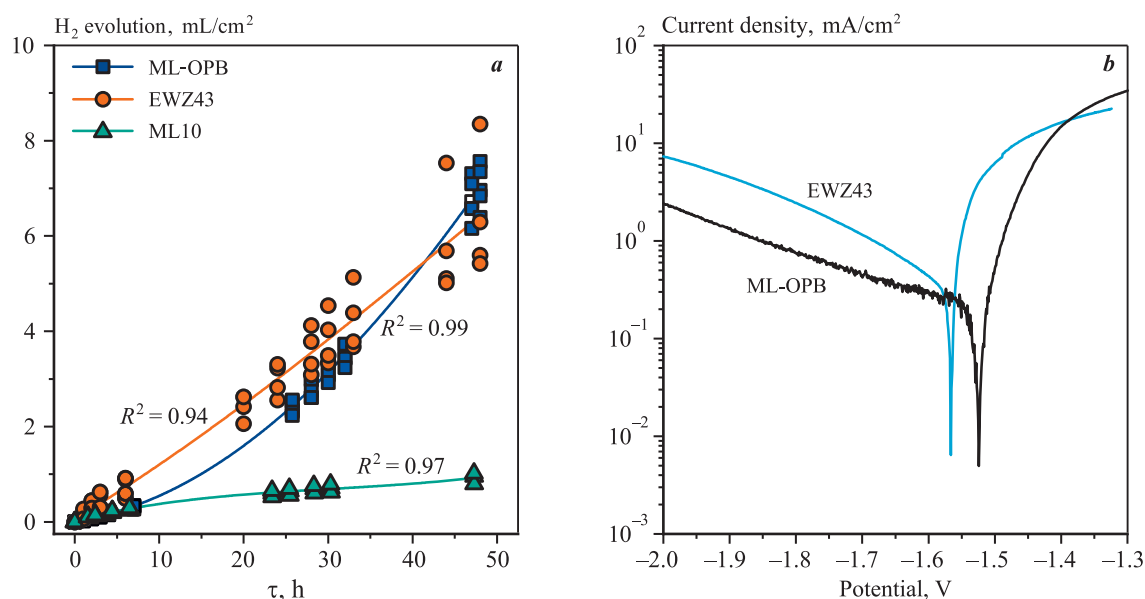


Fig. 4. The amount of hydrogen released during corrosion testing of ML-OPB, EWZ43, and ML10 alloys in a 3 wt.% NaCl aqueous solution (a) and polarization curves for ML-OPB and EWZ43 alloys in a 3 wt.% NaCl aqueous solution (b)

Рис. 4. Количество выделившегося водорода в ходе коррозионных испытаний сплавов МЛ-ОПБ, EWZ43 и МЛ10 в среде 3 мас. %-ного водного раствора NaCl (a) и поляризационные кривые для сплавов МЛ-ОПБ и EWZ43 в среде 3 мас. %-ного водного раствора NaCl (b)

by the ring and “Dog-bone” tests of the ML-OPB and EWZ43 alloys at a pouring temperature of 740 °C. It can be seen that the value of fluidity of the EWZ43 alloy coincides with that obtained for the AZ91 alloy (it was determined under similar conditions [32]), and the ML-OPB alloy exceeds the fluidity of these alloys (Fig. 5, a). It seems that the maximum fluidity of the ML-OPB alloy under consideration is associated with a large amount of eutectic in its structure, as well as with

a fairly short freezing range of alloys with the LPSO-phase [21].

Fig. 5, b shows the results of determining the HTS of alloys by the ring test. There are no confidence intervals for a number of alloys since there was a high degree of reproducibility of the results and for each ring width all three castings showed the same result. For the ML-OPB and EWZ43 alloys, the HTS, which indicates the maximum ring width at which the crack

appears, was found to be 15 and 17.5 mm, respectively. At the same time, according to OST (Industrial Standard) 1 90020-71 the HTS for the industrial AZ91 alloy is 30 mm. That is, the resistance to formation of hot cracks in the studied alloys is significantly higher than that of the AZ91 alloy. The reason for this is most likely that the AZ91 alloy exhibits a rather long freezing range, whereas the ML-OPB and EWZ43 alloys have a fairly short freezing range, moreover, their structure contains more eutectic. Because of the relatively short freezing range, the HTS of the ML10 alloy, according to OST (Industrial Standard) 1 90020-71, is 15–20 mm, i.e. comparable to the alloys under investigation. Also, the low HTS of the ML-OPB and EWZ43 alloys is promoted by the fine grain size, which is ensured by the presence of zirconium in the alloy [34].

Fig. 5, *c* represents the HTS values for the ML-OPB, EWZ43 and ML10 alloys obtained by the “Dog-bone” test. For the ML-OPB alloy, a complete absence of cracks was observed, indicating minimal HTS. The maximum crack-free branch length for the AZ91 alloy was 50 mm [32], which confirms the conclusions that the tendency to form hot cracks in the ML-OPB alloy is much lower than in the most common commercial cast magnesium alloy — AZ91. The EWZ43 alloy occupies an intermediate position between the specified alloys.

Rectangular bar castings with various thicknesses of the ML-OPB and EWZ43 alloys were poured into the molds made of resin bonded sand. The element content in the oxide film of the bars as determined by EDS

is shown in Fig. 6. The oxide film in all cases mainly contains C, O, Mg, and Y. The content of C in Fig. 6 is not given and can be calculated as a difference between 100 % and the contents of the other elements shown in the charts. In the MgO—Y₂O₃ system no ternary phases are formed [35], therefore it can be assumed that the film structure is composed of a mixture of MgO and Y₂O₃ phases. The ratio of Mg to Y in the film depends on the thickness of the bar. Thus, for a 10 mm thick bar, the magnesium content in the film is higher than the yttrium content, whereas in 20 and 30 mm thick bars the situation is reversed and the yttrium content is 1.5–2.0 times higher than that of magnesium. The quantitative ratio of the phase fractions cannot be established because the thickness of the film is shallow and the alloy of the bar under oxide layer affects the analysis result. That is, the higher magnesium content in a 10 mm thick bar is related to the fact that it bears a thinner oxide film. The composition of the oxide film for the ML-OPB and EWZ43 alloys is quite similar. The only difference is in the presence of a small amount (less than 1 at.%) of Nd in the EWZ43 alloy film. The remaining alloying elements (Zn, Zr, Ce and Yb) are virtually absent in the oxide film and do not affect the interaction of the ML-OPB and EWZ43 alloys with the resin bonded sand.

On the surface of cylindrical ingots with a diameter of 60 mm, after pouring into the molds without a ignition inhibitor in the resin bonded sand, separate areas of metal-mold interaction are observed, which is expressed as the appearance of defects in the form

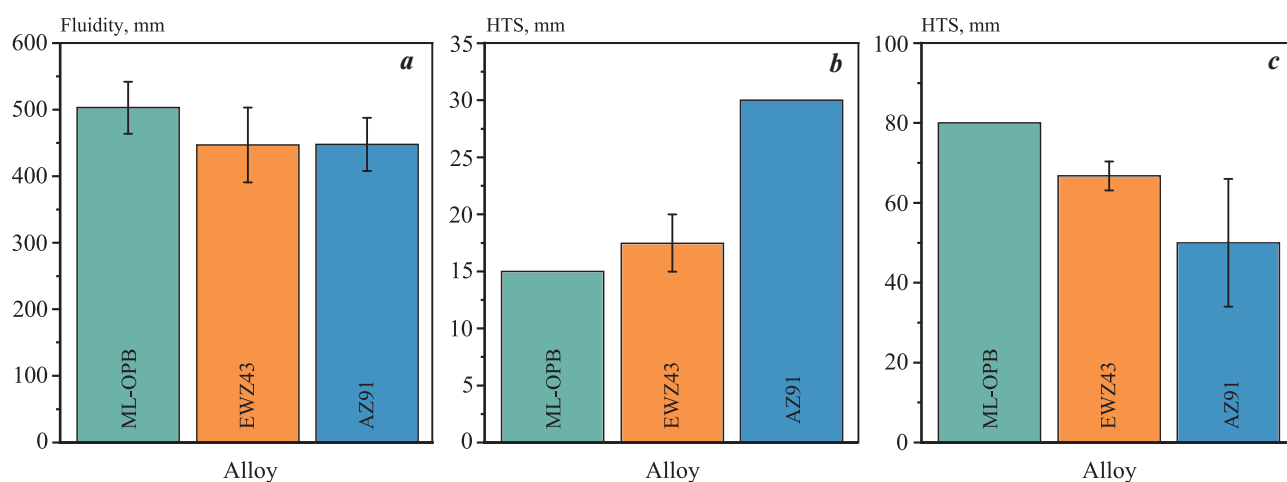


Fig. 5. Fluidity (*a*), hot tearing criterion obtained by the ring probe (*b*) and hot tearing criterion obtained by the «Dog-bone» test (*c*) for ML-OPB, EWZ43 and AZ91 alloys

Рис. 5. Жидкотекучесть (*a*), число горячеломкости по кольцевой пробе (*b*) и горячеломкость по пробе «Арфа» (*c*) для сплавов МЛ-ОПБ, EWZ43 и МЛ5

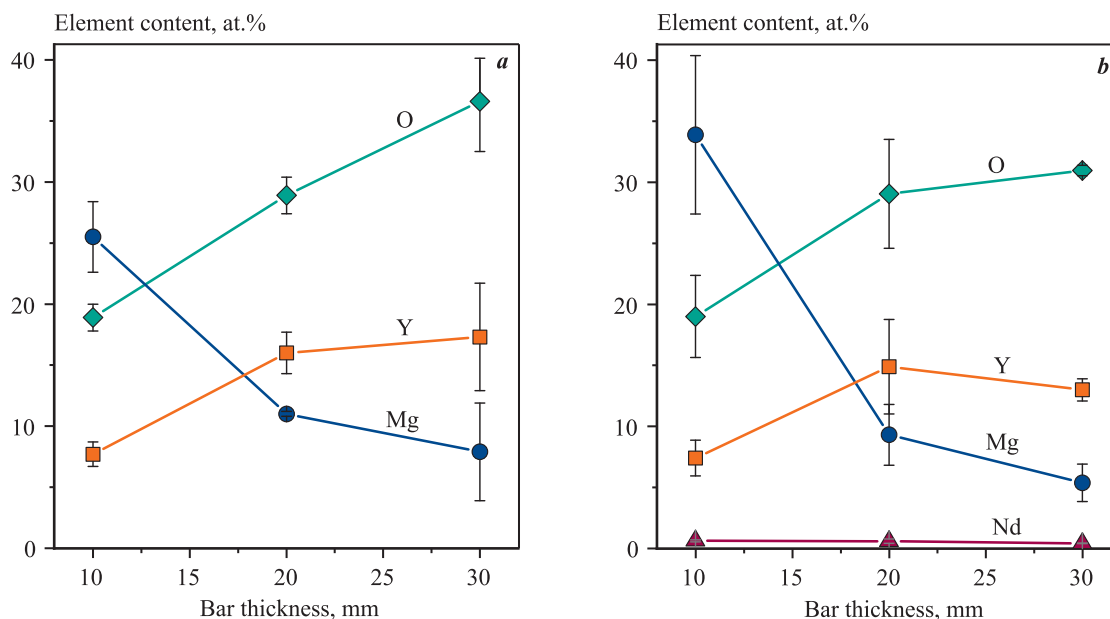


Fig. 6. The elements content in the oxide layer of ML-OPB (a) and EWZ43 (b) alloys bars with different thicknesses

Рис. 6. Содержание элементов в оксидной плене брусков различной толщины для сплавов МЛ-ОПБ (a) и EWZ43 (b)

of cavities. When KBF_4 was used as an inhibitor, there were practically no ignition sources on the surface of the cylindrical ingots. This pattern was observed for both alloys studied.

We determined the ignition temperature for the alloys ML-OPB, EWZ43, as well as ML10. Fig. 7, a shows a typical heating curve of the ML-OPB alloy sample in air. It can be seen that during heating at 1077°C there is a sharp increase in a temperature associated with additional heat release due to ignition of the sample. It should be noted that not in all cases the thermocouple readings were able to fix the ignition temperature, so at the same time we monitored the ignition visually.

Fig. 7, b shows the ignition temperatures of the ML-OPB, EWZ43 and ML10 alloys. It can be seen that the minimum ignition temperature of $878 \pm 73^\circ\text{C}$ is observed for the ML10 alloy. The ML-OPB and EWZ43 alloys exhibit a higher value of 1022 ± 36 and $1054 \pm 33^\circ\text{C}$, respectively. Thus, the presence of Y in ML-OPB and EWZ43 alloys significantly increases their ignition temperature. Upon that, the EWZ43 alloy, which has a lower Y content than the ML-OPB alloy, exhibits the maximum ignition temperature. Apparently, the higher ignition temperature of the EWZ43 alloy is due to the presence of Nd. That is, Nd, as well as Ce [5, 8], contributes to the formation of a dense oxide film at lower Y concentrations.

Fig. 8, a illustrates a image of a cone-shaped ML-OPB alloy sample in the flame of a gas burner af-

ter 6 min from the beginning of the experiment. It can be seen that the sample has slightly changed its shape as a result of melting, but no ignition sources can be observed. Once 6 min had elapsed, the cone-shaped sample came into contact with the burner, whereupon it instantly lost its shape and flowed over the surface (Fig. 8, b). This suggests that the sample was primarily liquid and that its shape was preserved only due to the presence of a sufficiently strength oxide film. A similar behaviour was observed for the sample of alloy EWZ43, which, even after complete melting, could not show any ignition. As for the ML10 alloy, the average ignition time for it turned out to be 240 ± 63 s. The ignition sources on the cone-shaped sample made of the ML10 alloy can be seen in Fig. 8, c and d. Thus, it can be stated that the ignition resistance of the ML-OPB and EWZ43 alloys is extremely high and greatly exceeds that of the ML10 alloy.

Fig. 9 illustrates images of castings made of the ML-OPB, EZW43 and ML10 alloys, taken after 100 s from the start of ignition tests in the flame of a burner simulating an open fire on an aircraft. For the ML10 alloy (Fig. 9, c) the first ignition sources were observed 70 s after placing the casting in the burner flame. And already in the 100th second the multiple ignition sources can be seen. After the burner flame was turned off and the casting came into contact with the atmosphere, there was a bright flash and the ML10 alloy casting burned completely (Fig. 9, d). In the ML-OPB and

EWZ43 alloys (Fig. 9, *a* and *b*), no ignition sources appeared even after complete melting of the casting and melt spreading. It can be seen that the oxide films

formed on the ML-OPB and EWZ43 alloy castings are quite strength and partially preserve the shape of the casting, forming a kind of cover from which the alloy

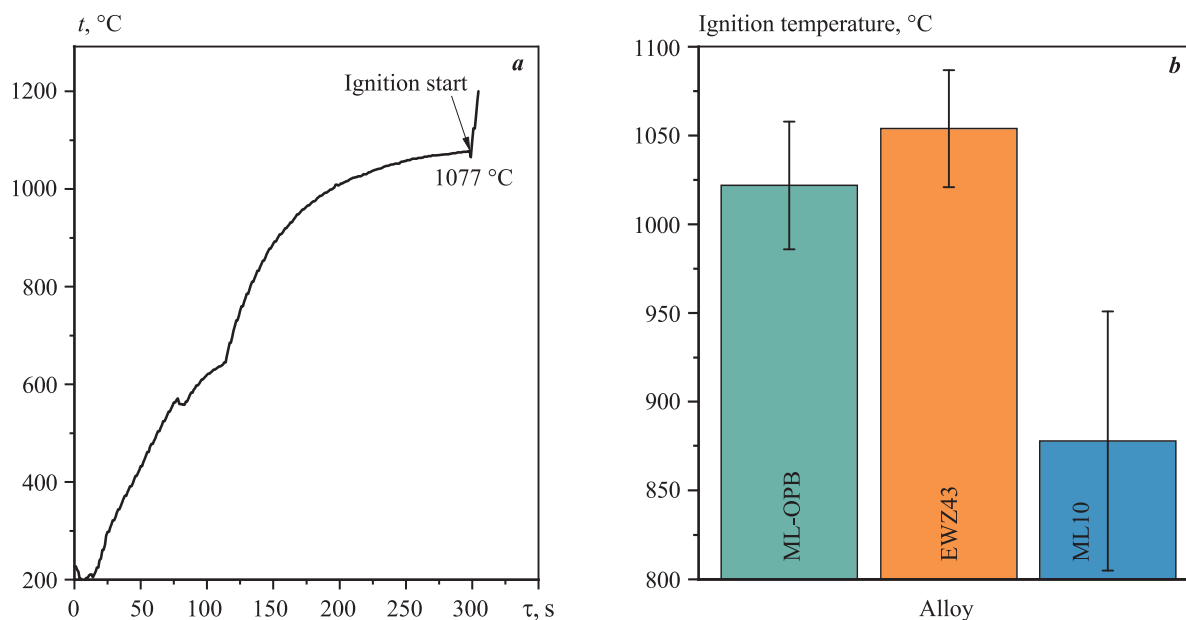


Fig. 7. The heating curve for ML-OPB alloy sample in air (*a*) and ignition temperature of ML-OPB, EZW43, and ML10 alloys samples (*b*)

Рис. 7. Кривая нагрева образца из сплава МЛ-ОПБ на воздухе (*a*) и температуры возгорания образцов из сплавов МЛ-ОПБ, EZW43 и МЛ10 (*b*)

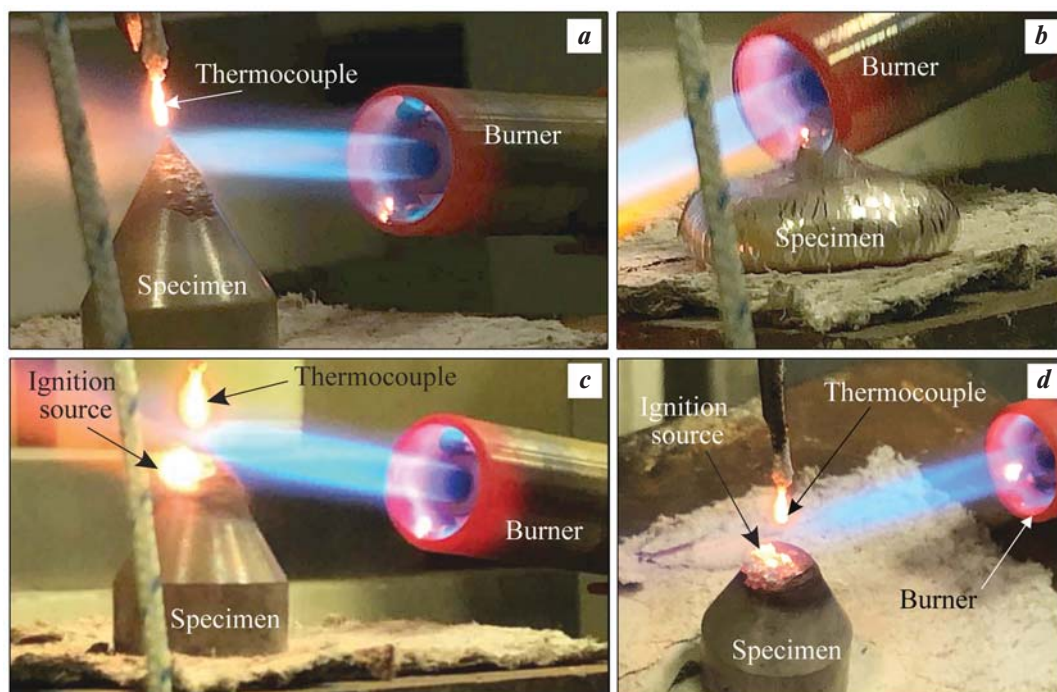


Fig. 8. The photographs of conical specimens made of ML-OPB (*a*, *b*) and ML10 (*c*, *d*) alloys during flammability tests in a gas burner flame

Рис. 8. Фотографии конусных образцов из сплавов МЛ-ОПБ (*a*, *b*) и МЛ10 (*c*, *d*) во время испытаний на возгорание в факеле газовой горелки

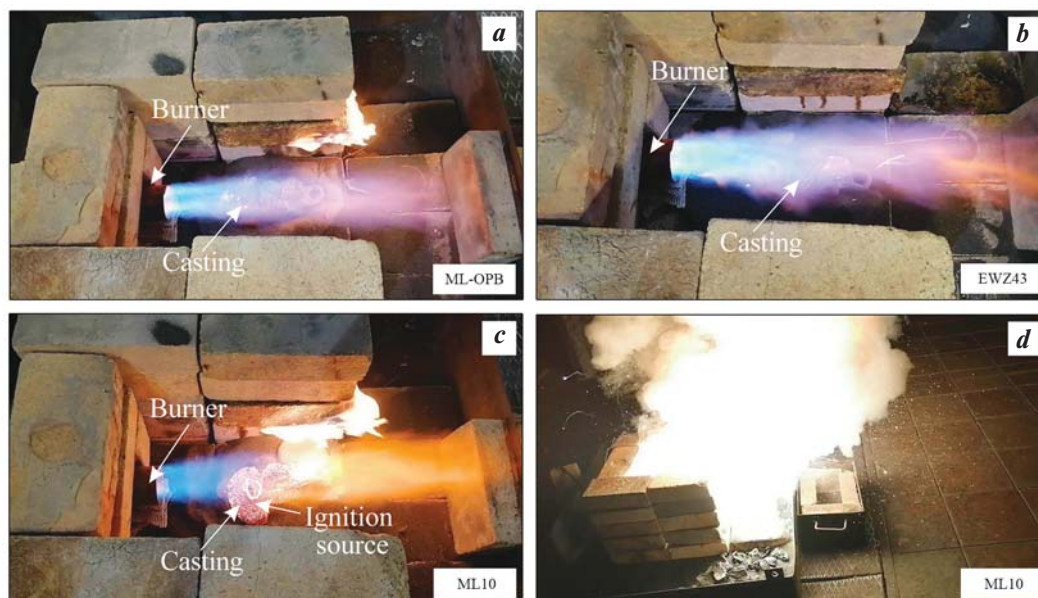


Fig. 9. The photographs of ML-OPB (a), EWZ43 (b) and ML10 (c) alloys castings after 120 s of flammability tests in a gas burner flame simulating an open fire on an aircraft, and combustion of a ML10 alloy casting at the end of the flammability experiment (d)

Рис. 9. Фотографии отливок из сплавов МЛ-ОПБ (a), EWZ43 (b) и МЛ10 (c) по прошествии 120 с испытаний на возгорание в пламени горелки, имитирующем открытый пожар на летательном аппарате, и горение отливки из сплава МЛ10 по окончании эксперимента (d)

flowed out. Upon that, the oxide films are kept heated to a high temperature by the burner flame and become glowing. After switching off the flame, the ML-OPB and EWZ43 alloys did not combust, unlike the ML10 alloy. These tests confirm that the ignition resistance of the ML-OPB and EWZ43 alloys is significantly higher than that of the ML10 alloy.

Conclusion

1. The microstructure of the ML-OPB alloy in the as-cast state consists of a α -Mg and LPSO-phase. As a result of HT, the morphology of the LPSO-phase changes to a lamellar one. Long-time holding at elevated temperature of samples made of the ML-OPB alloy ($t = 300\text{ }^{\circ}\text{C}$; $\tau = 500\text{ h}$) leads to the formation of precipitates on the grain boundary. The microstructure of the EWZ43 alloy consists of a α -Mg and the Mg_3Nd phase, which transforms into the $\text{Mg}_{41}\text{Nd}_5$ phase during the HT and its amount decreases significantly. The long-time holding at elevated temperature of the alloy also causes the formation of the grain boundary precipitates.

2. EWZ43 alloy significantly exceeds the tensile strength of the ML-OPB and ML10 alloys, but it exhibits small values of EI (about 5 % in T6 condition). The

tensile properties of ML-OPB and ML10 are similar, but ML-OPB exhibits higher EI. It was found that after a long-time holding at elevated temperature ($t = 300\text{ }^{\circ}\text{C}$; $\tau = 500\text{ h}$) the strength of the ML-OPB and EWZ43 alloys decreased, especially the EI for the ML-OPB alloy (twice). The reason for the decrease in properties is likely to be due to the precipitation of phases at the grain boundaries.

3. Long-time holding at elevated temperature of the alloys resulted in the formation of a Y-rich oxide film on the surface of the ML-OPB and EWZ43 alloy samples. Likewise, the Yb and Nd oxides in the ML-OPB and EWZ43 alloys, respectively, can play a protective role.

4. The corrosion rates of the ML-OPB and EWZ43 alloys in a 3 wt.% NaCl solution, determined during immersion corrosion test by the amount of hydrogen released, were 6.9 and 6.3 mm/year, respectively, which is much higher than those of the most common magnesium alloys — AZ91 and ML10 (2.1 and 0.9 mm/year, respectively). Thus, castparts made of ML-OPB and EWZ43 alloys require additional protection against corrosion.

5. The fluidity of ML-OPB and EWZ43 alloys was not lower than that of commercial magnesium alloys. The HTS of the ML-OPB and EWZ43 alloys is comparable to the HTS of the shot freezing range ML10

alloy and lower than that of the long freezing range AZ91 alloy. The specified castability properties for the ML-OPB alloy were slightly higher than for the EWZ43 alloy.

6. The study of the interaction of the ML-OPB and EWZ43 alloys with the resin bonded sand revealed that a ignition inhibitor is not necessary for castings with a wall thickness of 30 mm or less. This high resistance of the oxide film is explained by the formation of yttrium oxide in the surface layers of the oxide film of the casting. At the same time, a ignition inhibitor (e.g. KBF_4) may be required when producing castings with a wall thickness of 60 mm or more.

7. The ignition temperature for the ML-OPB and EWZ43 alloys was 1022 and 1054 °C, respectively, which is significantly higher than that for the ML10 alloy (878 °C). Tests of the alloys in the flame of a gas burner on the cone-shaped samples indicated that the ML-OPB and EWZ43 alloys practically do not ignite and that the ML10 alloy ignites after a certain period of time, even prior to the complete melting of the sample. During the tests of standard aircraft castings of the “bracket” type, made of test alloys, in an open flame of a gas burner, simulating a fire on the aircraft, it was found that castings of the ML-OPB and EWZ43 alloys do not ignite until they are completely melted. At the same time the casting of the ML10 alloy ignite at temperatures close to the melting point.

References

1. Czerwinski F. Overcoming barriers of magnesium ignition and flammability. *Advanced Materials and Processes*. 2014; 172: 28–31.
2. Marker T.R. Development of a laboratory-scale flammability test for magnesium alloys used in aircraft seat construction. Scientific report No. DOT/FAA/TC-13/52. Springfield: National Technical Information Services (NTIS), 2014.
3. Tekumalla S., Gupta M. An insight into ignition factors and mechanisms of magnesium based materials: A review. *Materials and Design*. 2017; 113: 84–98. <https://doi.org/10.1016/j.matdes.2016.09.103>
4. Tan Q., Atrens A., Mo N., Zhang M.X. Oxidation of magnesium alloys at elevated temperatures in air: A review. *Corrosion Science*. 2016; 112: 734–759. <https://doi.org/10.1016/j.corsci.2016.06.018>
5. Fan J.F., Yang Ch.L., Han G., Fang S., Yang W.D., Xu B.S. Oxidation behavior of ignition-proof magnesium alloys with rare earth addition. *Journal of Alloys and Compounds*. 2011; 509 (5): 2137–2142. <https://doi.org/10.1016/j.jallcom.2010.10.168>
6. Aydin D.S., Bayindir Z., Hoseini M., Pekguleryuz M.O. The high temperature oxidation and ignition behavior of Mg–Nd alloys. Part I: The oxidation of dilute alloys. *Journal of Alloys and Compounds*. 2013; 569: 35–44. <https://doi.org/10.1016/j.jallcom.2013.03.130>
7. Zhao S., Zhou H., Zhou T., Zhang Z., Lin P., Ren L. The oxidation resistance and ignition temperature of AZ31 magnesium alloy with additions of La_2O_3 and La. *Corrosion Science*. 2013; 67: 75–81. <https://doi.org/10.1016/j.corsci.2012.10.007>
8. Fan J.F., Cheng S.L., Xie H., Hao W.X., Wang M., Yang G.C., Zhou Y.H. Surface oxidation behavior of Mg–Y–Ce alloys at high temperature. *Metallurgical and Materials Transactions A*. 2005; 36 (1): 235–239. <https://doi.org/10.1007/s11661-005-0155-7>
9. Cheng C., Lan Q., Wang A., Le Q., Yang F., Li X. Effect of Ca additions on ignition temperature and multi-stage oxidation behavior of AZ80. *Metals*. 2018; 8: 766. <https://doi.org/10.3390/met8100766>
10. Inoue S.I., Yamasaki M., Kawamura Y. Formation of an incombustible oxide film on a molten Mg–Al–Ca alloy. *Corrosion Science*. 2017; 122: 118–122. <https://doi.org/10.1016/j.corsci.2017.01.026>
11. Kim Y.H., Kim W.J. Flame-resistant Ca-containing AZ31 magnesium alloy sheets with good mechanical properties fabricated by a combination of strip casting and high-ratio differential speed rolling methods. *Metals and Materials International*. 2015; 21: 374–381. <https://doi.org/10.1007/s12540-015-4338-5>
12. Duyunova V.A., Leonov A.A., Trofimov N.V., Rostovtseva A.S. Effect of qualitative and quantitative ratios of rare-earth elements in a new fireproof cast magnesium alloy. *Russian Metallurgy (Metally)*. 2021; 2021 (11): 1409–1412. <https://doi.org/10.1134/S0036029521110033>
Дуюнова В.А., Леонов А.А., Трофимов Н.В., Ростовцева А.С. Особенности влияния качественного и количественного соотношения редкоземельных элементов в новом пожаробезопасном литейном магниевом сплаве. *Металлы*. 2021; (6): 34–38.
13. Konstantinov I.L., Baranov V.N., Sidelnikov S.B., Kulikov B.P., Bezrukikh A.I., Frolov V.F., Orelkina T.A., Voroshilov D.S., Yuryev P.O., Belokonova I.N. Investigation of the structure and properties of cold-rolled strips from experimental alloy 1580 with a reduced scandium content. *International Journal of Advanced Manufacturing Technology*. 2020; 109: 443–450. <https://doi.org/10.1007/s00170-020-05681-4>
14. Koltygin A.V., Bazhenov V.E., Belov V.D., Matveev S.V. Cast magnesium alloy: Pat. 2687359 (RF). 2018. (In Russ.).

- Колтыгин А.В., Баженов В.Е., Белов В.Д., Матвеев С.В. Литейный магниевый сплав: Пат. 2687359 (РФ). 2018.
15. Koltygin A.V., Bazhenov V.E., Khasenova R.S., Komissarov A.A., Bazlov A.I., Bautin V.A. Effects of small additions of Zn on the microstructure, mechanical properties and corrosion resistance of WE43B Mg alloys. *International Journal of Minerals, Metallurgy and Materials*. 2019; 26 (7): 858–868.
<https://doi.org/10.1007/s12613-019-1801-1>
 16. Zhu Y.M., Morton A.J., Nie J.F. The 18R and 14H long-period stacking ordered structures in Mg–Y–Zn alloys. *Acta Materialia*. 2010; 58 (8): 2936–2947.
<https://doi.org/10.1016/j.actamat.2010.01.022>
 17. Xu D., Han E.H., Xu Y. Effect of long-period stacking ordered phase on microstructure, mechanical property and corrosion resistance of Mg alloys: A review. *Progress in Natural Science: Materials International*. 2016; 26 (2): 117–128.
<https://doi.org/10.1016/j.pnsc.2016.03.006>
 18. Luo S.Q., Tang A.T., Pan F.S., Song K., Wang W.Q. Effect of mole ratio of Y to Zn on phase constituent of Mg–Zn–Zr–Y alloys. *Transactions of Nonferrous Metals Society of China*. 2011; 21 (4): 795–800.
[https://doi.org/10.1016/S1003-6326\(11\)60783-8](https://doi.org/10.1016/S1003-6326(11)60783-8)
 19. Xu D.K., Tang W.N., Liu L., Xu Y.B., Han E.H. Effect of W-phase on the mechanical properties of as-cast Mg–Zn–Y–Zr alloys. *Journal of Alloys and Compounds*. 2008; 461 (1–2): 248–252.
<https://doi.org/10.1016/j.jallcom.2007.07.096>
 20. Xu D.K., Tang W.N., Liu L., Xu Y.B., Han E.H. Effect of Y concentration on the microstructure and mechanical properties of as-cast Mg–Zn–Y–Zr alloys. *Journal of Alloys and Compounds*. 2007; 432 (1–2): 129–134.
<https://doi.org/10.1016/j.jallcom.2006.05.123>
 21. Bazhenov V.E., Saidov S.S., Tselovalnik Yu.V., Voropaeva O.O., Plisetskaya I.V., Tokar A.A., Bazlov A.I., Bautin V.A., Komissarov A.A., Koltygin A.V., Belov V.D. Comparison of castability, mechanical, and corrosion properties of Mg–Zn–Y–Zr alloys containing LPSO and W phases. *Transactions of Nonferrous Metals Society of China*. 2021; 31 (5): 1276–1290.
[https://doi.org/10.1016/S1003-6326\(21\)65577-2](https://doi.org/10.1016/S1003-6326(21)65577-2)
 22. Andersson J.O., Helander T., Huglund L., Shi P.F., Sundman B. Thermo-Calc and DICTRA, computational tools for materials science. *CALPHAD*. 2002; 26 (2): 273–312.
[https://doi.org/10.1016/S0364-5916\(02\)00037-8](https://doi.org/10.1016/S0364-5916(02)00037-8)
 23. Thermo-Calc software TCMG4: TCS Mg-based alloys database version 4 (accessed: 01.03.2022).
 24. Bazhenov V.E., Koltygin A.V., Sung M.C., Park S.H., Tselovalnik Y.V., Stepashkin A.A., Rizhskii A.A., Belov M.V., Belov V.D., Malyutin K.V. Development of Mg–Zn–Y–Zr casting magnesium alloy with high thermal conductivity. *Journal of Magnesium and Alloys*. 2021; 9 (5): 1567–1577.
<https://doi.org/10.1016/j.jma.2020.11.020>
 25. Kirkland N.T., Birbilis N., Staiger M.P. Assessing the corrosion of biodegradable magnesium implants: a critical review of current methodologies and their limitations. *Acta Biomaterialia*. 2012; 8 (3): 925–936.
<https://doi.org/10.1016/j.actbio.2011.11.014>
 26. ASTM Standard G1-03. Standard practice for preparing, cleaning, and evaluating corrosion test specimens. West Conshohocken: ASTM International, 2011.
 27. ASTM Standard G102-89, Standard practice for calculation of corrosion rates and related information from electrochemical measurements. West Conshohocken: ASTM International, 2015.
 28. Bazhenov V.E., Pikunov M.V., Safronova A.A., Tselovalnik Yu.V. Hot-tearing susceptibility of Al–Zn alloys. *Russian Metallurgy (Metally)*. 2017; 2017: 711–717.
<https://doi.org/10.1134/S0036029517090026>
 - Баженов В.Е., Пикун М.В., Сафронова А.А., Целовальник Ю.В. Исследование горячеломкости сплавов системы Al–Zn. *Металлы*. 2017; (5): 37–44.
 29. Bazhenov V.E., Koltygin A.V., Titov A.Yu., Belov V.D., Pavlinich S.P. Influence of ignition inhibitors on the strength of resin bonded sand molds and the composition of the oxide film on the surface of ML19 alloy castings. *Liteinoe proizvodstvo*. 2019; (5): 8–14. (In Russ.).
Баженов В.Е., Колтыгин А.В., Титов А.Ю., Белов В.Д., Павлинич С.П. Влияние ингибиторов горения на прочность форм из ХТС и состав оксидной пленки на поверхности отливок из сплава МЛ19. *Литейное производство*. 2019; (5): 8–14.
 30. Koltygin A.V., Bazhenov V.E. Structure and properties of ML10 (NZ30K) magnesium alloy, used as a raw material for the castings production. *Tsvetnye metally*. 2017; (7): 68–72. (In Russ.).
Колтыгин А.В., Баженов В.Е. Структура и свойства магниевых сплавов МЛ10 (NZ30K), используемого в качестве шихты для производства отливок. *Цветные металлы*. 2017; (7): 68–72.
<https://doi.org/10.17580/tsm.2017.07.11>
 31. Bazhenov V.E., Sannikov A.V., Saidov S.S., Rizhskii A.A., Koltygin A.V., Belov V.D., Yudin V.A. Influence of the alloying elements content and cooling rate on the corrosion resistance of the ML10 alloy. *Liteinoe proizvodstvo*. 2020; (12): 13–18. (In Russ.).
Баженов В.Е., Санников А.В., Саидов С.С., Рижский А.А., Колтыгин А.В., Белов В.Д., Юдин В.А. Влияние содержания легирующих элементов и скорости охлаждения на коррозионную стойкость сплава МЛ10.

- рости охлаждения на коррозионную стойкость сплава МЛ10. *Литейное производство*. 2020; (12): 13–18.
32. Bazhenov V.E., Koltygin A.V., Sung M.C., Park S.H., Titov A.Yu., Bautin V.A., Matveev S.V., Belov M.V., Belov V.D., Malyutin K.V. Design of Mg–Zn–Si–Ca casting magnesium alloy with high thermal conductivity. *Journal of Magnesium and Alloys*. 2020; 8 (1): 184–191.
<https://doi.org/10.1016/j.jma.2019.11.008>
33. Li C.Q., Xu D.K., Zeng Z.R., Wang B.J., Sheng L.Y., Chen X.B., Han E.H. Effect of volume fraction of LPSO phases on corrosion and mechanical properties of Mg–Zn–Y alloys. *Materials and Design*. 2017; 121: 430–441.
<https://doi.org/10.1016/j.matdes.2017.02.078>
34. StJohn D.H., Qian M., Easton M.A., Cao P., Hildebrand Z. Grain refinement of magnesium alloys. *Metallurgical and Materials Transactions A*. 2005; 36: 1669–1679.
<https://doi.org/10.1007/s11661-005-0030-6>
35. Jiang D.T., Mukherjee A.K. Spark plasma sintering of an infrared-transparent Y₂O₃–MgO nanocomposite. *Journal of the American Ceramic Society*. 2010; 93 (3): 769–773.
<https://doi.org/10.1111/j.1551-2916.2009.03444.x>

Information about the authors

Vyacheslav E. Bazhenov – Cand. Sci. (Eng.), Assistant Prof., Department of Foundry Technologies and Material Art Working (FT&MAW), National University of Science and Technology “MISIS” (NUST MISIS).
<https://orcid.org/0000-0003-3214-1935>
E-mail: V.E.Bazhenov@gmail.com

Ivan I. Baranov – Educat. Master, Department of FT&MAW, NUST MISIS.
<https://orcid.org/0000-0002-0465-7865>
E-mail: baranov.wania@yandex.ru

Anastasiya A. Lyskovich – Lab. Assistant, Department of FT&MAW, NUST MISIS.
<https://orcid.org/0000-0002-8490-4829>
E-mail: nastya719ls999@gmail.com

Andrei V. Koltygin – Cand. Sci. (Eng.), Assistant Prof., Department of FT&MAW, NUST MISIS.
<https://orcid.org/0000-0002-8376-0480>
E-mail: misistlp@mail.com

Andrei V. Sannikov – Cand. Sci. (Eng.), Assistant Prof., Department of FT&MAW, NUST MISIS.
<https://orcid.org/0000-0002-0517-7732>
E-mail: sannikov@ic-ltm.ru

Karen A. Kyaramyan – Head of Department of the Branch of Joint Stock Company “United Engine Corporation” “Research Institute of Technology and Organization of Engine Production” (JSC “UEC” “NIID”).
E-mail: k.kyaramyan@uecrus.com

Vladimir D. Belov – Dr. Sci. (Eng.), Head of Department of FT&MAW, NUST MISIS.
<https://orcid.org/0000-0003-3607-8144>
E-mail: vdbelov@mail.ru

Sergei P. Pavlinich – Dr. Sci. (Eng.), Director of the Branch of JSC “UEC” “NIID”.
E-mail: Pavlinich@uecrus.com

Информация об авторах

Вячеслав Евгеньевич Баженов – к.т.н., доцент кафедры литейных технологий и художественной обработки материалов (ЛТиХОМ) Национального исследовательского технологического университета «МИСИС» (НИТУ МИСИС).
<https://orcid.org/0000-0003-3214-1935>
E-mail: V.E.Bazhenov@gmail.com

Иван Ильич Баранов – учебный мастер кафедры ЛТиХОМ, НИТУ МИСИС.
<https://orcid.org/0000-0002-0465-7865>
E-mail: baranov.wania@yandex.ru

Анастасия Андреевна Лыскович – исследователь-лаборант кафедры ЛТиХОМ, НИТУ МИСИС.
<https://orcid.org/0000-0002-8490-4829>
E-mail: nastya719ls999@gmail.com

Андрей Вадимович Колтыгин – к.т.н., доцент кафедры ЛТиХОМ, НИТУ МИСИС.
<https://orcid.org/0000-0002-8376-0480>
E-mail: misistlp@mail.ru

Андрей Владимирович Санников – к.т.н., доцент кафедры ЛТиХОМ, НИТУ МИСИС.
<https://orcid.org/0000-0002-0517-7732>
E-mail: sannikov@ic-ltm.ru

Карен Абовович Кярамян – начальник отдела филиала АО «ОДК» «НИИД».
E-mail: k.kyaramyan@uecrus.com

Владимир Дмитриевич Белов – д.т.н., заведующий кафедрой ЛТиХОМ, НИТУ МИСИС.
<https://orcid.org/0000-0003-3607-8144>
E-mail: vdbelov@mail.ru

Сергей Петрович Павлинич – д.т.н., директор филиала АО «ОДК» «НИИД».
E-mail: Pavlinich@uecrus.com

Contribution of the authors

V.E. Bazhenov – conceptualization, analysis of the experimental results, writing of the manuscript.

I.I. Baranov – realization of experiment, analysis of the experimental results.

A.A. Lyskovich – realization of experiment, analysis of the experimental results.

A.V. Kolygin – scientific guidance, review and editing of the manuscript.

A.V. Sannikov – realization of experiment, analysis of the experimental results.

K.A. Kyaramyan – formulation of the aims and objectives of the study, provision of resources.

V.D. Belov – supervision, review and editing of the manuscript.

S.P. Pavlinich – supervision, review and editing of the manuscript.

Вклад авторов

В.Е. Баженов – формирование основной концепции, обработка результатов исследований, написание текста статьи.

И.И. Баранов – проведение экспериментов, обработка результатов исследований.

А.А. Лыскович – проведение экспериментов, обработка результатов исследований.

А.В. Колтыгин – научное руководство, редактирование текста статьи.

А.В. Санников – проведение экспериментов, обработка результатов исследований.

К.А. Карамян – формулировка цели и задачи исследования, обеспечение ресурсами.

В.Д. Белов – общее руководство, редактирование текста статьи.

С.П. Павлинич – общее руководство, редактирование текста статьи.

The article was submitted 18.05.2022, revised 22.08.2022, accepted for publication 24.08.2022

Статья поступила в редакцию 18.05.2022, доработана 22.08.2022, подписана в печать 24.08.2022

UDC 669.017.16

<https://doi.org/10.17073/0021-3438-2023-1-56-65>

Research article

Научная статья



Effect of hafnium on cast microstructure in alloy 1570

I.A. Zorin¹, E.V. Aryshensky¹, A.M. Drits¹, S.V. Konovalov¹, V.S. Komarov²

¹ Samara National Research University

34 Moskovskoe highway, Samara, 443086, Russia

² National University of Science and Technology “MISIS”

4 Leninskiy pr., Moscow, 119049, Russia

✉ Evgenii V. Aryshenskii (ar-evgenii@yandex.ru)

Abstract: The issue is devoted to the study of the influence of hafnium on the structure and properties of alloy 1570. Ingots from alloy 1570 were cast into the steel coquille, including those with additives of hafnium 0.1, 0.2 and 0.5 %. To determine the size of the grain structure in the obtained ingots, an Axionvert-40 MAT optical microscope was used, chemical analysis of intermetallic particles was carried out using JEOL 6390A SEM. In addition, for the alloy 1570 and 1570–0.5Hf, the presence of nanoparticles with the L₁₂ structure was studied using transmission electron microscope JEM-2100. Studies showed that hafnium additives make it possible to achieve a significant modification of the cast structure. For example, when introducing hafnium into the initial alloy in an amount of 0.5 % of the total weight, it was possible to achieve a reduction in the average grain size by 2 times. Scanning microscopy data showed that hafnium partially dissolves in particles containing scandium and zirconium as well. The addition of hafnium increases the number of large particles formed during crystallization. Transmission microscopy showed the presence of coherent aluminum matrix nanoparticles in alloy 1570 and having a superstructure of L₁₂, which were most likely formed during intermittent decay during ingot cooling. When 0.5 % Hf was added, no nanoparticles with the L₁₂ superstructure were detected. To explain the latter fact, it is necessary to study the surface of the liquidus of the Al–Hf–Sc system, as well as to study the effect of hafnium on the diffusion coefficient of scandium in aluminum.

Keywords: aluminum alloys, alloying with small additives of transition elements, microstructure, intermetallides

Funding: This study was supported by Russian Science Foundation Grant No. 22-29-01506, <https://rscf.ru/project/22-29-01506/>

For citation: Zorin I.A., Aryshensky E.V., Drits A.M., Konovalov S.V., Komarov V.S. Effect of hafnium on cast microstructure in alloy 1570. *Izvestiya. Non-Ferrous Metallurgy*. 2023; 29 (1): 56–65. (In Russ.). <https://doi.org/10.17073/0021-3438-2023-1-56-65>

Влияние гафния на литую микроструктуру в сплаве 1570

И.А. Зорин¹, Е.В. Арышенский¹, А.М. Дриц¹, С.В. Коновалов¹, В.С. Комаров²

¹ Самарский национальный исследовательский университет им. акад. С.П. Королева

443086, Россия, г. Самара, Московское шоссе, 34

² Национальный исследовательский технологический университет «МИСИС»

119049, Россия, г. Москва, Ленинский пр-т, 4

✉ Евгений Владимирович Арышенский (ar-evgenii@yandex.ru)

Аннотация: Изучено влияние гафния на структуру и свойства сплава 1570. В стальной кокиль были отлиты слитки из сплава 1570, в том числе с добавками гафния (0,1, 0,2 и 0,5 %). Для определения размеров зеренной структуры в полученных слитках приме-

нялся оптический микроскоп «Axiovert-40 MAT», химический анализ интерметаллидных частиц проводился с помощью сканирующего электронного микроскопа JEOL 6390A. Кроме того, для сплавов 1570 и 1570–0,5Hf на просвечивающем электронном микроскопе JEM-2100 изучалось наличие наночастиц, имеющих структуру L_{12} . Исследования показали, что добавки гафния позволяют добиться существенной модификации литой структуры. Например, при введении в исходный сплав 0,5 % Hf (от общей массы) достигнуто уменьшение среднего размера зерна в 2 раза. Согласно данным сканирующей микроскопии, гафний частично растворяется в частицах, содержащих также скандий и цирконий. Добавка гафния увеличивает количество крупных частиц, образующихся при кристаллизации. Просвечивающая микроскопия показала наличие в сплаве 1570 наночастиц, когерентных алюминиевой матрице и имеющих сверхструктуру L_{12} , которые с большой долей вероятности образовались в ходе прерывистого распада при остывании слитков. При добавке 0,5 % Hf наночастиц, имеющих сверхструктуру L_{12} , не обнаружено. Для объяснения этого факта необходимы исследования поверхности ликвидуса системы Al–Hf–Sc, а также изучение влияния гафния на коэффициент диффузии скандия в алюминии.

Ключевые слова: алюминиевые сплавы, легирование малыми добавками переходных элементов, микроструктура, интерметаллиды

Финансирование: Исследование выполнено за счет гранта Российского научного фонда № 22-29-01506, <https://rscf.ru/project/22-29-01506/>

Для цитирования: Зорин И.А., Арышенский Е.В., Дриц А.М., Коновалов С.В., Комаров В.С. Влияние гафния на литую микроструктуру в сплаве 1570. *Известия вузов. Цветная металлургия*. 2023; 29 (1): 56–65. <https://doi.org/10.17073/0021-3438-2023-1-56-65>

Introduction

Aluminum alloys are widely used and largely indispensable in aircraft, rocket and space equipment. Therefore, much research is being done to develop new and improve existing Al alloys [1–6].

One way to improve the performance properties of aluminum alloys is to add small amounts of scandium, the strongest modifier of cast aluminum structure. Furthermore, Sc additions lead to the formation of hardening Al_3Sc nanoparticles when properly cast and heat treated [7].

As a rule, scandium is used together with zirconium, which makes it possible to significantly reduce the amount of Sc required for the cast structure. Moreover, zirconium partially replaces scandium in Al_3Sc particles by forming a shell around them [8], which slows down the coagulation of the particles and increases their thermal stability due to the diffusion coefficient, which is lower for zirconium than for scandium [9].

Aluminum alloys with high magnesium content are the most popular for Sc–Zr alloys because they cause significant solid state hardening [10]. One of the most sought-after alloys of this group is alloy 1570 [6].

Further improvement of the properties of alloy 1570 is possible by the introduction of small additions of hafnium, which, first, is also a strong modifier of the cast structure [11] and, second, like zirconium, partially replaces scandium in the Al_3Sc particles and forms a shell that increases their thermal stability [9]. However, in order to address the question of the relevance of the use of hafnium in this alloy, it is necessary to study its effects on the microstructure of

the alloy both in the as-cast state and after heat treatment. Previously, this issue has not been considered anywhere.

The purpose of this study is to investigate the effects of hafnium on the microstructure of alloy 1570 as cast.

Methods

The samples of the model alloys were prepared under laboratory conditions in the induction furnace UI-25P with an input frequency of 50–60 Hz and an output frequency of 1–20 kHz. The 20×40×400 mm ingots were cast in a water-cooled steel mold at melting temperatures of 720–740 °C. The table shows the chemical composition of all alloys studied.

The following materials were used as furnace charge for the alloy: Aluminum (purity 99.8 %), magnesium (99.9 %), master alloy Al–2%Sc, silumin Al–12%Si, master alloy Al–5%Zr.

The grain structure of the samples was examined using an Axiovert-40 optical microscope MAT (Carl Zeiss, Germany). The average grain size was measured for each sample using the secant method (GOST 21073.2).

Intermetallic particles were examined using a scanning electron microscope SEM JEOL 6390A (Japan). The chemical composition of the structural components was studied by the method of energy dispersive spectroscopy using an X-Max 80T detector (Oxford Instruments, United Kingdom) in the energy range of 0–10 keV (the energy resolution of the detector is 122 eV). The microstructure of the 1570 and 1570–0.5Hf al-

Investigated alloys chemical composition, %

Химический состав исследуемых сплавов, %

Alloy	Al	Si	Fe	Mn	Mg	Ti	Zr	Sc	Hf
1570	Basis	0.17	0.27	0.44	6.16	0.03	0.05	0.22	–
1570–0.1Hf	Basis	0.17	0.27	0.44	6.16	0.03	0.05	0.22	0.1
1570–0.2Hf	Basis	0.17	0.27	0.44	6.16	0.03	0.05	0.22	0.2
1570–0.5Hf	Basis	0.17	0.27	0.44	6.16	0.03	0.05	0.22	0.5

loys was further investigated using a JEM-2100 transmission electron microscope (JEOL, Japan) at 200 kV. Elemental analysis was performed using an energy dispersive X-ray spectrometer INCA x-sight (Oxford Instruments, UK).

Results and discussion

Fig. 1 shows the alloy 1570 microstructure with joint scandium-zirconium alloying. This alloy shows equiaxed

grain with average size of 44 μm. This is 6 times less than, for example, the high-magnesium alloy 5182 without scandium and zirconium additions [12]. In general, the data obtained correspond to those in [13], where with the joint addition of scandium (0.25 %) and zirconium (0.15 %) to the 1970 alloy, the grain is refined 8.5 times.

With increasing hafnium content, the grain size gradually decreases. With the addition of 0.1 % Hf, the average size of the grain structure decreases to 34 μm.

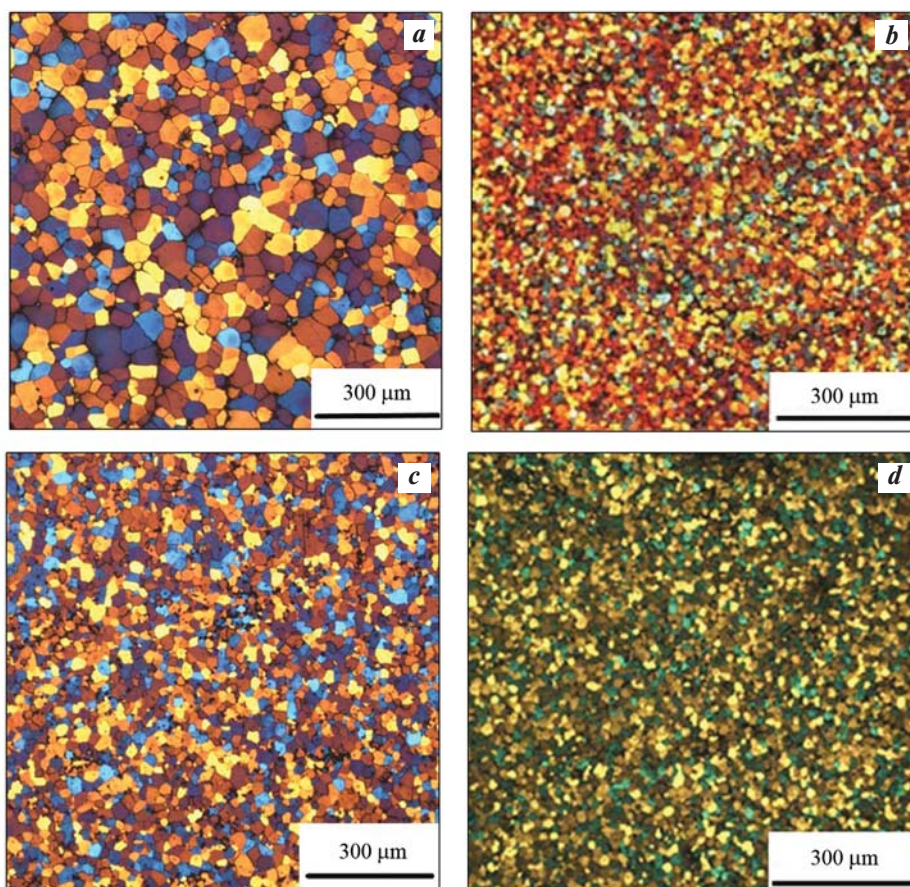


Fig. 1. Cast alloy microstructure
a – 1570; *b* – 1570–0.1Hf; *c* – 1570–0.2Hf; *d* – 1570–0.5Hf

Рис. 1. Микроструктура литого сплава
a – 1570; *b* – 1570–0,1Hf; *c* – 1570–0,2Hf; *d* – 1570–0,5Hf

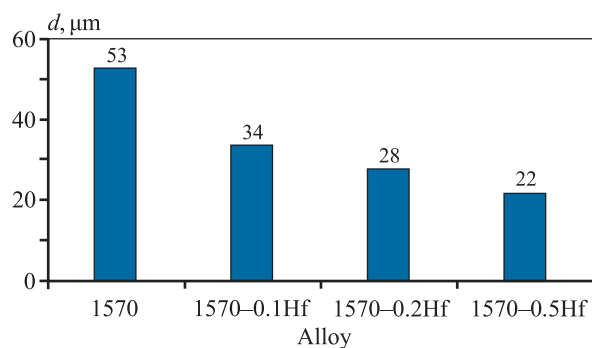


Fig. 2. The cast samples average grain size

Рис. 2. Средний размер зерна литых образцов

Further increasing the hafnium content to 0.2 and 0.5 % modifies the grain structure to 28 and 22 μm respectively (see Fig. 2).

In order to explain the influence of hafnium on the refinement of the cast grain structure, it should be noted that, according to the Al–Hf state diagram, primary Al_3Hf intermetallics form in the liquid phase at an Hf content of 0.43 % [14]. However, due to non-equilibrium crystallization conditions, primary intermetallic compounds can occur even at an Hf concentration of 0.2 % [11]. In addition, hafnium promotes refinement of the grain structure by reducing the surface tension between the solid and liquid phases, thus facilitating nucleation in the latter [11]. The grain refinement caused by the addition of 0.1 and 0.2 % hafnium can therefore be explained by the reduction in surface tension. A further reduction in grain size with the addition of 0.5 % Hf is due to the appearance of primary Al_3Hf particles.

There may be another explanation for the modifying effect of hafnium when introduced into alloy 1570. Hafnium may have similar effects to zirconium on scandium. Some researchers believe that zirconium reduces the amount of scandium required to reach the proeutectic concentration and initiate the formation of the primary Al_3Sc particles. In this way, according to them, the effectiveness of the joint scandium-zirconium alloy on the change of the cast structure can be explained [15]. The authors of the study [16] show that the common alloying with zirconium and scandium, even at low content of these elements, contributes to the occurrence of primary intermetallic compounds in aluminum alloys. According to the liquidus surface of the Al–Sc–Zr system calculated in [16], the liquid phase starts to crystallize already at low scandium and zirconium concentrations in $\text{Al}_{75}\text{Sc}_{16}\text{Zr}_9$. At scandium and zirconium concentrations typical of alloy 1570, the liquidus surface predicts liquid crystallization into the primary intermetallic phase Al_2Sc , which resolves Zr well. Apparently, the

occurrence of primary Al_2Sc contributes to the change in grain structure. Hafnium may have a similar effect. However, there are currently no data on the Al–Hf–Sc liquidus surface, making it impossible to confirm this hypothesis.

It should be noted that the EDS analysis can only determine the chemical composition of the intermetallic particles with some accuracy, but unlike the X-ray phase analysis, it cannot identify them unambiguously. It is only possible to correlate their chemical composition with the composition of the particles described in the literature, which was done in this study.

Particles containing aluminum, silicon and iron were found in both alloy 1570 and alloy 1570–0.5Hf. In their chemical composition, these intermetallics (2 and 7 in Fig. 3, a, b) are close to $\text{Al}_3(\text{Fe},\text{Si})$ (Fig. 3, c, d) [17]. These and similar intermetallic particles are often found in aluminum alloys, since Fe and Si are always present as unavoidable impurities.

The second type of particles found in the study are intermetallic particles containing aluminum and magnesium (4 in Fig. 3, b, c). Some intermetallics also contain silicon in addition to the above-mentioned elements (3 and 6 in Fig. 3). The second type of particles is close in chemical composition to the β -phase (Al_3Mg_2), which is very common in high-magnesium aluminum alloys [10, 18, 19], and the third type — the Mg_2Si phase, which is also commonly found in this type of alloys [18, 19]. The presence of aluminum in the particles near Mg_2Si can be explained by the fact that the study with the EDS analysis necessarily captures some of the solid solution.

Another type of particles discovered during the study are particles similar in chemical composition and morphology (diamond-shaped) to the primary Al_3Sc particles (1 and 5 in Fig. 3) [20, 21]. However, in addition to scandium, they also contain zirconium in alloy 1570 and zirconium and hafnium in alloy 1570–0.5Hf. It should be noted that zirconium and hafnium dissolve in the Al_3Sc phase by 35 and 36 %, respectively [13, 22]. This explains the presence of particles with the combined presence of scandium, zirconium, and hafnium.

When interpreting the transmission microscopy results it should be taken into account that Al has a face-centered cubic unit cell, and Al_3Sc has a primitive cubic unit cell. The primitive lattice will resolve all reflections. According to the energy dispersion microscopy results, we can see the co-directionality of the inverse lattice vectors ($\langle 001 \rangle$, $\langle 110 \rangle$) for Al_3Sc and Al. Al_3Sc and Al also have lattice parameters close to each other, and therefore the resolved reflections for both phases, such as the reflections of surfaces $\{111\}$,

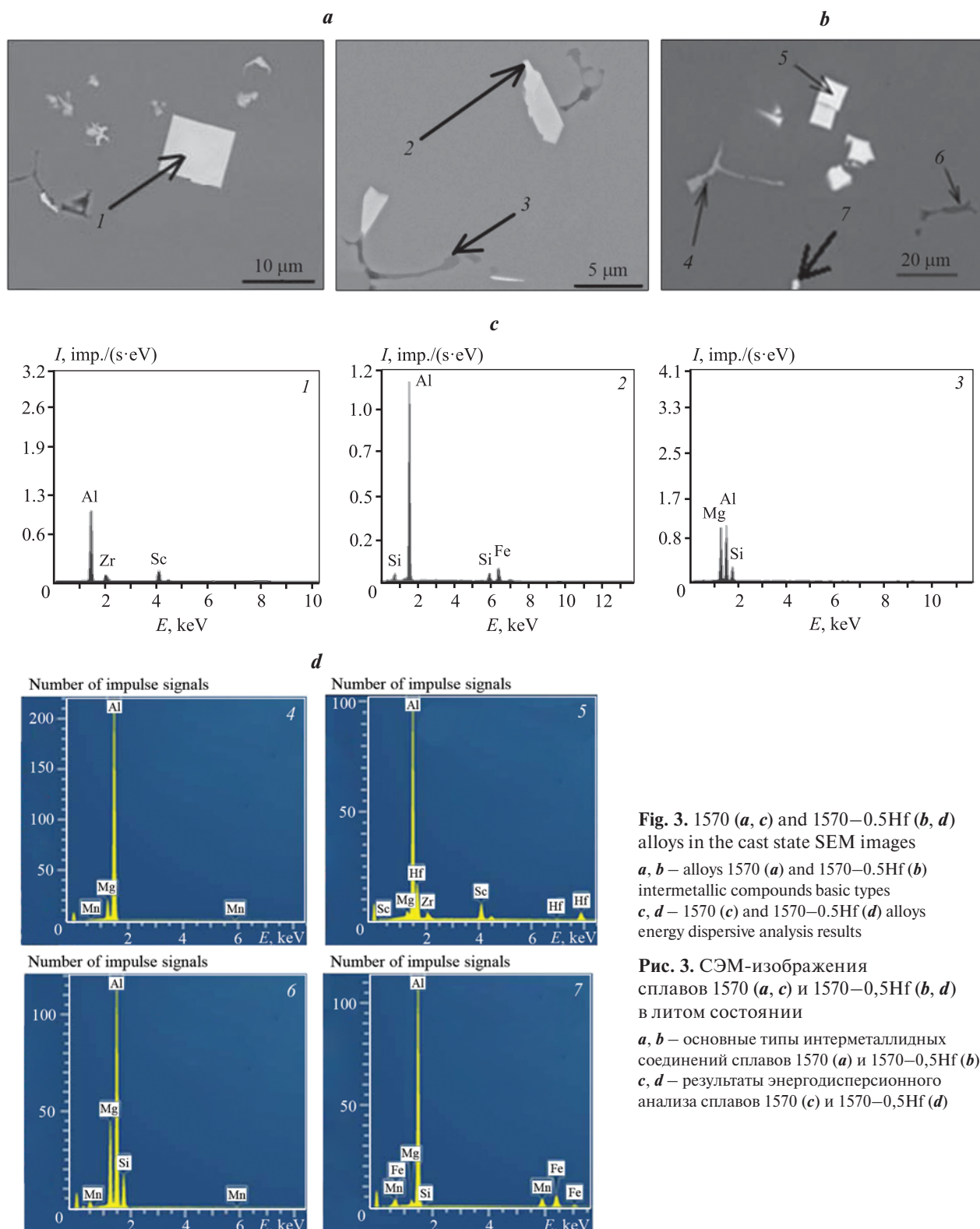


Fig. 3. 1570 (*a, c*) and 1570–0.5Hf (*b, d*) alloys in the cast state SEM images *a, b* – alloys 1570 (*a*) and 1570–0.5Hf (*b*) intermetallic compounds basic types *c, d* – 1570 (*c*) and 1570–0.5Hf (*d*) alloys energy dispersive analysis results

Рис. 3. СЭМ-изображения сплавов 1570 (*a, c*) и 1570–0,5Hf (*b, d*) в литом состоянии *a, b* – основные типы интерметаллидных соединений сплавов 1570 (*a*) и 1570–0,5Hf (*b*) *c, d* – результаты энергодисперсионного анализа сплавов 1570 (*c*) и 1570–0,5Hf (*d*)

agree. Fig. 4, *a* shows three images of microdiffraction in the dark field, where the directions on the zone axis for Al_3Sc and Al coincide. From the above, it can be concluded that the Al_3Sc lattice is coherent with the aluminum matrix. In addition, the presence of $\{110\}$

type reflexes confirms that Al_3Sc particles have an L12 structure [23, 24]. The average size of the detected nanoparticles was 7–10 nm (Fig. 4, *a*), the results of energy dispersive analysis showed the presence of scandium in them (Fig. 5). As for the 1570–0.5Hf al-

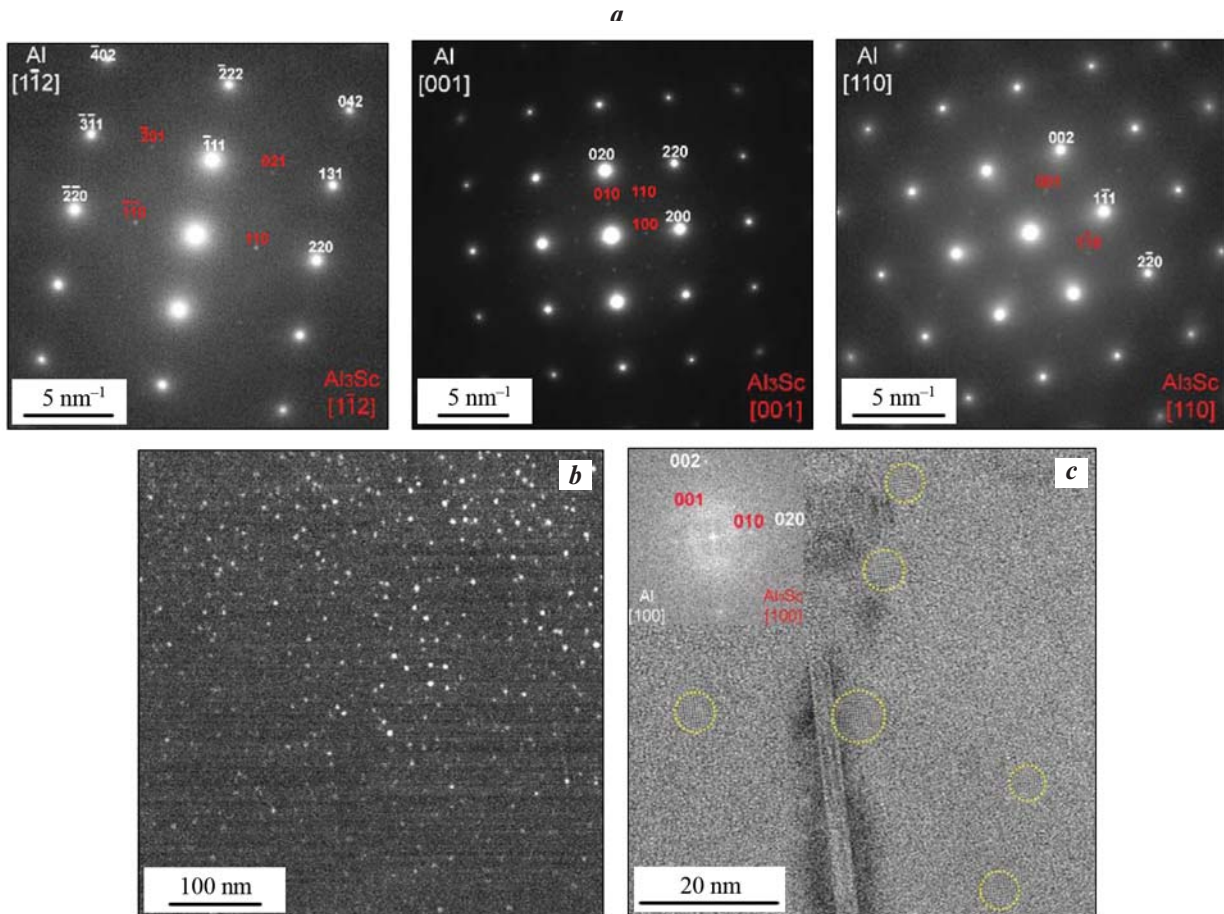


Fig. 4. Selected area diffraction pattern of 1570 alloy
a – axes [112], [001] and [110] microelectronograms; *b, c* – coherent nanoparticles

Рис. 4. Электронно-микроскопические изображения микроструктуры сплава 1570
a – микроэлектронogramмы осей [112], [001] и [110]; *b, c* – когерентные наночастицы

loy, no particles with reflexes from L_{12} superstructures were detected.

Before proceeding to the explanation of the nature and origin of the Al_3Sc particles, it should be noted that when casting aluminum alloys with small additions of scandium, attempts are made to fix the scandium in solid solution due to the rapid cooling of the cast billet in the region of the crystallization temperature [25]. However, due to the high diffusion rate of scandium in aluminum during the subsequent cooling of the ingot, scandium is released in most cases by the intermittent decomposition of the supersaturated solid solution in the form of semi-coherent and coherent particles [20, 21]. Although such particles improve mechanical properties, their efficiency is much lower than that of those produced by continuous decomposition [15]. Moreover, intermittent decomposition of the supersaturated solid solution during cooling of the cast bolt leads to the release of large amounts of scandium, which reduces the number of

Al_3Sc -type nanoparticles formed during further heat treatment [26]. Therefore, based on the literature data and taking into account the coherence of these particles, the presence of scandium in them and the superstructure L_{12} , we can say with high probability that they are close to the intermetallic Al_3Sc .

The absence of reflections from superstructure L_{12} in the alloy with the addition of 0.5 % Hf most likely means that the supersaturated solid solution is significantly lacking in scandium, so that no discontinuous decomposition occurs. One explanation could be the possible effect of hafnium on reducing the proeutectic concentration of scandium mentioned above. When this effect occurs, it means that more primary Al_3Sc particles are formed and thus the scandium concentration in the supersaturated solid solution decreases. This is indirectly confirmed by the increase in the total number of large intermetallic particles (see Fig. 5). Another possible explanation is that hafnium slows the diffusion of scandi-

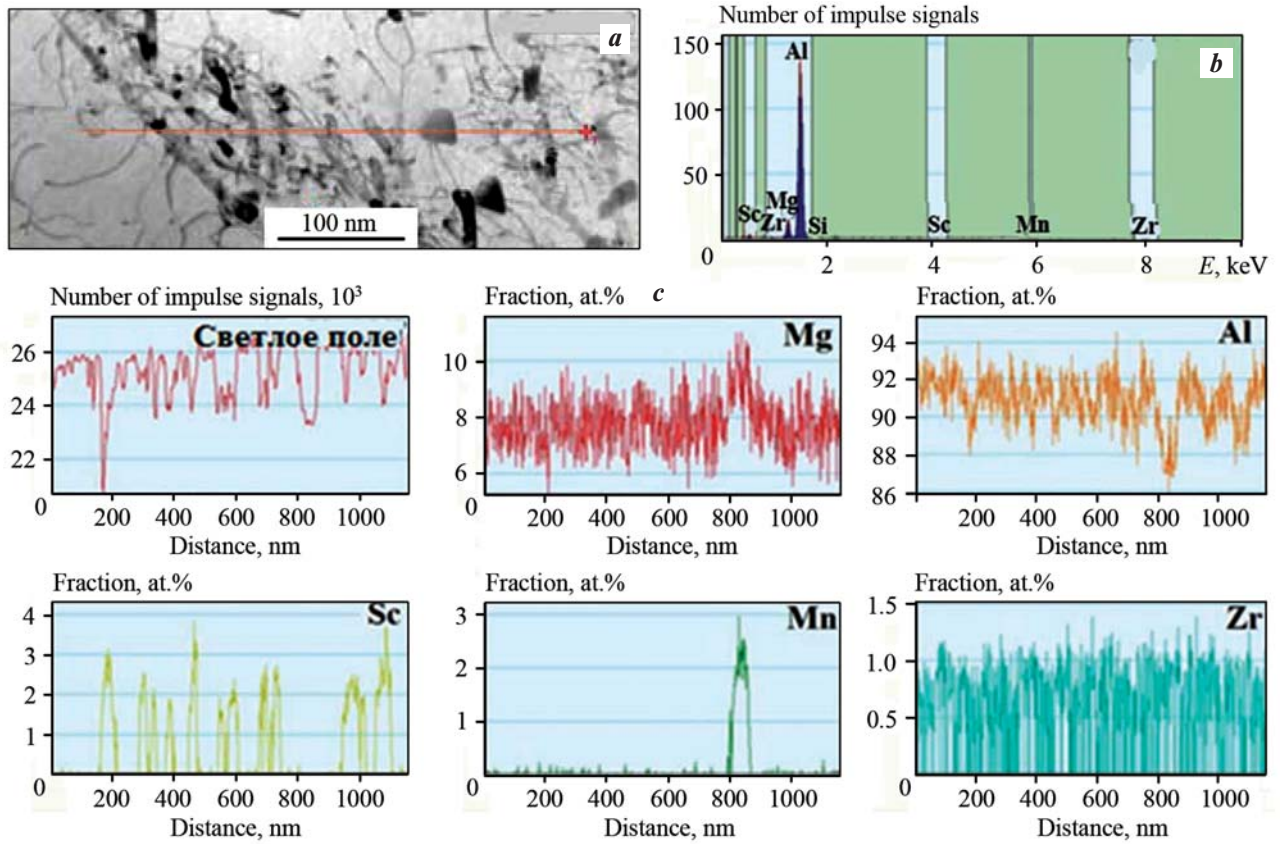


Fig. 5. Alloy 1570 energy dispersive X-ray spectroscopy
a – investigated microstructure bright-field image; *b* – energy dispersive spectral profile (EDS); *c* – scanning line (EDS) elements distribution

Рис. 5. Энергодисперсионная рентгеновская спектроскопия сплава 1570
a – светлопольное изображение исследуемой микроструктуры; *b* – энергодисперсионный спектральный профиль (EDS);
c – распределение элементов по линии сканирования (EDS)

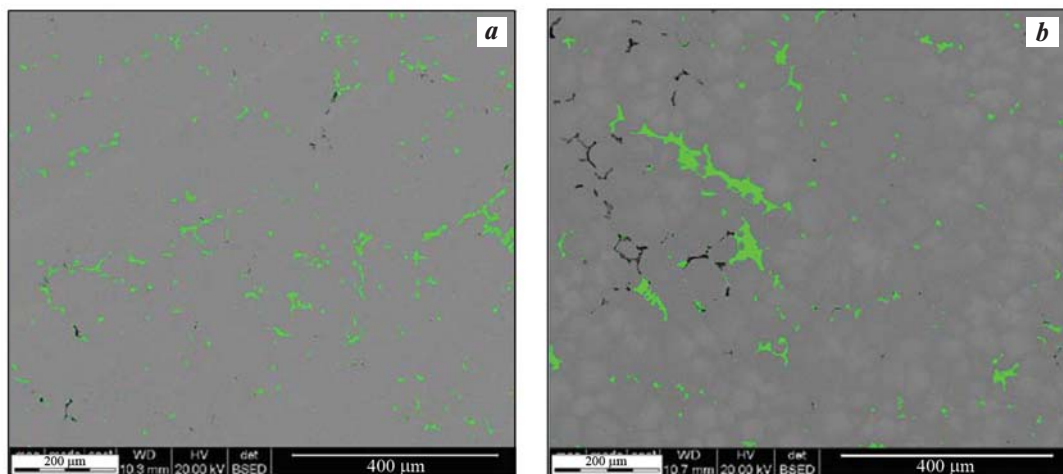


Fig. 6. 1570 (*a*) and 1570–0.5Hf (*b*) alloys intermetallic particles appearance
Рис. 6. Внешний вид интерметаллидных частиц в сплавах 1570 (*a*) и 1570–0,5Hf (*b*)

um in the aluminum matrix, but there are no studies in the literature that address this question.

From the data obtained by scanning electron microscopy (Fig. 6), it can be concluded that the number of intermetallic particles deposited from the supersaturated solid solution increases when alloy 1570 is alloyed with hafnium.

Conclusion

Hafnium additives allow to increase the efficiency of milling grain by 2 times. The main explanation for this is the primary Al_3Hf particle modifying effect. According to the results of the study the chemical composition of the large intermetallic particles, it was found that hafnium is partially dissolved in intermetallic particles, which also contain zirconium and scandium. Transmission microscopy revealed a large number of coherent scandium-containing particles with superstructure L_{12} in alloy 1570, which were most likely formed by intermittent decomposition of the supersaturated solid solution. At addition of 0.5 % hafnium the fine-dispersed particles having L_{12} superstructure are absent — to explain this fact additional liquidus surface of Al—Hf—Sc system and hafnium influence on scandium diffusion coefficient investigations are required.

References

1. Savchenkov S., Kosov Y., Bazhin V., Krylov K., Kawalla R. Microstructural master alloys features of aluminium-erbium system. *Crystals*. 2021; 11 (11): 1353. <https://doi.org/10.3390/cryst11111353>
2. Belov N.A., Shurkin P.K., Korotkova N.O., Cherkasov S.O. The effect of heat treatment on the structure and mechanical properties of cold-rolled sheets made of Al—Cu—Mn alloys with varying copper to manganese ratios. *Tsetnye Metally*. 2021; (9): 80—86. (In Russ.). <https://doi.org/10.17580/tsm.2021.09.09>
Белов Н.А., Шуркин П.К., Короткова Н.О., Черкасов С.О. Влияние термообработки на структуру и механические свойства холоднокатанных листов сплавов системы Al—Cu—Mn с разным соотношением меди и марганца. *Цветные металлы*. 2021; (9): 80—86.
3. Akopyan T.K., Belov N.A., Letyagin N.V., Milovich F.O., Lukiyanchuk A.A., Fortuna A.S. Influence of indium trace addition on the microstructure and precipitation hardening response in Al—Si—Cu casting aluminium alloy. *Materials Science and Engineering A*. 2022; 831: 142329. <https://doi.org/10.1016/j.msea.2021.142329>
4. Bazhin V.Y., Alattar A.L., Danilov I.V. Development of technologies for the production of multicomponent ligatures Al—Cu—B—C with high thermal characteristics. *IOP Conference Series: Materials Science and Engineering*. 2019; 537 (2): 149243.
5. Du H., Zhang S., Zhang B., Belov N., Liu Z. Ca-modified Al—Mg—Sc alloy with high strength at elevated temperatures due to a hierarchical microstructure. *Journal of Materials Science*. 2021; 56 (28): 16145—16157.
6. Bronz A.V., Efremov V.I., Plotnikov A.D., Chernyavskii A.G. Alloy 1570C is a material for hermetic structures of promising reusable products of RSC «Energya». *Kosmicheskaya tekhnika i tekhnologii*. 2014; (4): 62—67. (In Russ.).
Бронз А.В., Ефремов В.И., Плотников А.Д., Чернявский А.Г. Сплав 1570C — материал для герметичных конструкций перспективных многоразовых изделий РКК «Энергия». *Космическая техника и технологии*. 2014; (4): 62—67.
7. Zakharov V.V. The effect of scandium on the structure and properties of aluminum alloys. *Metallovedenie i termicheskaya obrabotka metallov*. 2003; (7): 7—15. (In Russ.).
Захаров В.В. Влияние скандия на структуру и свойства алюминиевых сплавов. *Металловедение и термическая обработка металлов*. 2003; (7): 7—15.
8. Clouet E., Ludovic L., Thierry E., Williams L., Deschamps A. Complex precipitation pathways in multicomponent alloys. *Nature Materials*. 2006; 5 (6): 482—488. <https://doi.org/10.1038/nmat1652>
9. Hallem H., Marthinsen K., Lefebvre W., Danoix F., Forbord B. The formation of $\text{Al}_3(\text{Sc}_x\text{Zr}_y\text{Hf}_{1-x-y})$ -dispersoids in aluminium alloys. *Materials Science and Engineering*. 2006; 421 (1—2): 154—160.
10. Kolachev B.A., Elagin V.I., Livanov V.A. Metallurgy and heat treatment of non-ferrous metals and alloys. Moscow: MISIS, 2005. (In Russ.).
Колачев Б.А., Елагин В.И., Ливанов В.А. Металловедение и термическая обработка цветных металлов и сплавов. М.: МИСиС, 2005.
10. Li H-y, Li D-w, Zhu Z-x, Chen B-a, Xin C, Yang C-l, Zhang H-y, Kang W. Grain refinement mechanism of as-cast aluminum by hafnium. *Transactions of Nonferrous Metals Society of China*. 2016; 26 (12): 3059—3069. [https://doi.org/10.1016/S1003-6326\(16\)64438-2](https://doi.org/10.1016/S1003-6326(16)64438-2)
12. Yashin V., Aryshenskii E., Hirsch J., Kononov S., Latushkin I. Study of recrystallization kinetics in AA5182 aluminium alloy after deformation of the as-cast structure. *Materials Research Express*. 2019; 6: 066552. <https://doi.org/10.1088/2053-1591/ab085f>
13. Davydov V.G., Elagin V.I., Zakharov V.V., Rostova T.D. Alloying aluminum alloys with scandium and zirconium

- additives. *Metallovedenie i termicheskaya obrabotka metallov*. 1996; (8): 25–30. (In Russ.).
<https://doi.org/10.1007/bf01395323>
- Давыдов В.Г., Елагин В.И., Захаров В.В., Ростова Т.Д. О легировании алюминиевых сплавов добавками скандия и циркония. *Металловедение и термическая обработка металлов*. 1996; (8): 25–30.
14. Rokhlin L.L., Bochvar N.R., Dobatkina T.V., Leont'ev V.G. Al-rich portion of the Al–Hf phase diagram. *Russian Metallurgy (Metally)*. 2009; 3: 258–262.
<https://doi.org/10.1134/S003602950903012>
- Рохлин Л.Л., Бочвар Н.Р., Добаткина Т.В., Леонтьев В.Г. Исследование богатой алюминием части диаграммы состояния Al–Hf. *Металлы*. 2009; (3): 93–98.
15. Röyset J., Ryum N. Scandium in aluminium alloys. *International Materials Reviews*. 2005; 50 (1): 19–44.
16. Bo H., Liu L.B., Hu J.L., Jin Z.P. Experimental study and thermodynamic modeling of the Al–Sc–Zr system. *Computational Materials Science*. 2017; 133: 82–92.
<https://doi.org/10.1016/j.commatsci.2017.02.029>
17. Mondolfo L.F. Aluminium alloys: structure and properties. Elsevier, 1976.
 Мондольфо Л.Ф. Структура и свойства алюминиевых сплавов. М.: Металлургия, 1979.
18. Engler O., Kuhnke K., Hasenclever J. Development of intermetallic particles during solidification and homogenization of two AA 5xxx series Al–Mg alloys with different Mg contents. *Journal of Alloys and Compounds*. 2017; 728: 669–681.
<https://doi.org/10.1016/j.jallcom.2017.09.060>
19. Engler O., Simon M. Control of second-phase particles in the Al–Mg–Mn alloy AA 5083. *Journal of Alloys and Compounds*. 2016; 689: 998–1010.
<https://doi.org/10.1016/j.jallcom.2016.08.070>
20. Blake N., Hopkins M.A. Constitution and age hardening of Al–Sc alloys. *Journal of Materials Science*. 1985; 20: 2861–2867.
<https://doi.org/10.1007/BF00553049>
21. Norman A., Prangnell P., McEwen R. The solidification behavior of dilute aluminum–scandium alloys. *Acta Materialia*. 1998; 46: 5715–5732.
22. Rokhlin L.L., Bochvar N.R., Boselli J., Dobatkina T.V. Investigation of the phase relations in the Al-rich alloys of the Al–Sc–Hf system in solid state. *Journal of Phase Equilibria and Diffusion*. 2010; 31: 327–332.
<https://doi.org/10.1007/s11669-010-9710-z>
23. Harada Y., Dunand D.C. Creep properties of Al₃Sc and Al₃(Sc, X) intermetallics. *Acta Materialia*. 2000; 48 (13): 3477–3487.
[https://doi.org/10.1016/S1359-6454\(00\)00142-7](https://doi.org/10.1016/S1359-6454(00)00142-7)
24. Keith E., Knipling, David C., Dunand, David N. Precipitation evolution in Al–Zr and Al–Zr–Ti alloys during isothermal aging at 375–425 C. *Acta Materialia*. 2008; 56 (1): 114–127.
<https://doi.org/10.1016/j.actamat.2007.09.004>
25. Zakharov V.V., Elagin V.I., Rostova T.D., Filatov Yu.A. Metallurgical principles of alloying aluminum alloys with scandium. *Tekhnologiya legkikh spлавov*. 2010; (1): 67–73. (In Russ.).
 Захаров В.В., Елагин В.И., Ростова Т.Д., Филатов Ю.А. Металловедческие принципы легирования алюминиевых сплавов скандием. *Технология легких сплавов*. 2010; (1): 67–73.
26. Parker B.A., Zhou Z.F., Nolle P. The effect of small additions of scandium on the properties of aluminium alloys. *Journal of Materials Science*. 1995; 30 (2): 452–458.
<https://doi.org/10.1007/BF00354411>

Information about the authors

Igor' A. Zorin – Student, Laboratory Worker of the ONIL-4 of Samara National Research University.
<https://orcid.org/0000-0001-9349-2494>
 E-mail: zorin_20@mail.ru

Evgenii V. Aryshenskii – Cand. Sci. (Eng.), Associate Prof. of the Department “Materials Technology and Aviation Materials Science”, Senior Researcher of the ONIL-4 of Samara National Research University.
<https://orcid.org/0000-0003-3875-7749>
 E-mail: ar-evgenii@yandex.ru

Aleksandr M. Drita – Cand. Sci. (Eng.), Leading Researcher of the ONIL-4 of Samara National Research University.
<https://orcid.org/0000-0002-9468-8736>
 E-mail: alexander.drita@arconic.com

Информация об авторах

Игорь Александрович Зорин – студент, лаборант ОНИЛ-4 Самарского университета.
<https://orcid.org/0000-0001-9349-2494>
 E-mail: zorin_20@mail.ru

Евгений Владимирович Арышенский – к.т.н., доцент кафедры «Технология металлов и авиаматериаловедение» (ТМиАМ), старший научный сотрудник ОНИЛ-4 Самарского университета.
<https://orcid.org/0000-0003-3875-7749>
 E-mail: ar-evgenii@yandex.ru

Александр Михайлович Дриц – к.т.н., ведущий научный сотрудник ОНИЛ-4 Самарского университета.
<https://orcid.org/0000-0002-9468-8736>
 E-mail: alexander.drita@arconic.com

Sergei V. Konovalov – Dr. Sci. (Eng.), Prof., Chief Researcher of the ONIL-4, Head of the Department “Materials Technology and Aviation Materials Science” of Samara National Research University.

<https://orcid.org/0000-0003-4809-8660>

E-mail: konovserg@gmail.com

Viktor S. Komarov – Cand. Sci. (Eng.), Senior Researcher of the Laboratory of Ultrafine-Grained Metal Materials of National University of Science and Technology “MISIS”.

<https://orcid.org/0000-0003-4710-3739>

E-mail: kom1107@yandex.ru

Сергей Валерьевич Коновалов – д.т.н., профессор, заведующий кафедрой ТМиАМ, главный научный сотрудник ОНИЛ-4 Самарского университета.

<https://orcid.org/0000-0003-4809-8660>

E-mail: konovserg@gmail.com

Виктор Сергеевич Комаров – к.т.н., старший научный сотрудник лаборатории ультрамелкозернистых металлических материалов Национального исследовательского технологического университета «МИСИС».

<https://orcid.org/0000-0003-4710-3739>

E-mail: kom1107@yandex.ru

Contribution of the authors

I.A. Zorin – conducting experiments, writing the manuscript.

E.V. Aryshenskii – formation of the main concept, goal and objectives of the study, preparation of the text, formulation of the conclusions.

A.M. Drits – scientific guidance, correction of the text, correction of conclusions.

S.V. Konovalov – conducting research using a scanning electron microscope and processing these results.

V.S. Komarov – conducting research using a transmission electron microscope and processing these results.

Вклад авторов

И.А. Зорин – проведение экспериментов, подготовка текста статьи

Е.В. Арышенский – формирование основной концепции, постановка цели и задачи исследования, подготовка текста, формулировка выводов.

А.М. Дриц – научное руководство, корректировка текста, корректировка выводов.

С.В. Коновалов – проведение исследований с помощью сканирующего электронного микроскопа и обработка этих результатов.

В.С. Комаров – проведение исследований с помощью просвечивающего электронного микроскопа и обработка этих результатов.

The article was submitted 10.04.2022, revised 02.11.2022, accepted for publication 08.11.2022

Статья поступила в редакцию 10.04.2022, доработана 02.11.2022, подписана в печать 08.11.2022

UDC 669.2292'5 + 669.735 : 539.216.2

<https://doi.org/10.17073/0021-3438-2023-1-66-74>

Research article

Научная статья



V–Cd nanoparticle-formed alloys: fabrication, phase composition and structure

V.N. Volodin, Yu.Zh. Tuleushev, A.K. Kaliyeva,
E.A. Zhakanbayev, A.K. Mamyrbayev

Institute of Nuclear Physics, Ministry of Energy of Republic of Kazakhstan

1 Ibragimov str., Almaty, 050032, Republic of Kazakhstan

✉ Valerii N. Volodin (volodinv_n@mail.ru)

Abstract: The results of the study of targeted sputtering and deposition of ultrafine vanadium and cadmium particles on substrates that are not heated and shifted with respect to the substrate plasma currents are revealed. As a result of the conducted studies, coatings were obtained in the range with a concentration of cadmium from 9.6 to 88.6 at.%. The critical size of vanadium particles capable of forming alloys with cadmium is 0.6 nm. The concentration limit for the presence of solid solutions of cadmium in vanadium is the cadmium content of ~37 at.%, at a higher cadmium content the film coating is represented by a mixture of cadmium phases and a solid solution of cadmium in vanadium. The dependence of the lattice parameter of α -vanadium on the content of cadmium in it corresponds to the expression: a [nm] = $8 \cdot 10^{-4} C_{Cd} + 0.3707$, where C_{Cd} is the concentration of cadmium, at.%. On the surface of the sample in the region of solid solutions (31.6 at.% Cd), the presence of threadlike crystals of cadmium was found, the reason for the appearance of which is the lattice pressure of the matrix metal. Annealing of films rich in cadmium (69.5 at.%) in vacuum is accompanied by cracking of the coating and the formation of pores. The latter can be used as a method for obtaining porous vanadium.

Keywords: vanadium, cadmium, nanoparticles, alloy, solid solution, lattice parameter, coating, threadlike crystals

Funding: This work was supported financially by the Ministry of Education and Science of the Republic of Kazakhstan (grant BR10965191).

For citation: Volodin V.N., Tuleushev Yu.Zh., Kaliyeva A.K., Zhakanbayev E.A., Mamyrbayev A.K. V–Cd nanoparticle-formed alloys: fabrication, phase composition and structure. *Izvestiya. Non-Ferrous Metallurgy*. 2023; 29 (1): 66–74. (In Russ.).

<https://doi.org/10.17073/0021-3438-2023-1-66-74>

Сформированные наночастицами сплавы V–Cd: получение, фазовый состав и структура

В.Н. Володин, Ю.Ж. Тулеушев, А.К. Калиева,
Е.А. Жаканбаев, А.К. Мамырбаев

Институт ядерной физики Министерства энергетики Респ. Казахстан

050032, Респ. Казахстан, г. Алматы, ул. Ибрагимова, 1

✉ Валерий Николаевич Володин (volodinv_n@mail.ru)

Аннотация: Приведены результаты исследований распыления и осаждения ультрадисперсных частиц ванадия и кадмия на нагреваемые и перемещаемые относительно потоков плазмы подложки. Были получены покрытия в интервале концентраций

кадмия от 9,6 до 88,6 ат.%. Критическим размером частиц ванадия, способных к образованию сплавов с кадмием, определена величина 0,6 нм. Концентрационной границей существования твердых растворов кадмия в ванадии является содержание кадмия ~37 ат.%, при большей его доли пленочное покрытие представлено смесью фаз кадмия и твердого раствора кадмия в ванадии. Зависимость параметра решетки α -ванадия от содержания кадмия в нем соответствует следующему выражению: a [нм] = $8 \cdot 10^{-4} C_{Cd} + 0,3707$, где C_{Cd} – концентрация кадмия, ат.%. На поверхности образца в области твердых растворов (31,6 ат.% Cd) обнаружено наличие нитевидных кристаллов кадмия, причиной появления которых является решеточное давление матричного металла. Отжиг богатых по содержанию кадмия пленок (69,5 ат.%) в вакууме сопровождается растрескиванием покрытия и образованием пор. Последнее может быть использовано как метод получения пористого ванадия.

Ключевые слова: ванадий, кадмий, наночастицы, сплав, твердый раствор, параметр решетки, покрытие, нитевидные кристаллы

Финансирование: Работа выполнена при финансовой поддержке Министерства образования и науки Республики Казахстан (грант BR10965191).

Для цитирования: Володин В.Н., Тулеушев Ю.Ж., Калиева А.К., Жаканбаев Е.А., Мамырбаев А.К. Сформированные наночастицами сплавы V–Cd: получение, фазовый состав и структура. *Известия вузов. Цветная металлургия*. 2023; 29 (1): 66–74. <https://doi.org/10.17073/0021-3438-2023-1-66-74>

Introduction

To date, there is a problem of obtaining intermetal alloys with very large differences in physical properties, such as melting point, vapor pressure, density, crystal lattice type, etc. At the same time, the production of such alloys requires new properties and technologies to obtain potential materials with unusual properties. In our case, the choice of alloy is due to the fact that the distillation of the highly volatile cadmium from the V–Cd alloys allows the recovery of porous vanadium, which can be used as a catalyst or special filter in another technical field.

One of the ways to compensate for the differences in the properties of the metals, especially in their melting temperatures, in the production of solid solution alloys is to use the size factor. The significant decrease in melting temperature (from a few tens to hundreds of degrees) of various metal dispersion particles, with a simultaneous decrease in droplet size, has sparked the interest of researchers in this area of materials science. Here and now, numerous studies have been carried out on the influence of particle size on melting temperature [1–8], thermodynamics of small formations [9–13] and material structure, preparation of alloys at “room temperature”, synthesis of intermetallic compounds [14–16] and others. This research led to the introduction of the concept of “thermofluctional melting” to the scientific community. The latter means that a very small particle remains in a quasi-liquid state up to a certain critical size, beyond which it crystallizes.

The author of the paper [13], in his consideration of the thermodynamics of small systems, has noted some important points, in particular: for sufficiently small systems, the phase state and phase transitions are meaningless; for very small and isolated systems, it be-

comes impossible to define the concept of appropriate temperature; the melting and boiling temperatures of nano-sized liquid drops of matter are always lower than the corresponding values in the bulk phase of the same material, etc.

There is no information in the literature about the existence of vanadium and cadmium alloys or intermetallic compounds. Vanadium melting point [17] is 1910 °C, cadmium — 321 °C; vanadium boiling point [18] (at which vapor pressure equals atmospheric pressure) is 3392 °C, cadmium — 766 °C.

Instrumental determination of small particle size and melting temperature is very difficult, but alloy formation, a solid dissolution of two metals, proves the presence of ultradisperse particles that can coalesce in a quasi-liquid state at low temperature. In this context, we have studied the double V–Cd alloy by atomized metal deposition to determine the critical sizes of the nanoclusters, the concentration limits of the V–Cd solid solutions, and the phase composition and structure of the film coatings.

Materials and methodology

One of the ways to form nanometer size (<100 nm) ultra-dispersed particle flows consists in metal atomization in a low-pressure plasma. Studies were performed using an ion-plasma unit with oppositely placed planar DC magnetrons with water-cooled targets on the walls of the vacuum chamber. The unit design and the sample atomizing technique were described in detail earlier [15].

The substrate temperature did not exceed 100 °C during sample formation. The ratio of metal concen-

trations in the alloy samples was changed by the atomization rate of magnetron sputtering targets. The ratio of deposited components was controlled by the weight method (by the amount of atomized and deposited metal during the coating formation) and in parallel by the method of Rutherford backscattering of protons at the tandem accelerator UKP-2-1 of the Institute of Nuclear Physics (Almaty).

Metals used in experiments were with major element content, wt.%: vanadium — 99.6; cadmium — 99.99. Targets are made of each of the metals in the disk form, 40 mm in diameter and 4 mm thick.

Sample preparation included sequential operations of vanadium and cadmium target sputtering and deposition of atomized particles on unheated substrates that move relative to the plasma streams in the form of island films — nanometer sublayers — to the proposed total coating thickness. The sublayer thickness was calculated by dividing the total coating thickness by the number of substrate passes relative to the metal-containing plasma flows.

The use of the thickness of the sublayer as a dimensional factor is due to the fact that the change in the melting temperature of the film with decreasing thickness is similar to that of small particles [13], which form according to the “island” principle.

The critical size of the metal particles was determined by reducing the thickness of the sublayer through alternate confinement of niobium and second metal atomizers as a result of each intersection of a metal-containing plasma stream through the moving substrate. The fluxes with dissimilar metal particles were separated by 180° relative to each other, which excluded the formation of solutions when the fluxes touched or crossed. Moreover, the substrate took 3 s to move from the center line of one magnetron atomizer to the second, which was sufficient for crystallization of very small particles, assuming the existing process. The thickness of the sublayer at which the solid solution appears in the coating was considered to be the critical size of the metal particles.

The element concentration at which phases other than the solid solution appeared was considered to be the existence limit of the alloy.

Polycor substrates (α -Al₂O₃) and monocrystalline silicon were used for the coatings. X-ray diffractometer “D8 Advance” (Bruker, Germany) with CuK α -radiation ($\lambda = 0.154051$ nm) and graphite monochromators were used for the X-ray diffraction study of the “V–Cd” system. The lattice parameter value was calculated as the average of all diffraction lines from a given phase.

High-temperature anneals were performed in a vacuum high-temperature furnace based on the URVT-2500.

Results and discussion

The results of determining the critical dimensions of the vanadium and cadmium sublayers by alternating short-range (with a small number of lattice periods) layers and reducing the layer thickness of each metal for a system with a concentration of ~25 at.% Cd are shown in Table 1.

As a result of the obtained samples diffractometrical research it was established (see Table 1) that with the cadmium vanadium capillary-porous system (CPS) thickness of 0.6 and 0.3 nm respectively in the coating of this composition cadmium vanadium solid solution was obtained with a body-centered cubic (BCC) structure and lattice parameter, $a = 0.3931 \pm 0.0009$ nm. So that the vanadium nanoparticles critical size capable of coalescing with cadmium is 0.6 nm. As expected, the critical size of the cadmium particles can be adjusted towards higher values, since increasing the CPS while maintaining the critical size of the vanadium particles with the existing method of coating production of the given composition takes the system out of the range of existence of solid solutions due to alloys with higher concentration of the alloying element. For example, the critical size of cadmium nanoparticles in the formation of our alloys with refractory metals such as niobium [15] and tantalum [19] corresponds to values of 3.2 and 2.1 nm, respectively.

In order to determine the solid solutions concentration boundaries in the V–Cd system taking into account the size factor, 11 coating samples with cadmium concentration from 9.6 to 88.6 at.% have been formed. The coatings composition and the phases detected are given in Table 2.

Fig.1 shows some V–Cd system coatings diffractograms with different cadmium concentrations.

Cadmium and amorphous vanadium phases were detected in the sample with cadmium content of 88.6 at.% (spectrum 1 in Fig. 1). In the concentration interval of 42.0–80.2 at.% Cd (spectrum 2), the cadmium phase coexists with cadmium-vanadium solid solution with BCC structure. Cadmium as a separate phase is not observed in coatings with <31.6 at.% Cd (spectrum 3). Moreover, in this case the cadmium-vanadium solid solution has a predominant orientation (111). At concentrations <14.7 at.% (spectrum 4), the coatings are represented by cadmium-vanadium solid solutions with the lattice parameter of the solid solution

Table 1. Thickness of short-period metal layers and lattice parameters of detected phases in vanadium films containing ~25 at.% Cd

Таблица 1. Толщина короткопериодных слоев металлов и параметры решетки обнаруженных фаз в пленках ванадия, содержащих ~25 ат.% Cd

Layer thick-ness, nm		Phases lattice parameters, nm		
V	Cd	V	Cd	
		<i>a</i>	<i>a</i>	<i>c</i>
16.0	8.0	0.3491 ± 0.0018	0.2981 ± 0.0002	0.5620 ± 0.0003
12.1	6.0	0.3815 ± 0.0012	0.2980 ± 0.0003	0.5621 ± 0.0002
9.3	4.8	0.3868 ± 0.0008	0.2980 ± 0.0002	0.5622 ± 0.0003
6.2	3.0	0.3925 ± 0.0007	0.2982 ± 0.0002	0.5620 ± 0.0003
3.4	1.7	Amorphous		
0.6	0.3	Cadmium vanadium solid solution, <i>a</i> = 0.3931 ± 0.0009 nm		

changing towards the increase due to a considerably larger cadmium atoms radius (0.1727 nm) in comparison to that of vanadium (0.1489 nm) [20]. Change of the lattice parameter of cadmium-vanadium solid solution as well as the solution coexisting with cadmium is shown in Fig. 2.

From data of Fig. 2 one can see that up to ~37 at.% Cd concentration the α -vanadium lattice parameter changes linearly with increase of Cd con-

tent in solution, the saturated solid solution with the average parameter *a* = 0.4001 nm is allocated into a separate phase (coexisting with cadmium) for higher

Table 2. Coatings composition and phases detected

Таблица 2. Состав покрытий и обнаруженные в них фазы

Coatings composition, at. %		Phases detected
V	Cd	
11.4	88.6	Cd + V amorphous
19.8	80.2	Cd + cadmium vanadium solid solution
30.5	69.5	Cd + cadmium vanadium solid solution
35.0	65.0	Cd + cadmium vanadium solid solution
43.3	56.7	Cd + cadmium vanadium solid solution
47.7	52.3	Cd + cadmium vanadium solid solution
57.0	43.0	Cd + cadmium vanadium solid solution
68.4	31.6	Cadmium vanadium solid solution (texture (111))
73.5	26.5	Cadmium-vanadium solid solution
85.3	14.7	Cadmium-vanadium solid solution
90.4	9.6	Cadmium-vanadium solid solution

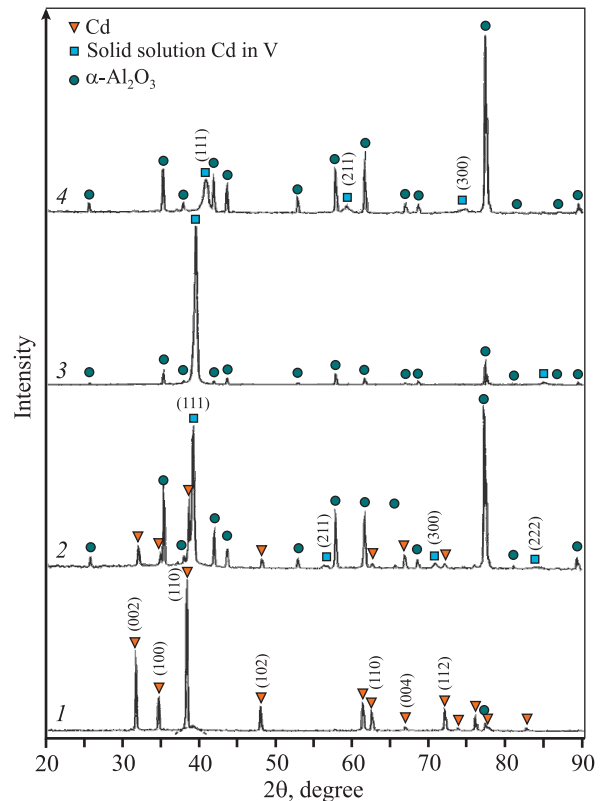


Fig. 1. V–Cd system coatings diffractograms with different cadmium contents

Cd, at. %: 1 – 88.6; 2 – 43.0; 3 – 31.6; 4 – 14.7

Рис. 1. Дифрактограммы покрытий системы V–Cd с различным содержанием кадмия

Cd, ат. %: 1 – 88,6; 2 – 43,0; 3 – 31,6; 4 – 14,7

values of Cd content than mentioned above. That is, the concentration boundary of existence of cadmium solid solutions in vanadium corresponds to ~Cd 37 at.%. Dependence of the α -vanadium lattice parameter before its saturation on the cadmium content in it corresponds to the following equation: a [nm] = $8 \cdot 10^{-4} C_{Cd} + 0.3707$, where C_{Cd} – cadmium concentration, at.%.

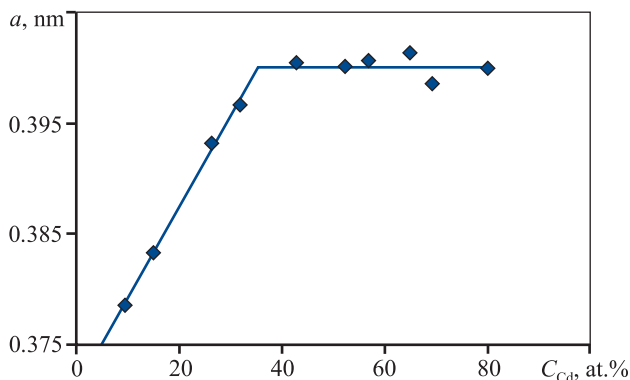


Fig. 2. Cadmium–vanadium solid solution lattice parameter dependence on the cadmium content in the coating

Рис. 2. Зависимость параметра решетки твердого раствора кадмия в ванадии от содержания кадмия в покрытии

SEM-researches of a primary sample with 31.6 at. % cadmium concentration (Fig. 3) have revealed the filamentous crystals of various shapes appearance up to 30 μ m long and 2 μ m thick as well as crystals resembling sprouting plants on the coating surface besides formations of 1–2 μ m.

The mechanism of such formations on the samples surface is apparently similar to the phenomenon of similar tin crystals formation in the form of whiskers and protrusions on Lu_4Sn_5 surface at storage in the air during several days where the filamentous crystals growth initiating force are compressive matrix compound stresses [21]. The surface of the sample annealed at 300 °C in vacuum losing a significant portion (by preliminary data, 30–40 wt.% [22]) of cadmium by evaporation) is represented by melted grains of irregular shape that differ in size.

A similar study of a sample with 69.5 at.% cadmium content characterized by coexisting phases of cadmium and cadmium–vanadium solid solution showed a different surface topography (Fig. 4). The initial sample has no pronounced grain formations. After annealing, the surface is represented by “shatt” formations with a porous structure inside the film due to cadmium evaporation.

In the coating sample diffractometric study with

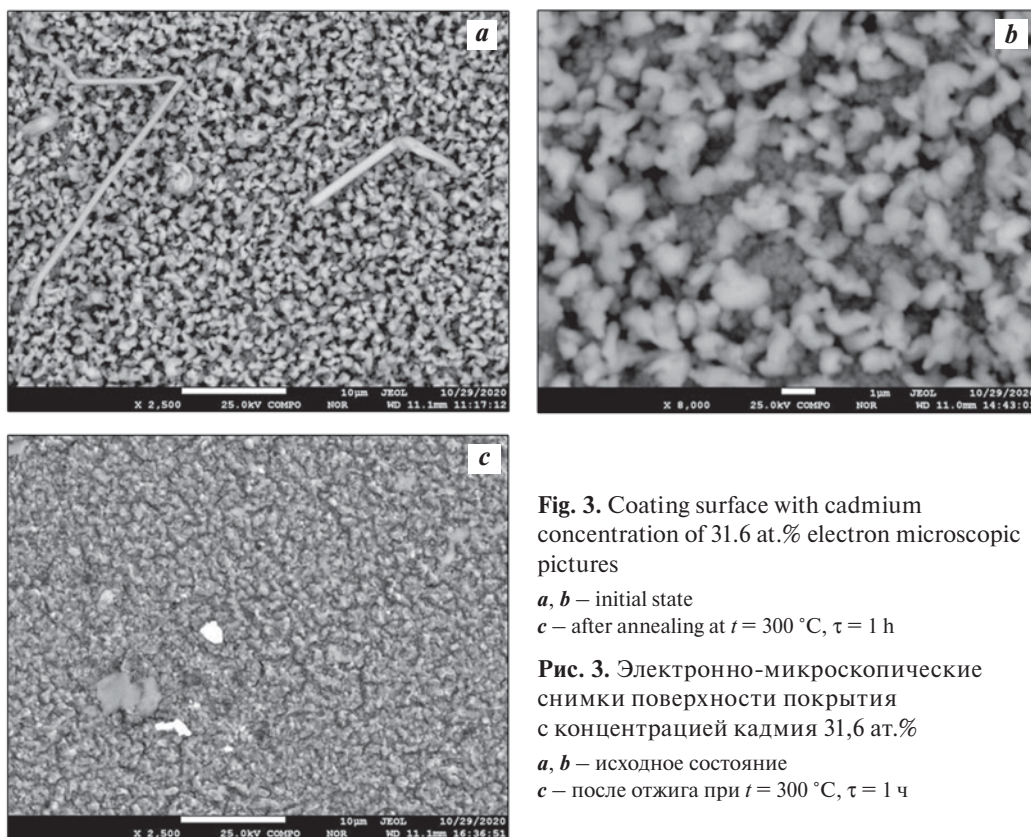


Fig. 3. Coating surface with cadmium concentration of 31.6 at.% electron microscopic pictures

a, b – initial state
c – after annealing at $t = 300$ °C, $\tau = 1$ h

Рис. 3. Электронно-микроскопические снимки поверхности покрытия с концентрацией кадмия 31,6 ат.%

a, b – исходное состояние
c – после отжига при $t = 300$ °C, $\tau = 1$ ч

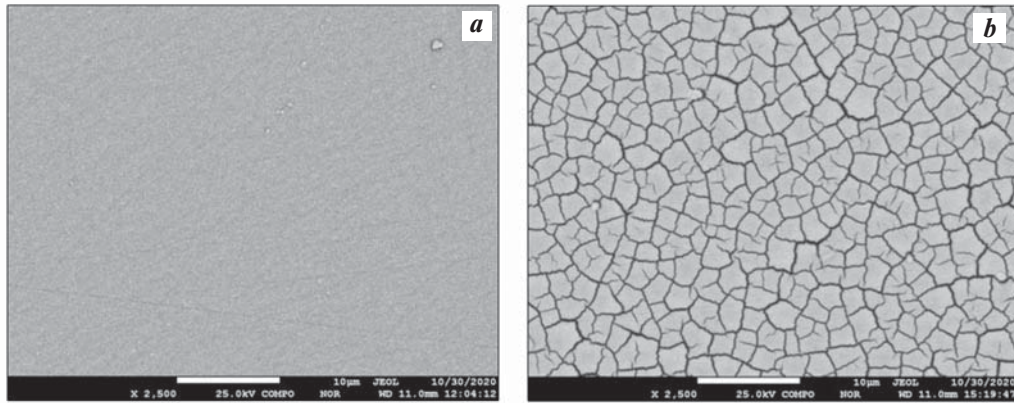


Fig. 4. Coating surface with 69.5 at.% cadmium concentration electron-microscopic pictures

a – initial state; *b* – after annealing at $t = 300\text{ }^{\circ}\text{C}$, $\tau = 1\text{ h}$

Рис. 4. Электронно-микроскопические снимки поверхности покрытия с концентрацией кадмия 69,5 ат.%

a – исходное состояние; *b* – после отжига при $t = 300\text{ }^{\circ}\text{C}$, $\tau = 1\text{ ч}$

9.6 at.% cadmium content (Fig. 5) annealed at $400\text{ }^{\circ}\text{C}$ for 1 h, the reflexes of the phase which can be assigned to cubic syngony are observed. Reflex (111) of this phase exactly coincides with reflex (104) ($d_{hkl} = 0.2552\text{ nm}$), and reflex (220) coincides with polycor reflex (211) ($d_{hkl} = 0.1546\text{ nm}$). The assumed lattice parameter of this cubic phase $a = 0.4393 \pm 0.0008\text{ nm}$ suggests that the compound is a complex cadmium-vanadium oxide with the $\text{V}_x\text{Hf}_{1-x}\text{O}$ formula, since cadmium oxide CdO (ICPDS card number 1011051) with lattice parameter $a = 0.4730\text{ nm}$ is known. The measured d_{hkl} values of the presupposed phase and the corresponding Miller indices are given below:

$d_{hkl},\text{ nm}$	0.2552	0.2195	0.1546	0.1269
hkl	(111)	(200)	(220)	(222)

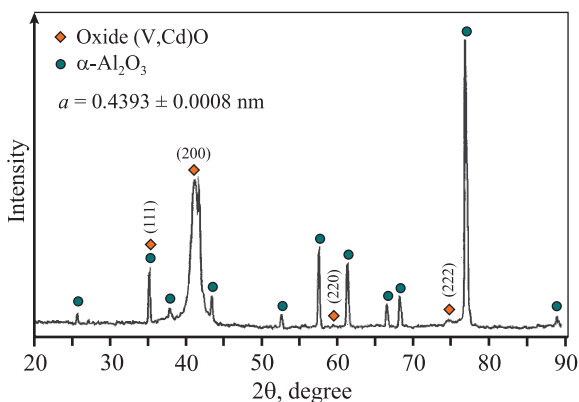


Fig. 5. Coating sample containing 9.6 Cd at.% diffractogram after annealing ($t = 400\text{ }^{\circ}\text{C}$, $\tau = 1\text{ h}$)

Рис. 5. Дифрактограмма образца покрытия с содержанием 9,6 ат. % Cd после отжига ($t = 400\text{ }^{\circ}\text{C}$, $\tau = 1\text{ ч}$)

Oxide formation after the sample extraction from vacuum volume testifies, in our opinion, the developed structure presence in the film depth. Judgment on the presence of through pores in this case is not possible, but the probability of their presence is very high. This requires additional studies along with examination of the cadmium evaporation degree from the films of similar composition and from cadmium-vanadium solid solution.

At the same time, coatings with high cadmium content and subsequent evaporation from their mixtures with cadmium-vanadium solid solution can be used to obtain materials with highly developed surface.

Conclusion

As a result of this research the possibility of obtaining ultradisperse vanadium and cadmium particles which can form alloys and compounds in the quasi-liquid state was confirmed. Formation of coatings with ultradisperse metal particles allows obtaining alloys (solid solutions) at temperatures below $100\text{ }^{\circ}\text{C}$. The critical size of vanadium particles capable of coalescence with cadmium was determined to be 0.6 nm . For cadmium, an underestimated formations critical size was obtained as compared to the confirmed data from earlier studies, 0.3 nm .

The concentration boundary of the cadmium-vanadium solid solutions existence is $\sim\text{Cd } 37\text{ at.}\%$ content, provided that the parameter of the α -vanadium volume-centered cubic lattice linearly increases because of larger cadmium atomic radius in relation to vanadium. At higher (up to $80.2\text{ at.}\%$) cadmium content, the film coating is represented by a mixture

of cadmium and cadmium-vanadium solid solution phases.

Electron-microscopic studies revealed the presence of filamentary crystals and cadmium formations on the sample surface in the solid solutions field (31.6 at.% Cd). We assume by virtue of the study results of other authors that they appeared due to the lattice pressure of the matrix metal.

Annealing of samples in vacuum is accompanied by diffusion of cadmium to the phase interface and evaporation, which reduces its concentration in the coating. Annealing of cadmium-rich films in the region of cadmium phases and solid solutions (69.5 at.% Cd) is associated with coating cracking and pore formation. After further investigation, it can be used as a method for the recovery of porous vanadium.

References

1. Peppiatt S.J. The melting of particles. II. Bismuth. *Proceedings of the Royal Society of London. Series A*. 1975; A345 (1642): 401–412.
<https://doi.org/10.1098/rspa.1975.0145>
2. Berty J., David M.J., Lafourcade L. Etude de la surfusion de films mines de bismuth par diffraycon des electrons. *Thin Solid Films*. 1977; 46 (2): 177–185.
[https://doi.org/10.1016/0040-6090\(77\)90060-8](https://doi.org/10.1016/0040-6090(77)90060-8)
3. Zhdanov G.S. Temperature hysteresis of the phase transition and the crystallization mechanism of thin metal films. *Fizika tverdogo tela*. 1977; 19 (1): 299–301. (In Russ.).
Жданов Г.С. Температурный гистерезис фазового перехода и механизм кристаллизации тонких металлических пленок. *Физика твердого тела*. 1977; 19 (1): 299–301.
4. Buffat Ph., Borel J-P. Size effect on the melting temperature of gold particles. *Physical Review A*. 1976; 13 (6): 2287–2298.
<https://doi.org/10.1103/PhysRevA.13.2287>
5. Perepezko J.H., Rasmussen D.H. Solidification of highly supercooled liquid metal and alloys. *Journal of Non-Crystalline Solids*. 1993; 156–158: 463–472.
[https://doi.org/10.1016/0022-3093\(93\)90002-F](https://doi.org/10.1016/0022-3093(93)90002-F)
6. Roduner E. Size matters: why nanomaterials are different. *Chemical Society Reviews*. 2006; 35: 583–592
7. Zou C., Gao Y., Yang B., Zhai Q. Size dependent melting properties of Sn nanoparticles by chemical reduction synthesis. *Transactions of Nonferrous Metals Society of China*. 2010; 20 (2): 248–253.
[https://doi.org/10.1016/S1003-6326\(09\)60130-8](https://doi.org/10.1016/S1003-6326(09)60130-8)
8. Jiang H., Moon K., Dong H. Size dependent melting properties of tin nanoparticles. *Chemical Physics Letters*. 2006; 429 (4): 492–496.
<https://doi.org/10.1016/j.cplett.2006.08.027>
9. Stowell M.J. The solid-liquid interfacial free energy of lead from supercooling data. *Philosophical Magazine: A Journal of Theoretical, Experimental and Applied Physics*. 1970; 22 (176): 1–6.
<https://doi.org/10.1080/14786437008228146>
10. Qingshan F., Yongqiang X., Zixiang C. Size — and shape — dependent surface thermodynamic properties of nanocrystals. *Journal of Physics and Chemistry of Solids*. 2018; 116: 79–85.
<https://doi.org/10.1016/j.jpcs.2018.01.018>
11. Mu J., Zhu Z.W., Zhang H.F. Size dependent melting behaviors of nanocrystalline in particles embedded in amorphous matrix. *Journal of Applied Physics*. 2012; 111 (4): 043515 (1–4).
<https://doi.org/10.1063/1.3686624>
12. Luo W., Su K., Li K., Li Q. Connection between nanostructured materials' size dependent melting and thermodynamic properties of bulk materials. *Solid State Communications*. 2011; 151 (3): 229–233.
<https://doi.org/10.1016/j.ssc.2010.11.025>
13. Roduner E. Dimensional effects in nanomaterials. Moscow: Tekhnosfera, 2010. (In Russ.).
Родунер Э. Размерные эффекты в наноматериалах. М.: Техносфера, 2010.
14. Tuleushev Yu.Zh., Volodin V.N., Zhakanbaev E.A. New Ta₃Be phase in the film coatings of tantalum-beryllium alloys. *Physics of Metals and Metallography*. 2019. 120 (4): 361–365.
<https://doi.org/10.1134/S0031918X19040148>
15. Volodin V.N., Tuleushev Yu.Zh., Trebukhov S.A., Nitsenko A.V., Burabaeva N.V. Fabrication of binary niobium alloys with low-melting metals by the deposition of nanoparticles. *Russian Journal of Non-Ferrous Metals*. 2019; 60 (6): 639–645.
<https://doi.org/10.3103/S106782121906021X>
16. Volodin V.N., Tuleushev Yu.Zh., Zhakanbaev E.A., Trebukhov S.A., Burabaeva N.V., Nitsenko A.V. Synthesis of intermetallic phases in the Nb—Cd and Mo—Cd systems by ion-plasma sputtering and atomic layer deposition of metals in vacuum. *Inorganic Materials*. 2020; 56 (1): 28–34.
<https://doi.org/10.1134/S0020168520010185>
17. State diagrams of binary metallic systems: Handbook. Vol. 3. Ed. N.P. Lya-kishev. Moscow: Mashinostroenie, 2001. (In Russ.).
Диаграммы состояния двойных металлических систем: Справочник. Т. 3. Под ред. Н.П. Лякишева. М.: Машиностроение, 2001.

18. Malyshev V.P., Turdukozhayeva A.M., Ospanov E.A., Sarkenov B. Evaporation and boiling of simple substances. Moscow: Nauchnyi mir, 2010. (In Russ.).
Малышев В.П., Турдукожаева А.М., Оспанов Е.А., Саркенов Б. Испаряемость и кипение простых веществ. М.: Научный мир, 2010.
19. Obtaining binary alloys of cadmium with refractory metals by deposition of nanoparticles. In: *Collection of reports XI International Congress «Non-Ferrous Metals and Minerals – 2019»* (Krasnoyarsk, 16–20 Sept. 2019). Krasnoyarsk: Nauchno-Innovatsionnyi Tsentr, 2019. P. 1019–1028. (In Russ.).
Володин В.Н., Ниценко А.В., Требухов С.А., Бурабаева Н.М., Тулеушев Ю.Ж. Получение двойных сплавов кадмия с тугоплавкими металлами осаждением наночастиц. В сборнике докладов XI международно-го конгресса «Цветные металлы и минералы — 2019» (Красноярск, 16–20 сент. 2019 г.). Красноярск: Научно-инновационный центр, 2019. С. 1019–1028.
20. Physical metal science. Ed. R.U. Kan, P. Haazen. Moscow: Metallurgiya, 1987. (In Russ.).
Физическое металловедение. Под ред. Р.У. Кана, П. Хаазена. М.: Металлургия, 1987.
21. Chuang T.H., Lin H.J., Chi C.C. Rapid growth of tin whiskers on the surface of Sn–6.6Lu alloy. *Science: Materials*. 2007; 56 (1): 45–48.
22. Volodin V.N., Tuleushev Yu.Zh., Kenzhaliev B.K., Trebukhov S.A. Thermal degradation of hard alloys of niobium-cadmium system at low pressure. *Kompleksnoe ispol'zovanie mineral'nogo syr'ya*. 2020; (1 (312)): 41–47. (In Russ.).
<https://doi.org/10.31643/2020/6445/05>
Володин В.Н., Тулеушев Ю.Ж., Кенжалиев Б.К., Требухов С.А. Термическая деградация твердых сплавов системы ниобий–кадмий при низком давлении. *Комплексное использование минерального сырья*. 2020; (1 (312)): 41–47.

Information about the authors

Valerii N. Volodin – Dr. Sci. (Phys.-Math.), Dr. Sci. (Eng.), Prof., Principal Scientist of the Laboratory “Ion-Plasma Technologies”, Institute of Nuclear Physics.
<https://orcid.org/4701-1670-0043>
E-mail: volodinv_n@mail.ru

Yurii Zh. Tuleushev – Cand. Sci. (Phys.-Math.), Prof., Leading Scientist of the Laboratory “Ion-Plasma Technologies”, Institute of Nuclear Physics.
<https://orcid.org/5308-0348-2509>
E-mail: yuriy.tuleushev@mail.ru

Asel' K. Kaliyeva – Junior Research Scientist of the Laboratory “Ion-Plasma Technologies”, Institute of Nuclear Physics.
<https://orcid.org/7710-2140-1000>
E-mail: inbox2110@mail.ru; lab_ipt@mail.ru

Eldar A. Zhakanbayev – Cand. Sci. (Phys.-Math.), Head of the Laboratory “Ion-Plasma Technologies”, Institute of Nuclear Physics.
<https://orcid.org/8009-0450-2235>
E-mail: lab_ipt@mail.ru

Arsen K. Mamyrbayev – Engineer of the Laboratory “Ion-Plasma Technologies”, Institute of Nuclear Physics.
<https://orcid.org/9702-2227-4561>
E-mail: lab_ipt@mail.ru

Информация об авторах

Валерий Николаевич Володин – д.ф.-м.н., д.т.н., профессор, главный научный сотрудник лаборатории ионно-плазменных технологий Института ядерной физики (ИЯФ) Министерства энергетики Респ. Казахстан.
<https://orcid.org/4701-1670-0043>
E-mail: volodinv_n@mail.ru

Юрий Жианшахович Тулеушев – к.ф.-м.н., профессор, ведущий научный сотрудник лаборатории ионно-плазменных технологий ИЯФ.
<https://orcid.org/5308-0348-2509>
E-mail: yuriy.tuleushev@mail.ru

Асель Кыдырханкызы Калиева – младший научный сотрудник лаборатории ионно-плазменных технологий ИЯФ.
<https://orcid.org/7710-2140-1000>
E-mail: inbox2110@mail.ru; lab_ipt@mail.ru

Елдар Асхатович Жаканбаев – к.ф.-м.н., заведующий лабораторией ионно-плазменных технологий ИЯФ.
<https://orcid.org/8009-0450-2235>
E-mail: lab_ipt@mail.ru

Арсен Кайратулы Мамырбаев – инженер лаборатории ионно-плазменных технологий ИЯФ.
<https://orcid.org/9702-2227-4561>
E-mail: arsen.mamyrbayev@gmail.com

Contribution of the authors

V.N. Volodin – formation of the main concept, goal and objectives of the study, writing the text of the article, formulation of the conclusions.

Yu.Zh. Tuleushev – conducting the calculations, testing the samples, preparing the text of the article.

A.K. Kaliyeva – realization of experiment, processing of the research results.

E.A. Zhakanbayev – scientific guidance, correction of the text and conclusions.

A.K. Mamyrbayev – conducting the calculations, analysis of the research results.

Вклад авторов

В.Н. Володин – формирование основной концепции, постановка цели и задачи исследования, написание текста статьи, формулировка выводов.

Ю.Ж. Тулеушев – проведение расчетов, испытаний образцов, подготовка текста статьи.

А.К. Калиева – проведение экспериментов, обработка результатов исследований.

Е.А. Жаканбаев – научное руководство, корректировка текста, корректировка выводов.

А.К. Мамырбаев – проведение расчетов, анализ результатов исследований.

The article was submitted 14.04.2022, revised 25.05.2022, accepted for publication 26.05.2022

Статья поступила в редакцию 14.04.2022, доработана 23.05.2022, подписана в печать 26.05.2022

UDC 544.034

<https://doi.org/10.17073/0021-3438-2023-1-75-83>

Research article

Научная статья



Interdiffusion in refractory metal systems with a BCC lattice: titanium–tantalum and titanium–multicomponent (high-entropy) alloy

M.I. Razumovsky, A.O. Rodin, B.S. Bokstein

National University of Science and Technology “MISIS”

4 Leninskii pr., Moscow, 119049, Russia

✉ Mikhail I. Razumovsky (razmikhail@gmail.com)

Abstract: In this work, the interdiffusion features in multicomponent (high-entropy) alloys of refractory metals were studied. The following pairs were chosen as the diffusion study objects: titanium–equiatomic alloy (Hf–Nb–Ta–Ti–Zr–Mo) and titanium–tantalum for the sake of comparison. The article covers the issues of sample preparation, microstructure study, sample preparation methodology for diffusion research, and experimental results. Diffusion annealing was carried out for 12 h in a vacuum at a residual argon pressure of $6.65 \cdot 10^{-3}$ Pa and a temperature of 1200 °C. Particular attention was paid to the method of combining diffusion pairs (titanium with tantalum, titanium with alloy) by thermal cycling near the polymorphic transformation temperature in titanium (882 °C) within ± 50 °C. The behaviour of the most characteristic elements (Ta, Zr, Ti) in the weld area after the titanium and alloy diffusion pair joining was demonstrated. This is the first time that data on the dependence of the intensity of the corresponding spectral line for titanium and elements of a multicomponent alloy on the penetration depth were obtained. A change in the signal intensity for system elements was observed at a depth of 150–200 μm , whereas a sharp drop in the signal intensity was seen to occur at depths of about 50 μm . The effective value of the coefficient of diffusion of elements into titanium averaged over all elements of the alloying system (except for titanium) at a temperature of 1200 °C was calculated. The obtained value was compared to reference data: the self-diffusion coefficient in β -titanium and diffusion coefficients in titanium pairs with alloy doping elements.

Keywords: high-entropy alloys based on multiple refractory metals, interdiffusion parameters

Funding: This study was carried out with the financial support of a grant from the Russian Foundation for Basic Research (Project No. 20-03-00387).

Acknowledgments: The authors acknowledge V.K. Portnoi and E.A. Kolesnikov for their help with the experiments.

For citation: Razumovsky M.I., Rodin A.O., Bokstein B.S. Interdiffusion in refractory metal systems with a BCC lattice: titanium–tantalum and titanium–multicomponent (high-entropy) alloy. *Izvestiya. Non-Ferrous Metallurgy*. 2023; 29 (1): 75–83. (In Russ.).

<https://doi.org/10.17073/0021-3438-2023-1-75-83>

Взаимная диффузия в системах на основе тугоплавких металлов с ОЦК-решеткой: титан–тантал и титан – многокомпонентный (высокоэнтропийный) сплав

М.И. Разумовский, А.О. Родин, Б.С. Бокштейн

Национальный исследовательский технологический университет «МИСИС»

119049, Россия, г. Москва, Ленинский пр-т, 4

✉ Михаил Игоревич Разумовский (razmikhail@gmail.com)

Аннотация: Изучены особенности взаимной диффузии в многокомпонентных (высокоэнтропийных) сплавах на основе тугоплавких металлов. В качестве объектов диффузионного исследования были выбраны следующие пары: титан – эквиатомный

сплав (Hf–Nb–Ta–Ti–Zr–Mo) и, для сравнения, титан–тантал. Рассмотрены вопросы приготовления образцов, исследования микроструктуры, методика подготовки образцов для изучения диффузии и экспериментальные результаты. Диффузионный отжиг был проведен в течение 12 ч в вакууме с остаточным давлением аргона $6,65 \cdot 10^{-3}$ Па при температуре 1200 °С. Особое внимание уделено методике соединения диффузионных пар (титана с танталом, титана со сплавом) путем термодиффузионного цикла вблизи температуры полиморфного превращения в титане (882 °С) в пределах ± 50 °С. Показано поведение наиболее характерных элементов (Ta, Zr, Ti) в области сварного шва после соединения диффузионной пары титана и сплава. Впервые получены данные о зависимости интенсивности соответствующей линии спектра для титана и элементов многокомпонентного сплава от глубины проникновения. Изменение интенсивности сигнала для элементов систем наблюдается на глубине 150–200 мкм, а резкое падение интенсивности сигнала происходит на глубинах порядка 50 мкм. Рассчитано усредненное по всем элементам системы легирования сплава (за исключением титана) эффективное значение коэффициента диффузии элементов в титан при температуре 1200 °С. Проведено сравнение полученного значения со справочными данными: коэффициентом самодиффузии в β -титане, коэффициентами диффузии в парах титана с легирующими элементами сплава.

Ключевые слова: высокоэнтропийные сплавы на основе многих тугоплавких металлов, параметры взаимной диффузии

Финансирование: Работа выполнена при финансовой поддержке гранта Российского фонда фундаментальных исследований (проект № 20-03-00387).

Благодарности: Коллектив авторов выражает благодарность В.К. Портному и Е.А. Колесникову за помощь в проведении экспериментов.

Для цитирования: Разумовский М.И., Родин А.О., Бокштейн Б.С. Взаимная диффузия в системах на основе тугоплавких металлов с ОЦК-решеткой: титан–тантал и титан – многокомпонентный (высокоэнтропийный) сплав. *Известия вузов. Цветная металлургия*. 2023; 29 (1): 75–83. <https://doi.org/10.17073/0021-3438-2023-1-75-83>

Introduction

Achieving higher-than-average operating temperatures of gas turbine engines up to 1400 °C requires the use of alloys with a melting point exceeding 2000 °C. Refractory metal alloys are the most suitable for this purpose. In addition to their high melting points, these alloys usually contain more than 5 elements with a concentration of 5 to 35 % each, and hence are characterised by high configurational entropy. This is why they were called high-entropy alloys (HEA) [1, 2].

Since the increase in entropy is associated with an increase in the system disorder, the suggestion was made that the diffusion could be slowed down by the sluggish diffusion effect [3, 4]. There is very little data available on the dependence of the interdiffusion coefficients on the composition of the alloy in binary systems of refractory metals, even less for multicomponent alloys. The objective of this study was to select and analyse articles published in high-level influential journals (*Acta Materialia*, *Journal of Alloys and Compounds*, *Intermetallics*, etc.) in the 2018–2020 period. The articles were selected based on two criteria: 1) the subject matter of the study shall be multicomponent HEA; 2) the results obtained shall concern the diffusion mobility of the components.

Among the 47 articles selected, only 10 [5–14] met the first criterion, whereas only 3 articles [6; 9;

11] covered the problems of diffusion in the HEA of refractory metals with a BCC lattice. There are much more studies on diffusion in multicomponent HEAs with an FCC lattice than on those with a BCC lattice. The authors of [7] believe that “such studies still have a long way to go”.

The general conclusions may be formulated as follows: the slowing down of diffusion in high-entropy alloys (sluggish effect) is not uniformly present in all HEAs and depends on their composition; the results obtained by X-ray spectral microanalysis (EDX) proved to be the most informative; the sluggish diffusion effect is more pronounced for BCC structures than for FCC structures, although there have been much more studies conducted on FCC structures that are currently available; some authors suggest the possibility of the occurrence of a dissociative or interstitial mechanism in a BCC HEA, which is a consequence of the disordered structure, leading to increased, rather than sluggish, diffusion.

The main task of this study, therefore, is to carry out a comparative analysis of diffusion processes in diffusion pairs — one containing an alloy and the other containing single-component substances. The choice of the alloy composition — the multicomponent equiatomic alloy HfNbTaTiZrMo, is based on the analysis made in our review [15]

Sample preparation

To prepare the initial mixtures, «high-purity» class (99.96 %) powders of components (Hf, Nb, Ta, Ti, Zr, and Mo) with particle sizes of 40–80 μm were used. The powder mixture¹ was ground in a P-7 planetary mill (Fritsch, Germany) in an argon atmosphere at a powder-to-ball mass ratio of 1 : 8.

Hot isostatic pressing (HIP) was carried out in a laboratory gasostatic extruder at a temperature of 1200 °C for at least 2 h of exposure, and the powders were compacted in steel capsules that had been pre-evacuated during HIP.

X-ray spectral microanalysis (EDX) of the compacted samples was carried out using a scanning electron microscope of the brand LEO EVO 50 XVP (Carl Zeiss, Germany) with an INCA ENERGY (Oxford Instruments, UK) module.

The main phase obtained during the powder mixture grinding is a BCC solid solution with a lattice period $a \sim 0.34 \text{ nm}$ [16].

Microstructure of multicomponent alloys

In this work, thin, polished sections of pure titanium, tantalum, and an alloy based on multiple refractory metals were made. A mixture of hydrofluoric and nitric acids was used to reveal the resulting grain structure.

The structure was studied using an Axio Vert.A1 (Carl Zeiss, Germany) optical microscope and a JSM-6480LV (SEM) (JEOL, Japan) electron microscope equipped with an INCA ENERGY Dry Cool (Oxford Instruments, Great Britain) energy-dispersive spectroscopy module, as well as on a FEGFEINavaNanoSEM (Field Electron and Ion Company, FEI, USA) microscope fitted with a Bruker (Germany) module.

Fig. 1 shows a photograph of the homogeneous structure of one of the alloy samples.

Sample preparation method for diffusion studies

Diffusion welding was used for the diffusion contact of the samples. A stainless-steel clamp was placed in a quartz reactor in a vertical pipe furnace to provide and

maintain the $\sim 2 \text{ MPa}$ pressure required for welding. The interior part of the reactor was argon-purged to exclude any oxidation.

The mode of preparation of diffusion pairs consisted in thermal cycling at approximately the titanium polymorphic transformation temperature $\pm 50 \text{ }^\circ\text{C}$. One cycle consisted in heating the samples to a temperature of 930 °C and cooling them down to a temperature of 830 °C with multiple cycling or to room temperature with a single cycling. The cooling procedure involved

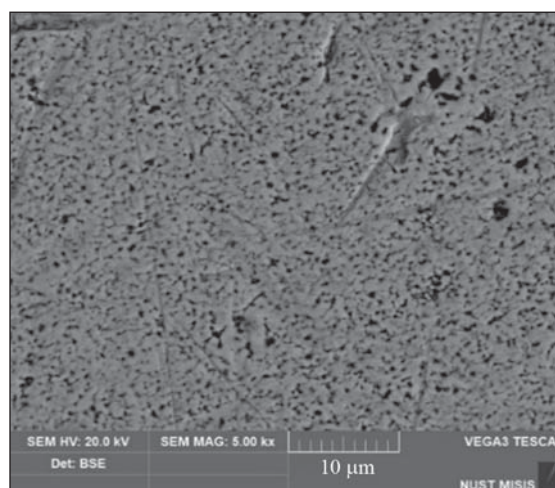


Fig. 1. SEM image of the alloy sample structure

Рис. 1. Электронное изображение (SEM) структуры образца сплава

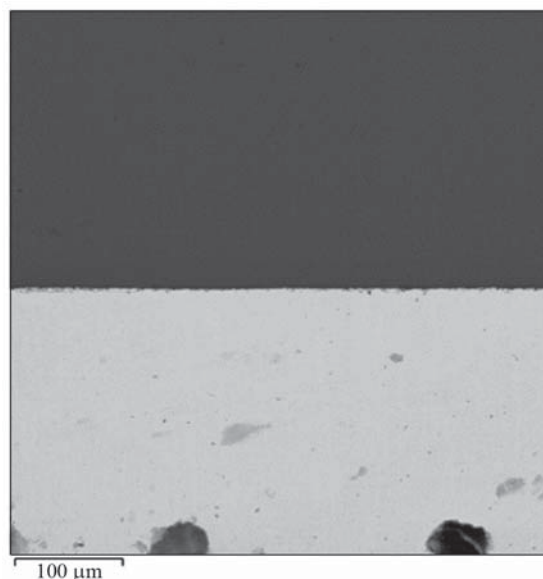


Fig. 2. SEM image of a welded joint between titanium and tantalum plates

Рис. 2. Электронное изображение (SEM) сварного шва между пластинами титана и тантала

¹ Samples of a refractory-metal multicomponent alloy were obtained using equipment of Lomonosov Moscow State University.

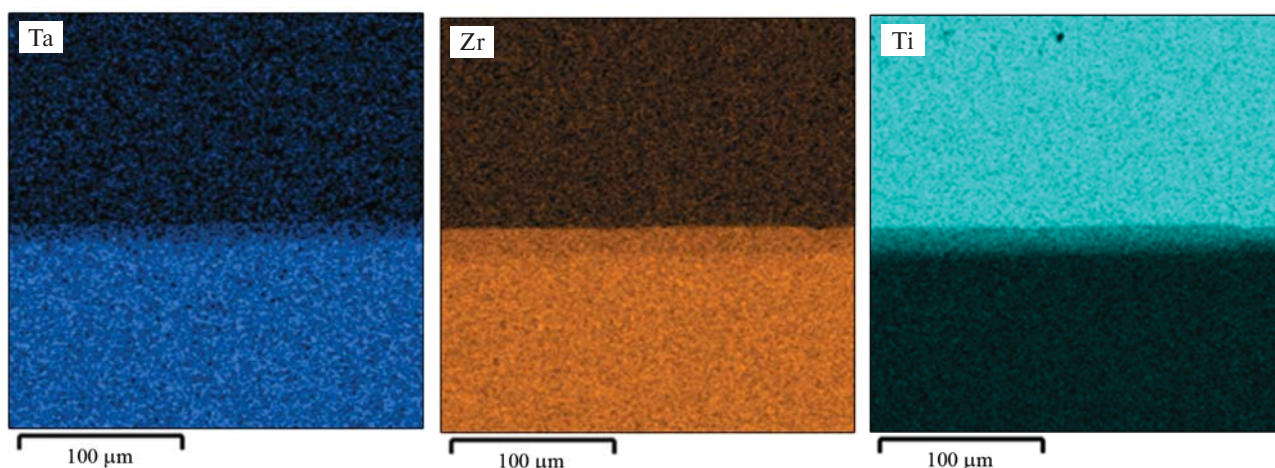


Fig. 3. SEM-EDS image showing element distribution in the welded titanium–alloy joint area

Рис. 3. Изображение SEM-EDS распределения элементов в области сварного шва титана и сплава

removing the quartz reactor containing the samples from the furnace, followed by holding at room temperature. A TVR A1 thermocouple was used to determine the change in temperature of the samples in the reactor.

After welding, the samples were specially processed to be able to examine the welded joint. For this, parts of the welded samples were removed by machining with grinding wheels, following which the welded joint areas were polished and then examined by X-ray spectroscopy. Fig. 2 and Fig. 3 show the SEM image of the weld and the element distribution in the welded joint area.

The size of the transition zone formed as a result of the fabrication of the diffusion pair is within a few micrometres and, apparently, is a consequence of phase recrystallisation. The obtained weld joints appeared continuous, with no pores or contraction cavities.

Experimental results and estimated diffusion coefficients

Diffusion annealing was carried out for 12 h in a vacuum with a residual argon pressure of $6.65 \cdot 10^{-3}$ Pa at a temperature of 1200 °C. After annealing, the samples were cut along the direction of diffusion penetration and the resulting surface ground and polished. Fig. 4 shows a typical polished surface. The lower, darker part is titanium, and the lighter part is the alloy. The dots show the areas of energy-dispersive analysis of the chemical composition. The distance between the dots is about 35 μm. Fig. 5 shows a typical spectrum.

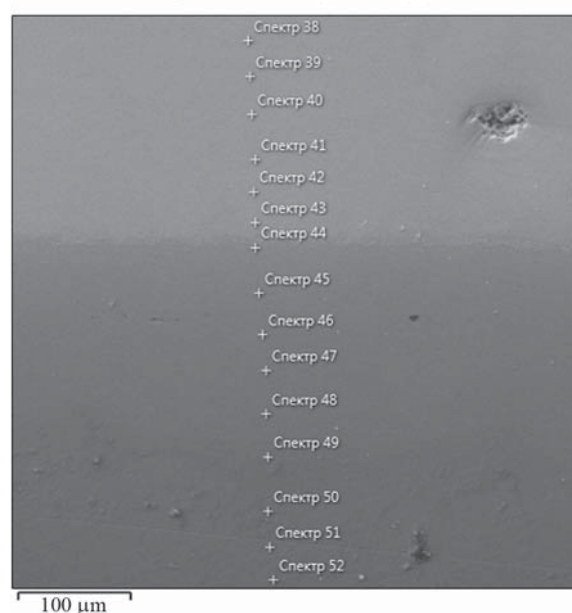


Fig. 4. EDX of an interdiffusion zone of a titanium–alloy pair (white crosses accordance each spectrum numbers from 38 to 52)

Рис. 4. РСМА зоны взаимной диффузии в паре сплав–титан

It is clear that interdiffusion is associated mainly with the penetration of the alloy components into titanium as the more fusible part of the system (Fig. 6); a change in signal intensity is observed at a distance of 150–250 μm for all elements. A sharp drop in intensity takes place at depths of ± 50 μm.

Data on the recalculated concentrations of the components are given in the table.

Figure 7 shows data on the dependence of the intensity of the corresponding spectral line for titanium and other alloy components.

Fig. 8 shows the concentration distribution of all elements of the HEA doping system in the interdiffusion zone. For comparison, a line corresponding to the description using the erfc-shaped solution is shown [17; 18]:

$$C(x, t) = C_n + \frac{C_0 - C_n}{2} \left\{ 1 - \operatorname{erf} \left(\frac{x - x_0}{2\sqrt{Dt}} \right) \right\},$$

where C_n is the minimum concentration of the reference element; C_0 is the element concentration in the equiatomic alloy; D is the diffusion coefficient; t is the time; x_0 is the interface coordinate.

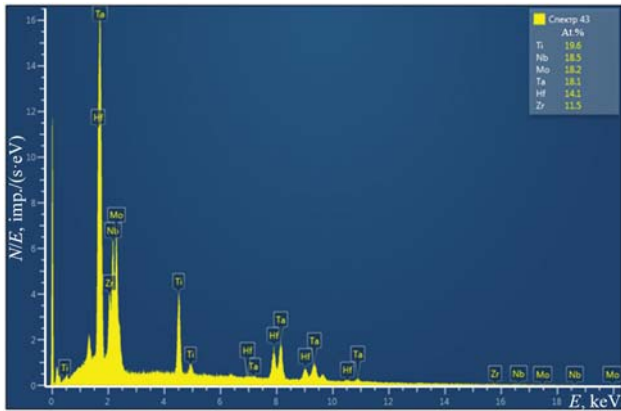


Fig. 5. Typical EDX spectrum in the interdiffusion zone of a titanium–alloy pair near the interface

Рис. 5. Типичный спектр РСМА в зоне взаимной диффузии пары титан–сплав вблизи поверхности раздела

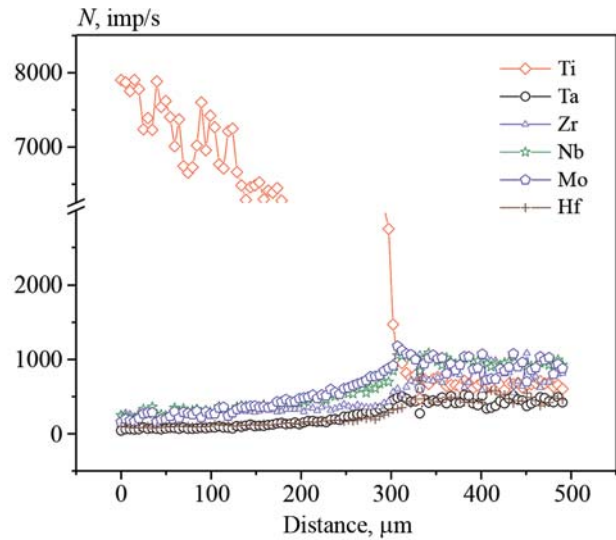


Fig. 6. Change in intensity of spectral lines in the interdiffusion zone of the titan–alloy pair

Рис. 6. Изменение интенсивности линий спектра в зоне взаимной диффузии в паре титан–сплав

Element concentration in the interdiffusion zone, at.%

Концентрации элементов в зоне взаимной диффузии, ат.%

Spectrum Ref. No.	Coordinate, μm	Ti	Zr	Hf	Mo	Ta	Nb
38	0	15.6	20.6	18.3	14.7	14.7	14.7
39	35	16.6	17.9	16.6	15.6	16.7	16.6
40	70	17.6	9.3	13.5	19.7	19.6	19.4
41	105	17.0	13.4	15.5	18.4	18.4	17.3
42	140	17.8	14.3	15.9	17.3	16.7	18.0
43	175	19.6	11.5	14.1	18.2	18.1	18.5
44	210	60.4	3.6	5.7	9.8	10.0	8.4
45	245	75.6	2.9	3.9	5.2	5.1	4.6
46	280	80.0	2.7	2.7	3.5	3.5	3.3
47	315	83.3	2.5	2.4	2.8	2.7	3.0
48	350	85.5	2.1	2.0	2.1	2.0	2.3
49	385	87.5	2.1	1.9	1.6	1.4	1.7
50	420	87.3	2.2	1.5	1.6	1.1	1.7

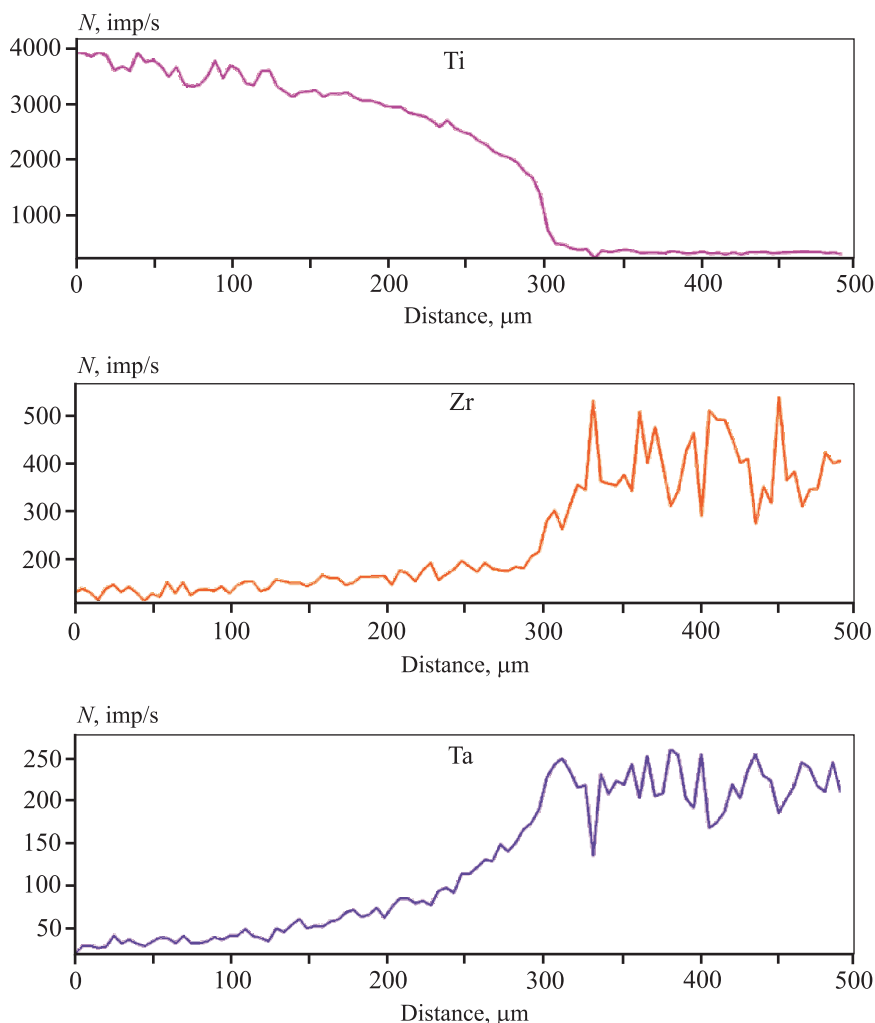


Fig. 7. Intensity profiles of some alloy components in the interdiffusion zone

Рис. 7. Профили интенсивности некоторых компонентов сплава в зоне взаимной диффузии

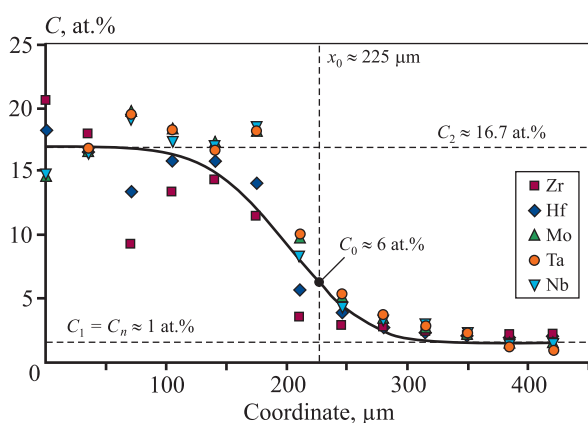


Fig. 8. Element distribution in the alloy–titanium diffusion zone

Рис. 8. Распределение элементов в диффузионной зоне пары сплав–титан

In Fig. 8, to the left of the x_0 plane is the alloy region and to the right is the titanium region.

Elements tend to have a similar behaviour that can be described well by the proposed solution. The experimental points for the titanium–HEA pair correspond to the diffusion coefficient $D = 3.0 \cdot 10^{-14} \text{ m}^2/\text{s}$.

Similar studies were carried out for the titanium–tantalum pair. Fig. 9 shows the photomicrograph and concentration profile of this pair.

The results presented show a significant difference between the diffusion processes in tantalum–titanium and alloy–titanium pairs. The data obtained for the titanium–tantalum pair correspond to the diffusion coefficient $D = 5.0 \cdot 10^{-16} \text{ m}^2/\text{s}$, which is approximately 2 orders of magnitude lower than for the titanium–HEA pair.

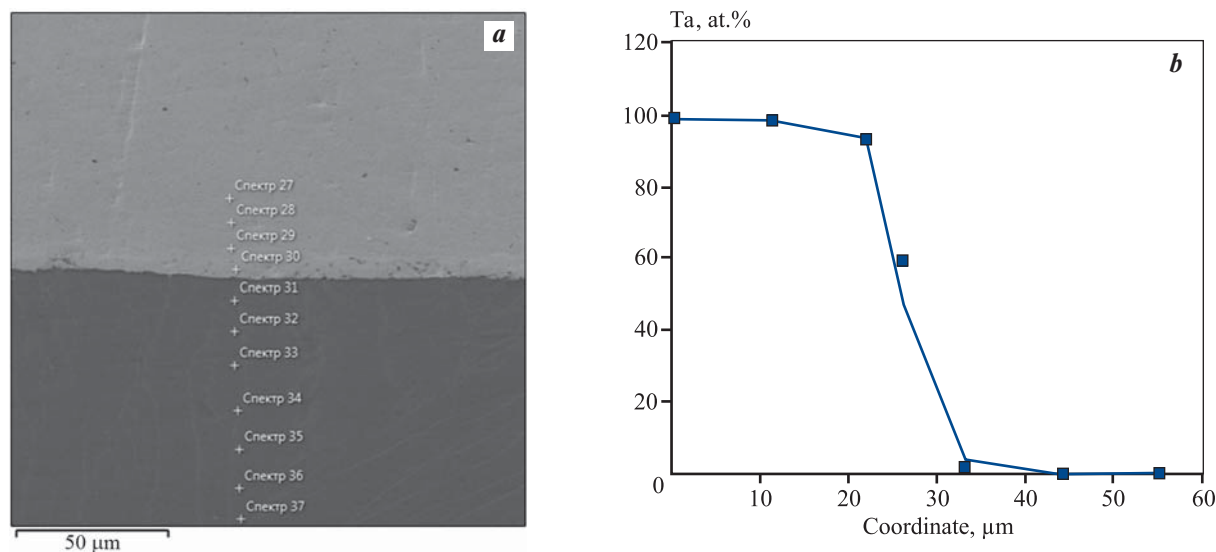


Fig. 9. Micrograph of the cut surface (a) and distribution of the Ta concentration in the Ti–Ta diffusion pair (b)

Рис. 9. Микрофотография поверхности среза (a) и распределение концентрации Ta в диффузионной паре Ti–Ta (b)

Conclusion

In this work, a technique for studying interdiffusion in pairs consisting of single-component (titanium—tantalum) and one and multiple (titanium—high-entropy alloy) refractory metals with a BCC lattice was developed and tested.

Diffusion annealing was carried out for 12 h in a vacuum with a residual argon pressure of $6.65 \cdot 10^{-3}$ Pa at a temperature of 1200 °C. The chemical composition in the interdiffusion zone was determined by energy-dispersive X-ray analysis. The obtained data on the dependence of the intensity of the corresponding spectral line for titanium and various elements of multicomponent alloys were recalculated in terms of the concentrations of the main elements in the diffusion zone.

Interdiffusion in the titanium—alloy pair is associated mainly with the penetration of the alloy components into titanium as a more fusible part of the system. A change in the signal intensity is observed at a distance of 150–250 μm for all elements. A sharp drop in the signal intensity takes place at a distance of around 50 μm.

The behaviour of the elements can be well described by the erf ϵ -shaped solution, which indicates the absence of a noticeable concentration dependence of the interdiffusion coefficients. Under the given experimental conditions, the average diffusion coefficient for all elements (except titanium) is $D = 3.0 \cdot 10^{-14}$ m²/s, which is approximately an order of magnitude less than the

self-diffusion coefficient in β -titanium, which is equal to $2.0 \cdot 10^{-13}$ m²/s [19]. Similarly, for comparison, it is possible to give the diffusion coefficient values in titanium at a temperature of 1200 °C of other refractory metals, namely: zirconium — D (Zr/Ti) = $2.6 \cdot 10^{-12}$ m²/s; molybdenum — D (Mo/Ti) = $9.3 \cdot 10^{-13}$ m²/s [20]; niobium — D (Nb/Ti) = $7.2 \cdot 10^{-13}$ m²/s [21] (isotope method); tantalum — D (Ta/Ti) = $7.2 \cdot 10^{-13}$ m²/s [22]; hafnium — D (Hf/Ti) = $1.0 \cdot 10^{-12}$ m²/s [23].

Similar studies for a titanium—tantalum pair show a significant difference in the diffusion processes in tantalum—titanium and alloy—titanium pairs. A change in the signal intensity (and, accordingly, the concentration of components in the diffusion zone) takes place at a distance of 20 μm. The data obtained correspond to the interdiffusion coefficient $D = 5.0 \cdot 10^{-16}$ m²/s, which is approximately 2 orders of magnitude lower than for the titanium—HEA pair. Note that tantalum and multicomponent alloys have significantly different melting temperatures (solidus and liquidus regions for alloys) of 3290 K for pure tantalum and 2100–2400 K for alloys [24].

References

1. Divinski S.V., Lukianova O.A., Wilde G., Dash A., Esakkiraja N., Paul A. High-entropy alloys: Diffusion. *Encyclopedia of Materials: Metals and Alloys*. 2020; 1–18. <https://doi.org/10.1016/B978-0-12-803581-8.11771-0>
2. Yong Zhang, Ting Ting Zuo, Zhi Tang, Michael C. Gao, Karin A. Dahmen, Peter K. Liaw, Zhao Ping Lu. Micro-

- structures and properties of high-entropy alloys. *Progress in Materials Science*. 2014; 61: 1–93.
<https://doi.org/10.1016/j.pmatsci.2013.10.001>
3. Yeh J.W., Chen S.K., Lin S.J., Gan J.Y., Chin T.S., Shun T.T., Tsau C.H., Chang S.Y. Nanostructured high-entropy alloys with multiple principal elements: novel alloy design concepts and outcomes. *Advanced Engineering Materials*. 2004; (6): 299–303.
 4. Yeh J.W. Recent progress in high-entropy alloys. *European Journal of Control*. 2006; 31: 633–648.
 5. Kumar P., Avasthi S. Diffusion barrier with 30-fold improved performance using AlCrTaTiZrN high-entropy alloy. *Journal of Alloys and Compounds*. 2020; 814: 151755.
 6. Dabrowa J., Zajusz M., Kucza W., Cieślak G., Berent K., Czeppe T., Kulik T., Danielewski M. Demystifying the sluggish diffusion effect in high entropy alloys. *Journal of Alloys and Compounds*. 2019; 783: 193–207.
<https://doi.org/10.1016/j.jallcom.2018.12.300>
 7. Glienke M., Vaidya M., Gururaj K., Daum L., Tas B., Rogal L., Pradeep K., Divinski S., Wilde G. Grain boundary diffusion in CoCrFeMnNi high entropy alloy: Kinetic hints towards a phase decomposition. *Acta Materialia*. 2020; 195: 304–316.
 8. Vaidya M., Sen S., Zhang X., Frommeyer L., Rogal L. Phenomenon of ultra-fast tracer diffusion of Co in HCP high entropy alloys. *Acta Materialia*. 2020; 196: 220–230.
 9. Beke D., Erdélyi G. On the self- and impurity diffusion in high entropy alloys. *Diffusion Foundations*. 2018; 17: 105–114.
 10. Lacour-Gogny-Goubert A., Huvelin Z., Perrut M., Boivin D., Horezan N., Guillot I., Vermaut Ph., Couzinié J.P. Effect of Mo, Ta, V and Zr on a duplex bcc+orthorhombic refractory complex concentrated alloy using diffusion couples. *Intermetallics*. 2020; 124: 106836.
 11. Vaidya M., Pradeep K.G., Murty B. S., Wilde G., Divinski S.V. Radioactive isotopes reveal a non sluggish kinetics of grain boundary diffusion in high entropy alloys. *Scientific Reports*. 2017; 7: 12293.
 12. Kottke J., Daniel Utt, Laurent-Brocq M., Adnan Fareed, Gaertner D., Perrière L., Rogal L., Stukowski A., Able K., Divinski S., Wilde G. Tracer diffusion in the Ni–Co–CrFeMn system: Transition from a dilute solid solution to a high entropy alloy. *Scripta Materialia*. 2018; 159: 94–98.
 13. Moghaddam A.O., Trofimov E.A. Toward expanding the realm of high entropy materials to platinum group metals: A review. *Journal of Alloys and Compounds*. 2021; 851: 156838.
 14. Zhenbang Wei, Cuiping Wang, Shiyang Qin, Yong Lu, Xiang Yu, Xingjun Liu. Assessment of atomic mobilities for bcc phase in the Ti–Nb–V system. *Journal of Phase Equilibria and Diffusion*. 2020; 41: 191–206.
 15. Razumovskii I.M., Beresnev A.G., Logacheva A.I., Razumovsky M.I., Bokstein B.S., Rodin A.O. Multi-component refractory metals base alloys — new generation of high-temperature composite materials. *Konstruktsii iz kompozitsionnykh materialov*. 2019; (1): 45–50. (In Russ.). Разумовский И.М., Береснев А.Г., Логачева А.И., Разумовский М.И., Бокштейн Б.С., Родин А.О. Сплавы на основе многих тугоплавких металлов — новое поколение жаропрочных композиционных материалов. *Конструкции из композиционных материалов*. 2019; (1): 45–50.
 16. Shelekhov E.V., Sviridova T.A. Programs for X-ray analysis of polycrystals. *Metal Science and Heat Treatment*. 2000; 42 (8): 309–313.
<https://doi.org/10.1007/BF02471306>
Шелехов Е.В., Свиридова Т.А. Программы для рентгеновского анализа поликристаллов. *Металловедение и термическая обработка металлов*. 2000; 42 (8): 309–313.
 17. Bokstein B.S. Diffusion in metals. 2-nd ed. Moscow: Lenand, 2019. (In Russ.). Бокштейн Б.С. Диффузия в металлах. 2-е изд. М.: Ленанд, 2019.
 18. Mehrer H. Diffusion in solids. Berlin, Heidelberg: Springer-Verlag, 2007.
<https://doi.org/10.1007/978-3-540-71488-0>
 19. Reza N., Libanati Y. Autodifusion de titanio beta y hafnio beta. *Acta Metallurgica*. 1968; 16: 1297–1305.
 20. Pavlinov L.V. Diffusion of metallic impurities into zirconium and titanium. *Fizika metallov i metallovedenie*. 1967; 24 (2): 272–277. (In Russ.). Павлинов Л.В. Диффузия металлических примесей в цирконии и титане. *Физика металлов и металловедение*. 1967; 24 (2): 272–277.
 21. Pontau A.E., Lazarus D. Diffusion of titanium and niobium in bcc Ti–Nb alloys. *Physical Review B*. 1979; 19: 4027.
 22. Ansel I., Thibon M., Debuigne J. Interdiffusion in the body cubic centred β -phase of Ta–Ti alloys. *Acta Materialia*. 1998; 46 (2): 423–430.
 23. Le Gall G., Ansel D., Debuigne J. Interdiffusion in the body cubic centered β -phase of titanium–hafnium alloys. *Acta Metallurgica*. 1987; 35 (9): 2297–2305.
 24. Bernstein N., Shabaev A., Lambrakos S.G. First principles study of normal and fast diffusing metallic impurities in hcp titanium. *Computational Materials Science*. 2015; 109: 380–387.

Information about the authors

Mikhail I. Razumovsky – Postgraduate Student of the Department of Physical Chemistry, National University of Science and Technology “MISIS” (NUST MISIS).

<https://orcid.org/0000-0002-0055-4834>

E-mail: razmikhail@gmail.com

Aleksei O. Rodin – Cand. Sci. (Phys.-Math.), Associate Prof. of the Department of Physical Chemistry, NUST MISIS.

<https://orcid.org/0000-0003-1209-7594>

E-mail: arodine@mail.ru

Boris S. Bokstein – Dr. Sci. (Phys.-Math.), Prof. of the Department of Physical Chemistry, NUST MISIS.

E-mail: bokstein@mail.ru

Информация об авторах

Михаил Игоревич Разумовский – аспирант кафедры физической химии Национального исследовательского технологического университета «МИСИС» (НИТУ МИСИС).

<https://orcid.org/0000-0002-0055-4834>

E-mail: razmikhail@gmail.com

Алексей Олегович Родин – к.ф.-м.н., доцент кафедры физической химии НИТУ МИСИС.

<https://orcid.org/0000-0003-1209-7594>

E-mail: arodine@mail.ru

Борис Самуилович Бокштейн – д.ф.-м.н., профессор кафедры физической химии НИТУ МИСИС.

E-mail: bokstein@mail.ru

Contribution of the authors

M.I. Razumovsky – realization of the experiments, processing of the research results.

A.O. Rodin – preparation and management of the experiments, provision of the resources.

B.S. Bokstein – scientific guidance, correction of the text and conclusions.

Вклад авторов

М.И. Разумовский – проведение экспериментов, обработка результатов исследований.

А.О. Родин – подготовка эксперимента, руководство проведением эксперимента, обеспечение ресурсами.

Б.С. Бокштейн – научное руководство, корректировка текста, корректировка выводов.

The article was submitted 19.04.2022, revised 28.06.2022, accepted for publication 30.06.2022

Статья поступила в редакцию 19.04.2022, доработана 28.06.2022, подписана в печать 30.06.2022